Search for Heavy Right-Handed W Bosons and Heavy Right-Handed Neutrinos Produced by 7 TeV pp Collisions Inside the CMS Detector

A DISSERTATION
SUBMITTED TO THE FACULTY OF THE GRADUATE SCHOOL
OF THE UNIVERSITY OF MINNESOTA
BY

Phillip Russell Dudero

IN PARTIAL FULFILLMENT OF THE REQUIREMENTS
FOR THE DEGREE OF
DOCTOR OF PHILOSOPHY

Prof. Jeremiah Michael Mans

May, 2011

Acknowledgements

Anyone who manages to succeed in returning to academia after 18 years away has no dearth of people to thank for their help along the way. I am the poster child of indebtedness.

I would like to thank Prof. Ron Poling for graciously allowing me to unofficially audit "remedial particle physics" and for grading my homework; he helped make my return to physics after so many years away much more sanguine than Homer Simpson's. When I took his class, my wife and I had only recently gotten married. One of our favorite memories is hearing Prof. Poling declare how a proton and a neutron form a "deuteron" because they like to be together.

I would like to thank Prof. James Kakalios, who was the Director of Graduate Studies when I applied for entry. Thanks goes to him for nominating me for the 3M four-year fellowship; that honor came out of the clear blue sky.

I would like to thank my fellow students who helped me to recover lost knowledge and get through written exams and homework sets. Thanks to Kevin Klapoetke for bird-dogging graduation forms for me long-distance. Thanks to Ellie Twedt for being an American friend (and babysitter extraordinaire!) in a foreign land. Thanks to Bryan Dahmes for being a sounding board, physics guide and brother.

I wish to acknowledge also my adviser, Prof. Jeremiah "Jeremy" Mans. His arrival at the University of Minnesota was perfectly timed with my search for a research adviser. My thanks go to him for being willing to take up such an unusual student, for sharing with me from his prodigious wealth of knowledge, and for his exceeding forbearance. With regard to his renowned omnicompetence I have oft quoted the Scripture: "No student is above his teacher...it is sufficient for the student to become like his teacher" - or perhaps some reasonable fraction thereof. I am also indebted to him for the opportunity to work on the greatest technical project I can ever hope to be involved in, and to do so within the context of an international adventure.

I wish to thank my parents, to my father for his dedicated prayers and to my mother for her help both practical and profound. Thanks go to all my family and friends, who I left behind for many years, as well as for the foreseeable future, to do this research. My thanks go to them for every prayer and act of support that helped us from a long ways away.

I wish to thank my wife Kathleen particularly, for saying “whither thou goest, so goeth I,” and to say to her directly: Thank you, honey, I literally couldn’t have done it without you. You are like the lady Elwing who came to “bright Eärendil” on the sea as a bird, and suddenly by virtue of who she was and the jewel she carried, passage was granted him to reach his destination where before all was futility.

Perhaps when they get old enough, my children Benjamin and Genevieve will also appreciate the knowledge that they brought me joy and balance in the midst of all the hard work.

Finally, if it hasn’t been made plain already, I owe my eternal gratitude and praise to God my Father, Who started me on this path, Who graced it with all the people I just mentioned, Who prepared a church community to receive us when we arrived in France, Whose tests of faith are breathtakingly daunting, Whose provision came through again and again against all human wisdom and counsel, and not just for myself but for all the members of my family. Truly, “He gently leads them that are with young.” A more profoundly spiritual journey I have not yet taken; I have no idea where it’s leading, but surely “it ain’t over yet.”

Dedication

"$\mathcal{S}.\mathcal{D}.\mathcal{G}.$"
– J.S. Bach, G.F. Handel

Abstract

This paper describes a search for signals from the production of right-handed W_R bosons and heavy neutrinos N_ℓ ($\ell = \mu$) that arise naturally in the $SU_C(3) \otimes SU_L(2) \otimes SU_R(2) \otimes U(1)$ left-right symmetric model. The search was performed using data collected from proton-proton collisions produced by the Large Hadron Collider at a center-of-mass energy of $\sqrt{s} = 7\,\mathrm{TeV}$, and occurring inside the Compact Muon Solenoid experiment. The data was collected during the 2010 running period and corresponds to a total integrated luminosity of $\mathcal{L} = 36\ \mathrm{pb}^{-1}$. No excess over expectations from Standard Model processes is observed. For models with exact left-right symmetry (the same coupling in the right sector), an exclusion region is established in the two-dimensional parameter space (M_{W_R}, M_{N_ℓ}) that extends to $M_{W_R} = 1360\ \mathrm{GeV}/c^2$, exceeding prior limits set by the Tevatron proton-antiproton collider.

Prospects for discovery or exclusion of these particles in the year 2011 using a projected $1\ \mathrm{fb}^{-1}$ total integrated luminosity are presented.

In addition, a method of precision timing of calorimetric deposits in the hadron calorimeter of CMS is discussed.

Contents

List of Tables

List of Figures

Chapter 1

Introduction

This thesis describes a search for signals from the production of right-handed W_R bosons and heavy neutrinos N_ℓ ($\ell = \mu$) that arise naturally in the $SU_C(3) \otimes SU_L(2) \otimes SU_R(2) \otimes U(1)$ left-right symmetric model. The search was performed using data collected from proton-proton collisions produced by the Large Hadron Collider at a center-of-mass energy of $\sqrt{s} = 7\,\text{TeV}$, and occurring inside the Compact Muon Solenoid experiment. The data was collected during the 2010 running period and corresponds to a total integrated luminosity of $\mathcal{L} = 36\ \text{pb}^{-1}$. No excess over expectations from Standard Model processes is observed. For models with exact left-right symmetry (the same coupling in the right sector), an exclusion region is established in the two-dimensional parameter space (M_{W_R}, M_{N_ℓ}) that extends to $M_{W_R} = 1360\ \text{GeV}/c^2$, exceeding prior limits set by the Tevatron proton-antiproton collider.

The analysis presented herein is part of a larger effort within the CMS collaboration that includes collaborators from the University of Minnesota and from the Institute for Nuclear Research in Moscow, Russia. The collaborators from INR performed the same search for right-handed W_R bosons and heavy neutrinos N_ℓ in the electron channel ($\ell = e$) [1]. The results from some of their studies on background estimation and systematic error estimation have been adopted as valid for this analysis of the muon channel and, where presented herein, are accompanied with appropriate accreditation.

Chapter 2 briefly presents the motivation for this search from theoretical considerations, a comparison of the Standard Model to the Left-Right-Symmetric Model, and a description of the constraints under which this search was performed. Chapter 3 presents a summary of the major subsystems of the CMS detector. Chapter 4 discusses how the precise time of calorimetric deposits is calculated, and how this timing can be used to reject non-collisional backgrounds. Chapter 5 begins the sequence of chapters that describes the analysis itself, beginning with the data samples that were used. Chapter 6 describes the reconstruction and selection criteria for individual detector objects such as muons and jets. Chapter 7 details how the main background processes were estimated. Chapter 8 covers the main sources of systematic errors in this analysis, and how they were controlled and estimated. Chapter 9 presents the final results of the analysis, as well as prospects for discovery/exclusion in the year 2011. Chapter 10 contains final concluding remarks.

Chapter 2

Left-Right-symmetric extensions to the Standard Model

> . . . but God chose what is foolish in the world to shame the wise, God chose what is weak in the world to shame the strong, God chose what is low and despised in the world, even things that are not, to bring to nothing things that are, so that no human being might boast in the presence of God.
>
> — St. Paul

This chapter describes one essential theoretical model that motivates the search for heavy right-handed W bosons and neutrinos, the Left-Right Symmetric Model. In particular, the chapter reviews the development of the Standard Model and then describes how, historically, the Left-Right Symmetric Model followed closely thereafter as one possible extension to the Standard Model. Additional experimental evidence in the form of neutrino oscillations, which points to new physics not described by the Standard Model, is briefly discussed. The chapter also describes how this model is constrained to perform the search in the most efficient way, and the limits set already by previous experiments that inform the choice of selections used.

2.1 Motivation

2.1.1 Parity Violation[1]

The primary motivation for the existence of the Left-Right Symmetric Model (LRSM) is bound up with a number of aesthetic principles that have driven the development of quantum theory since its inception. These include the primacy of symmetry in nature, as well as the (sometimes conflicting) desires to have simultaneously the most simple, "natural" and "unified" explanations for all the behavior of the universe.

As quantum theory was developed in the 20th century, evidence for the inviolability of certain symmetries and conservation laws across all the known fundamental forces was seen repeatedly; in fact, there were times in the development of the theory when a cherished conservation principle seemed threatened by new experimental evidence. Such issues were usually resolved in favor of the principle and led to the discovery of new particles.

A prime example of such an occurrence was the anomalous energy spectrum of β rays (electrons) from nuclear decays. Contrary to other known nuclear decay modes such as α and γ decays that yielded discrete energy spectra, these decays yielded β rays with continuous spectra in apparent violation of the principles of the conservation of energy, momentum and angular momentum. Lacking a clear explanation for this phenomenon, some theorists were prepared to abandon these principles, but not Wolfgang Pauli. To save the principles, in 1930 he proposed the existence of additional neutral particles in the nucleus that would carry away some of the energy of the decay. He was vindicated when the existence of *two* previously unknown neutral particle types were confirmed experimentally, first the neutron in 1932 and later in 1956 the "neutrino", so dubbed famously by Enrico Fermi in 1934.

It was also in the 1930s that Fermi developed the first cohesive theory of a new so-called "weak force" that would explain the means by which the radioactive β decay of nuclei would proceed. His theory was later expanded by Pontecorvo in 1947 to include the decay of the recently discovered "mu meson" (now called muons) into electrons and neutrinos.

---

[1] Material adapted from [2]

Therefore when the so-called parity symmetry, which was deemed by all to be inviolable by the fundamental forces of nature, was called into question by new experimental results in the decays of strange mesons, theorists were utterly convinced that a way out of the puzzle would be found, vindicating the conservation of parity as the other conservation laws had also been vindicated previously.

The parity symmetry can be described as a reflection, or "mirror" symmetry. We expect that when a physics process is held up to a mirror, the reflection in the mirror depicts a process that can also be found in nature; that is, we would not expect nature to respect the left or right "handedness" of a particle or process. Formally, particles are thought to have fundamental properties or "quantum numbers", one of which includes a parity number of +1 or -1. Combinations of particles can be said to have a collective parity which is the product of the individual parity numbers. The conservation of parity in the context of particle interactions means that the product of the individual parity numbers of the constituent particles should be the same before and after the interaction.

However, when the decays of two so-called "strange mesons", then dubbed θ^+ and τ^+, were studied in the 1950s, it was seen that these decays, which had to proceed by means of the weak interaction, led to final states with opposite parities; yet the two particles looked to be by all other experimental data the same identical particle. The simplest explanation required that they be the same particle; but the simplest explanation also then required that a cherished conservation principle would have to be abandoned in the process.

What happened next reads like a fiction novel: In 1956, two enterprising young theorists by the names of Yang and Lee, who were concerned with this problem, at first proposed a solution similar to Pauli's: postulate the existence of additional particles rather than abandon the symmetry; yet they were challenged by another theorist, the estimable Richard Feynman, to consider the possibility of parity violation. They therefore set out to determine whether the weak interaction violated the parity symmetry. By searching the literature available up to that time, they determined that while abundant evidence already existed for the conservation of parity by all the other forces of nature, no experiment had yet been performed to determine conclusively whether parity was respected by the weak interaction.

They therefore convinced a colleague to perform such an experiment, one that harkens back to the beginning of this discussion: prepare a sample of radioactive nuclei with a known spin and cause all of their spin vectors to be aligned. Then count the number of β rays (electrons) that came out of the nuclei either aligned or anti-aligned with their spin vectors. Conservation of parity would require that the β-decay of these nuclei would lead to an angular distribution of β rays that did not respect the fact that these spin vectors were aligned in one direction. The reason is that, put in a mirror, the handedness of the nuclei's spins would appear to reverse, but the direction of the decay products would not; therefore the mirror process represented a macro state of clearly opposite parity that should otherwise be indistinguishable from its mirror conjugate. But when the experiment was performed over the Christmas/New Year's break in 1956-1957, they discovered that the distribution of β rays was asymmetric; that is, the weak decays of the nuclei sample very definitely violated parity. The simple explanation won out over the symmetric explanation.

Theorists, while initially shocked at this outcome, adapted rapidly. Subsequent theories such as Yang and Lee's two-component neutrino and the so-called "V-A Theory" formulated by Marshak and Sudarshan all explicitly required the violation of parity.

This state of affairs did not change in the 1960s when the great coup of unifying the electromagnetic and weak forces into a single cohesive theory was achieved by Glashow, Salam and Weinberg: the so-called "Electroweak unification". In constructing the electroweak theory the known matter particles were given theoretical left- and right-handed components, but for the neutrinos the right-handed components were removed and the neutrinos were forced to be massless; the violation of parity was again put in *ab initio*. The Standard Model containing the electroweak theory remains the accepted theoretical model of all particle physics to this day, and is discussed further in the next section.

However, a symmetry as respected as the parity symmetry does not go gently into that good night. Here the aesthetics of particle theory plays a strong role. It is not entirely satisfactory to construct a particle theory phenomenologically, putting in experimental results "by hand", as it were. While the Standard Model has performed magnificently since its construction in both the explanation of existing phenomenon and the prediction of new ones, it also tacitly admits to ignorance of the underlying reason for the universe's behavior. The fully natural, complete, symmetric and unified explanation still eludes us.

It didn't take long after the introduction of the Standard Model, therefore, for the Left-Right Symmetric Model to be proposed. The LRSM purports to do two things: at existing experimental energy scales it mimics the Standard Model very closely, losing none of the SM's predictive power; but at higher energy scales, scales that up till now have been beyond our reach experimentally, it purports to restore the parity symmetry.

This in itself does not constitute a strong motivation for changing the Standard Model from an experimentalist point of view; the motivation from this direction has come more recently. But as one in a long line of theories waiting for adjudication by the data coming out of the Large Hadron Collider, the parity symmetry has perhaps waited in the dock the longest for a ruling on its latest appeal, and its defending attorney is the Left-Right Symmetric Model.

2.1.2 Neutrino oscillations, neutrino mass

One recent and celebrated example of perseverance in the face of criticism and disbelief in the scientific community is that of Raymond Davis, Jr. and the Homestake experiment [3], which was intended to measure the flux of neutrinos arriving at earth from the Sun. Using models of hydrogen fusion in the sun's core, theorist John Bahcall had calculated a predicted flux of electron neutrinos, of which Davis' experiment had observed only a third. Both the equations and the experiment were called into question repeatedly during its long run from 1968 to 1994, yet no mistake could be identified. Subsequent experiments confirmed the deficit, but it wasn't until the results of the Sudbury Neutrino Observatory (SNO) in 2001 [4] that the reason for the deficit was established: neutrinos appear to oscillate between lepton flavors (electron, muon, tau) in flight. This could only be true if neutrinos have mass, which was excluded by design in the construction the Standard Model. Since Davis' experiment was designed to detect only the electron flavor of neutrinos, other flavors to which these neutrinos had oscillated were unaccounted for in the total solar neutrino flux until the SNO experiment vindicated Bahcall's calculations. The results from SNO were consistent with existing solar fusion models and provided strong evidence of oscillations between neutrino flavor states.

Davis' initial results received a warm reception from at least one quarter: theorist Bruno Pontecorvo had first proposed the theory of neutrino oscillations in 1957, and upon learning of Davis' results published a paper along with Vladimir Gribov in 1969 [5], in which they stated:

> Recently there became known the results of the beautiful experiment of Davis et al., in which deep underground a search was made of sun neutrinos. . . The purpose of this note is to emphasize again that the result of sun neutrino experiments are related, . . . , in a marked way, to properties which are so far unknown of the neutrino as an elementary particle. The question at issue is: are (is) lepton charges (charge) conserved exactly?

(Here lepton flavor is referred to as lepton charge, not to be confused with electric charge.) They then proceeded to show that in order for oscillations between two flavors of neutrinos to exist, there must be nonzero neutrino mass terms in the theory. The oscillations are caused by a mixing between the flavor eigenstates and the (nonzero) mass eigenstates.

While it is not necessary to postulate a left-right symmetry in order to explain neutrino mass, it is necessary to reintroduce to the Standard Model the right-handed neutrino components that were sent into exile. The LRSM simply does this in a manifestly symmetric way. The LRSM naturally explains the smallness of neutrino mass (and therefore neutrino oscillations) in fundamental connection with the suppression of the right-handed weak interaction.

Neutrino mass and neutrino oscillations remain two of the most hotly pursued topics of research in particle physics today [6]. The currently favored mechanism of neutrino mass splitting, called the "seesaw mechanism", which is embedded in the LRSM, is bound up also with the possible existence of other symmetries in the universe that may help to explain the origin of matter. If these symmetries exist, it is (arguably) as likely as not that they are broken at mass scales that are accessible by experiments such as the Compact Muon Solenoid at the Large Hadron Collider; in fact, their discovery will likely also point the way to a better understanding of the physics of particles at yet higher energy scales, motivating this search for heavy neutrinos in the context of the LRSM all the more.

2.2 Comparison of the SM and the LRSM

2.2.1 Gauge Theory Fundamentals[2]

So pervasive is the concept of symmetry in particle theory that one generally begins the description of any theoretical model with a discussion of the "symmetry group" that governs the model. Group theory is the mathematical technique used to analyze symmetries; as the name implies, groups are comprised of, or "group together", a set of elements and operations on those elements. The operations acting on elements in the group only and always lead to other elements in the group. Theoretical particle physics in particular uses group theory to group together particles and particle fields; the operations that transform these elements into other elements in the group are considered symmetries of the group, and also correspond to some conserved quantity in nature (Noether's theorem).

In gauge theory these group operations are commonly called "gauge transformations", the symmetries are "gauge symmetries", the symmetry groups "gauge groups", and the invariance under transformation "gauge invariance." The earliest field theory to exhibit gauge symmetry was the theory of classical electrodynamics formulated by Maxwell in the 19th century; however, the term "gauge", meaning "measure" or "scale" came into common use later. It refers to redundant degrees of freedom in the Lagrangian, which is the governing equation of the field theory. One may choose a particular transformation, or "gauge", which when applied to the Lagrangian simplifies the mathematics while leaving the observable quantities completely unchanged.

A distinction is then made between global and local transformations; i.e., between transformations that do not depend on the location in space and time (global) and those that do (local). A global phase invariance leads to a global conservation law; a quantity is conserved after integrating over all of space and time in the initial and final states. A gauge transformation however is dependent on the local space-time point, and a symmetry applied to each point in space is a more stringent requirement. For our purposes we may start by way of example with the free field Lagrangian density for leptons

$$\mathcal{L} = \overline{\psi}(x)(i\partial\!\!\!/ - m)\psi(x), \tag{2.1}$$

---

[2] Material adapted from [7]

where the Feynman "slash" notation $\partial\!\!\!/$ denotes the product $\gamma^\mu \partial_\mu$ and γ^μ are the Dirac gamma matrices, $\psi(x)$ is the lepton particle field and m is the mass of the associated lepton. To this apply a local phase transformation

$$\psi(x) \rightarrow e^{iq\theta(x)}\psi(x), \tag{2.2}$$

where $\theta(x)$ is a phase angle depending on the space-time point x and q is the particle charge to be *locally* conserved in the gauge transformation. The Lagrangian in Eq. 2.1 is not invariant to this transformation by itself because of the additional derivatives of $\theta(x)$ that are generated. What is required to restore the invariance under this transformation is the introduction of a new vector field A^μ that satisfies

$$A_\mu(x) \rightarrow A_\mu(x) - \frac{1}{q}\partial_\mu \theta(x) \tag{2.3}$$

under the same transformation; the appearance of the derivative of $\theta(x)$ cancels the equivalent term arising from the transformation of $\psi(x)$. Here the transformation earns the designation "gauge", since this transformation modifies the gauge or scale of the vector field A_μ. The new vector field can subsequently be subsumed into the partial derivative ∂_μ to form a new "covariant" derivative

$$\partial_\mu \rightarrow D_\mu \equiv \partial_\mu - iqA_\mu. \tag{2.4}$$

Equation 2.1 can now be written

$$\mathcal{L} = \overline{\psi}(x)(i\not{D} - m)\psi(x), \tag{2.5}$$

which is now invariant under local gauge transformations of the type defined in Eq. 2.2 and 2.3. The Lagrangian is now said to be "manifestly gauge symmetric", and the extension of a global symmetry to a local gauge symmetry is termed "gauging the symmetry".

This procedure has more than arcane mathematical interest; rather it carries important physical content. (1) As observed previously, the imposition of this local gauge invariance requires the introduction of one or more (depending on the dimensionality of the symmetry group) new fields. Each field thus introduced represents a new physical particle to be observed in nature. Such particles are termed "gauge" or "vector" bosons because they arise from the introduction of a vector gauge field into the Lagrangian.

(2) Note also that no mass terms have been introduced for these new vector fields, nor can they be, since their addition would break the manifest gauge symmetry for which they were introduced. Therefore the associated particles must be massless in nature. (3) The addition of the vector field A^μ leads to terms in the Lagrangian that are the product of A^μ and the leptonic fields ψ; that is, the theory necessarily prescribes that the new gauge bosons and the existing matter particles interact.

For the theory of Quantum Electrodynamics (QED), which governs the electromagnetic interaction of particles with electric charge q, all of these properties are precisely what is desired. In fact the steps above correspond identically to the gauging of charge symmetry under the symmetry group $\mathrm{U}(1)_C$, resulting in the identification of the introduced massless gauge boson with the already well-known photon, and codifying the law of local conservation of electric charge to boot. As a result the photon becomes endowed with a new role: more than being simply a quantum of light, the photon also becomes the mediator of the electromagnetic interaction between particles that have electric charge; that is, in the quantum picture two electrically charged particles interact electromagnetically by the exchange of (real or virtual) photons. The masslessness of the photon indicates something of the "long arm" or range of the electromagnetic interaction; indeed, any massless vector boson so introduced necessarily gives rise to a Coulomb $1/r^2$ law already well known to freshman physics students.

However, for other symmetries, the introduction of massless gauge bosons where none are seen in nature poses a significant problem with the theory. The solution to this problem will be described in the next section.

2.2.2 The Electroweak Theory of the Standard Model[3]

The Standard Model encompasses gauge symmetry groups that are used to explain both the dynamics of the strong interaction as well as those of the weak and electromagnetic interactions. It is only the latter two that interest us here. The 1960s saw the unification of these two interactions into one, the electroweak interaction. The symmetry group of the electroweak interaction is the direct product $\mathrm{SU}(2)_T \otimes \mathrm{U}(1)_Y$ of two other symmetry groups, the special unitary group $\mathrm{SU}(2)_T$ and the unitary symmetry group $\mathrm{U}(1)_Y$. The subscript denotes the *generator* of the symmetry.

[3] Material adapted from [7], [8], [9], [10], [11]

The first group $\mathrm{SU}(2)_T$ represents a non-Abelian symmetry under transformations by the weak interaction. The subscript T denotes the "weak isospin", a concept borrowed from isospin of the strong interaction. The use of the term "spin", where in both the strong and weak cases nothing close to an angular momentum is manifest, is intended to convey the importation of a whole mathematical machinery developed to describe the spin of particles; the same symmetry group is used. By analogy to spin, one speaks of isospin as having components or projections along some arbitrary axis in an abstract space. By virtue of the 2-dimensionality of the group there are three independent generators of the SU(2) symmetry, meaning that there are three components of weak isospin. It is the third component of weak isospin, denoted T_3, that is said to be conserved in all weak interactions.

How did this construction come to be? As described previously, the theorists started with observation: it was observed that in all "charged current"[4] weak decays, lepton flavor is conserved; for instance, in muon decay ($\mu \rightarrow e + \nu_\mu + \bar{\nu}_e$) the appearance of the ν_μ preserves the "muon" flavor, and the simultaneous appearances of the e and the $\bar{\nu}_e$ cancel, leaving net zero "electron flavor" as existed before the decay, while electric charge is transferred from the muon to the electron. No such decay has been observed without the presence of the neutrinos. Therefore a weak interaction involving a lepton always transforms the lepton into its partner neutrino or vice-versa in accordance with the rules of a group. The quantum fields associated with the leptons and their partner neutrinos are therefore paired into doublets according to their flavor:

$$\begin{pmatrix} e \\ \nu_e \end{pmatrix}, \begin{pmatrix} \mu \\ \nu_\mu \end{pmatrix}, \begin{pmatrix} \tau \\ \nu_\tau \end{pmatrix}$$

(These, along with their anti-partners, represent all the leptons known to exist in nature.) In fact, since the weak interaction is observed to couple only to the left-handed components of the leptons, we subscript the group as $\mathrm{SU}(2)_\mathrm{L}$ and the leptonic doublets as

$$\begin{pmatrix} e \\ \nu_e \end{pmatrix}_\mathrm{L}, \begin{pmatrix} \mu \\ \nu_\mu \end{pmatrix}_\mathrm{L}, \begin{pmatrix} \tau \\ \nu_\tau \end{pmatrix}_\mathrm{L}$$

[4] So-called because electric charge is conveyed across lepton flavor from the initial state to the final state

The left- or right-handed components of the leptonic fields arise naturally from the free-field solution of the Dirac equation, which governs the dynamics of relativistic quantum free fields

$$(\partial\!\!\!/ - im)\psi = 0 \tag{2.6}$$

The solutions to this equation for neutrinos (setting $m = 0$) particularly are:

$$\psi_{\mathrm{L}} = \tfrac{1}{2}(1 + \gamma_5)\psi \quad \text{and} \quad \psi_{\mathrm{R}} = \tfrac{1}{2}(1 - \gamma_5)\psi \tag{2.7}$$

where γ_5 is the fifth Dirac matrix, the product of the first four matrices, and

$$P_L = \tfrac{1}{2}(1 + \gamma_5) \;\;,\;\; P_R = \tfrac{1}{2}(1 - \gamma_5) \tag{2.8}$$

are the left and right projection operators. Forcing the neutrino to be massless therefore also forces it to be a fully chiral particle. Since the right-handed components of the massive leptonic fields appeared by all experimental evidence not to participate in weak interactions, within the context of $\mathrm{SU}(2)_{\mathrm{L}}$ they were placed alone into singlets

$$((e)_R \;\;,\;\; (\mu)_R \;\;,\;\; (\tau)_R \;,$$

and since the neutrinos also appeared to be massless, the right handed neutrino components were removed from the model altogether. We see then that within the Standard Model the properties of the neutrino are bound explicitly to the weak force, which is the only fundamental force they interact with; they carry no other “charge” (electric, color, or mass) with which to couple to the other forces.

Within $\mathrm{SU}(2)_{\mathrm{L}}$ the quark fields are likewise segregated between left-handed doublets and right-handed singlets. It is by the weak interaction exclusively that quarks can change flavor. The successful integration of quarks into the theory of weak interactions (plural) represented a victorious demonstration of the universality of the weak interaction (singular) with one constant to express its strength relative to the other forces, G_F.

The story of the second symmetry group $\mathrm{U}(1)_Y$ is bound up with that of the unification of the weak and electromagnetic interactions that occurred in the 1960s and 70s. The latter was already covered by Quantum Electrodynamics (QED), which represented at that time a wildly successful quantum gauge theory founded on the symmetry group

$U(1)_C$, where C is electric charge, which is conserved under gauge transformations as described previously. Concurrently, "Yang-Mills" fields, which are non-Abelian gauge fields, were being used to successfully explain the dynamics of quarks under the strong interaction.

The founders of electroweak theory therefore took their cue from these developments. A number of important achievements in quantum field theory were necessary to accomplish electroweak unification; we focus on two. In 1961 Sheldon Glashow postulated a new "neutral current" weak interaction, without any prior experimental evidence to suggest its existence, to complement the known "charged current" interactions of the V-A Theory. He came to this conclusion when it became clear to him that the group SU(2) would not be sufficient to unify the two interactions, and it was known that combining U(1) with SU(2) would lead to an additional neutral gauge particle.

Glashow therefore postulated that the weak and electromagnetic interactions are unified under the direct product of two symmetry groups $SU(2)_T \otimes U(1)_Y$, where the generator of the U(1) group has changed from the electric charge to a new conserved quantum number, the *weak hypercharge*, which is a linear combination of the electric charge and the third component of the weak isospin, which is the generator of SU(2) group:

$$
\begin{aligned}
Y_W &= 2(Q - T_3), \quad \text{where} \\
Q &= \text{electric charge}, \\
T_3 &= 3^{rd} \text{ component of weak isospin}
\end{aligned}
\tag{2.9}
$$

Gauging the expanded symmetry then requires four gauge vector fields, three for SU(2) and one for U(1) and two distinct coupling constants typically labeled g and g'; the free field Lagrangian for the leptons then looks like

$$
\begin{aligned}
\mathcal{L}_{lep} &= \overline{\psi}_L i\not{D}^L \psi_L + \overline{\psi}_R i\not{D}^R \psi_R, \quad \text{where} \\
D^L_\mu &\equiv \partial_\mu + \tfrac{1}{2} i(gA_{i\mu}T_i - g'B_\mu), \\
D^R_\mu &\equiv \partial_\mu - ig'B_\mu, \\
A_{i\mu} &= \text{three vector fields indexed by } i = 1,2,3 \text{ for SU(2)} \\
B_\mu &= \text{one vector field for U(1)}
\end{aligned}
\tag{2.10}
$$

in analogy to Eq. 2.4 and 2.5. Thus we are led to the creation of four massless vector bosons, one positively charged, one negatively charged and two neutral, whereas the experimental evidence supported the existence of only one massless boson, the photon. Contrary to the strong and electromagnetic forces, the weak force is far weaker, as its name indicates, and seemed to act over a much shorter distance than the former two. This hints at a force carrier particle that is quite massive and short-lived. Solving the conundrum of how to shoehorn massive gauge bosons into a manifestly gauge symmetric theory was the second major breakthrough in electroweak unification.

Perhaps most importantly, the solution meant treating symmetry in a subtly different way, by recognizing that nature apparently recognizes different energy "scales", and that at some scales the symmetries of nature are manifest while at other scales the symmetries are "hidden". If the electroweak symmetry were apparent in nature at all scales, then all the gauge bosons predicted by the theory would have been discovered with zero mass. Therefore, since this was not the case, instead of saying that nature doesn't respect electroweak symmetry one would say only that the evidence indicates the symmetry, if it exists, is hidden, or "broken", at experimentally accessible energy scales. It remained then to suggest the mechanism by which the symmetry was said to be broken.

This is the essential nature of the solution that was postulated by Peter Higgs and others in 1964. The so-called Higgs mechanism of "spontaneous" electroweak symmetry breaking (EWSB) is now arguably the most well-known aspect of the Standard Model, mainly because the mechanism is still not proven, and remains the last hidden treasure of the Standard Model for which the LHC and CMS were built to discover. The important aspects of the mechanism to our purpose are as follows.

Predictably, the solution comes in the addition of yet more fields. Salam and Weinberg applied the Higgs mechanism to the fledgling electroweak theory, postulating the minimal addition of two new complex-valued scalar components in an electroweak doublet; that is, the Higgs fields carry weak isospin quantum numbers as well as electric charges +1 and 0:

$$\mathbf{\Phi} = \begin{pmatrix} \phi^+ \\ \phi^0 \end{pmatrix} \tag{2.11}$$

This leads to additional terms in the Lagrangian, the so-called "Higgs Potential"

$V(\Phi) = -\mu^2\Phi^*\Phi + \lambda(\Phi^*\Phi)^2$ as well as terms prescribing interactions between the scalar fields and the electroweak gauge fields as well as the fermions (the *Yukawa* terms); it is through these terms that the symmetry breaking is achieved:

$$\mathcal{L}_{\text{Yuk}} = h\left[\overline{\psi}_R(\phi^\dagger\psi_L) + (\overline{\psi}_L\phi)\psi_R\right] \ , \tag{2.12}$$

where h is a coupling constant describing the strength of the interaction, and is dependent on the particle in question; i.e., the coupling of each particle to the Higgs field varies by particle, which gives them their different masses. The breaking of electroweak symmetry then comes about in the "ground state" or "vacuum state" of the Higgs potential. A gauge degree of freedom exists to choose a particular gauge for the Higgs fields such that the charged field ϕ^+ vanishes, and the expectation value of the neutral field ϕ^0 in the ground state ($\langle\phi^0\rangle$) is v:

$$\langle 0|\Phi|0\rangle = \langle\Phi\rangle = \begin{pmatrix} 0 \\ v/\sqrt{2} \end{pmatrix} \quad , \quad v = \sqrt{-\mu^2/\lambda} \tag{2.13}$$

(The Higgs field self-coupling term also leads to the mass of the famed Higgs boson, the quantum of the Higgs field.) Inserting this result into the Lagrangian converts the Yukawa terms (Eq. 2.12) into Dirac mass terms of the form

$$-m\left[\overline{\psi}_R\psi_L + \overline{\psi}_L\psi_R\right]$$

for the fermions ψ, where $m = hv/\sqrt{2}$ is the Dirac mass of the particle. This spoils SU(2)⊗U(1) symmetry, "breaking it down" to the $\mathrm{U}(1)_C$ symmetry of electric charge, which is still preserved, and endows mass to all fermions ψ. Similar terms appear for the gauge fields as well, excepting the photon.

Rearranging Eq. 2.10, one obtains the fields for the quanta of the weak and neutral current interactions observed in nature, now called the $W^\pm$ and Z^0 gauge bosons, as linear combinations, or mixtures, of the electroweak fields A_μ and B_μ:

$$\begin{aligned}
W_\mu^- &= \tfrac{1}{2}\sqrt{2}(A_\mu^1 + iA_\mu^2) \\
W_\mu^+ &= \tfrac{1}{2}\sqrt{2}(A_\mu^1 - iA_\mu^2) \\
Z_\mu &= \frac{gA_\mu^3 - g'B_\mu}{\sqrt{g^2+g'^2}} \equiv A_\mu^3\cos\theta_{\mathrm{W}} - B_\mu\sin\theta_{\mathrm{W}} \\
A_\mu &= \frac{g'A_\mu^3 + gB_\mu}{\sqrt{g^2+g'^2}} \equiv A_\mu^3\sin\theta_{\mathrm{W}} + B_\mu\cos\theta_{\mathrm{W}}
\end{aligned} \tag{2.14}$$

where $\theta_{\rm W} \simeq 30^\circ$ is called the *Weinberg mixing angle.* Note that this angle represents a convenient shorthand to express the relative strengths of the coupling constants g and g':

$$\tan\theta_{\rm W} \equiv \frac{g}{g'} \quad , \quad \sin^2\theta_W = \frac{g'^2}{g^2+g'^2} \tag{2.15}$$

The Standard Model has no *a priori* prediction for these constants; rather θ_W is frequently measured in relation to the relative masses of the W and Z bosons:

$$\cos\theta_{\rm W} = \frac{m_W}{m_Z} \tag{2.16}$$

Experimentally it is found that $M_W = 80.399 \pm 0.023$ GeV/c^2 and $M_Z = 91.187 \pm 0.002$ GeV/c^2. The universal Fermi constant that describes the strength of the weak interaction can be expressed in terms of g and M_W,

$$G_F \propto \frac{g^2}{M_W^2} \ , \tag{2.17}$$

which reveals, as was anticipated, that the weak interaction is weak precisely because it is mediated by a massive vector boson.

With regard to the neutrinos, the Standard Model is agnostic about whether anti-neutrinos exist as separate particles from neutrinos, or whether the neutrino and the anti-neutrino are actually the same particle. In the former case the neutrino is said to be a Dirac particle, since Dirac's great achievement in deriving his eponymous equation was to discover that antiparticles existed; all the other fermions in the Standard Model fall in this category. In the latter case, the neutrino is said to be a Majorana particle, after Ettore Majorana, who realized the possibility. The distinction is not merely academic, but has consequences in nature, as will be seen in the next section.

2.2.3 The Left-Right Symmetric Extension

Some time was spent in the previous section detailing the manner of electroweak symmetry breaking for the plain reason that the Left-Right Symmetric Model introduces left-right symmetry and then proceeds to explain the breaking of this symmetry in a very similar manner. Namely, the left-right (parity) symmetry is respected by nature at some as-yet-unobserved energy scale, but that at currently observable scales the symmetry is spontaneously broken by the existence of heavy particles.

It must be noted at this point that left-right symmetry has been associated from the very beginning with the rise of “Grand Unification (or Unified) Theories” (GUTs). GUTs are a class of theories so-called because they attempt to go one further than the Standard Model: having successfully unified two fundamental interactions, why not also go for a third, the strong interaction? The advantage sought after from GUTs would be their overarching simplicity and prediction of relative interaction strengths.

The first proto-GUT to be published was the Pati-Salam model [12], which included left-right symmetry as part of its gauge symmetry structure. Subsequently, Mohapatra, et al. ([13],[14],[15],[16]) refined left-right symmetry as a model in its own right. In this model, the SU(2)$_R$ symmetry group is restored, along with the associated right-handed neutrinos N_l, $l = (e, \mu, \tau)$, changing the right-handed singlets into doublets:

$$(e)_R \quad \to \begin{pmatrix} e \\ N_e \end{pmatrix}_R \quad , \quad (\mu)_R \quad \to \begin{pmatrix} \mu \\ N_\mu \end{pmatrix}_R \quad , \quad (\tau)_R \quad \to \begin{pmatrix} \tau \\ N_\tau \end{pmatrix}_R \quad .$$

The full symmetry group becomes $SU(2)_L \otimes SU(2)_R \otimes U(1)_{Y_{L+R}}$; the identity of the U(1) generator Y_{L+R} will be discussed shortly. The re-introduction of SU(2)$_R$ brings with it another coupling constant g_R (although a manifest left-right symmetry requires $g_R = g_L$), three new weak isospin generators $T_{\mu R}$ and associated quantum numbers, and a new form of hypercharge

$$Y_{L+R} = 2(Q - T_{3L} - T_{3R}) \quad \text{(cf. Eq. 2.9)}. \tag{2.18}$$

In order to accomplish the “soft” L-R symmetry breaking, the Higgs sector of the model must also be expanded from a single doublet to a “bi-doublet” plus two triplets (following the notation of [15] and [16]):

$$\mathbf{\Phi} = \begin{pmatrix} \phi_1^0 & \phi_1^+ \\ \phi_2^- & \phi_2^0 \end{pmatrix} \quad , \quad \mathbf{\Delta_{L,R}} = \begin{pmatrix} \frac{1}{\sqrt{2}}\delta^+ & \delta^{++} \\ \delta^0 & -\frac{1}{\sqrt{2}}\delta_2^+ \end{pmatrix}_{L,R} \quad . \tag{2.19}$$

This selection is the minimal necessary to accomplish the symmetry breaking in the right way and yield mass matrices involving both left and right components for the quarks and leptons. The spontaneous breaking of symmetry in this model happens in stages. First the left-right symmetry breaking is realized by the coupling of the additional Higgs fields at their nonzero ground state to the right-handed gauge fields. The ground states are chosen such that

$$\langle \mathbf{\Phi} \rangle = \begin{pmatrix} \kappa & 0 \\ 0 & \kappa' \end{pmatrix} \quad , \quad \langle \mathbf{\Delta_L} \rangle = \mathbf{0} \quad , \quad \langle \mathbf{\Delta_R} \rangle = \begin{pmatrix} 0 \\ 0 \\ v \end{pmatrix} \quad , \tag{2.20}$$

where the vacuum expectation values v, κ, κ' are chosen such that $v \gg \kappa, \kappa'$. This ensures that the associated right-handed gauge boson receives the heaviest mass and breaks the symmetry down to the Standard Model $SU(2)_L \otimes SU(1)_Y$. The second stage of symmetry breaking proceeds as before. This is a critically necessary component of the theory, since in order for it to be acceptable it must produce the agreement with experiment exhibited by the Standard Model at low energy scales.

Following this prescription to the conclusion, we find the same physical gauge fields as before (A, W, Z) along with three new physical gauge fields, all as combinations of the old and new theoretical gauge fields, analogous, albeit modified, to Eq. 2.14 [15]. The mass eigenvalues in the limit of $v \gg \kappa, \kappa'$ are ([15]):

$$M_{W_L}^2 \simeq \frac{1}{4} g^2 (\kappa^2 + \kappa'^2) \qquad \text{(SM } W^\pm\text{)} \tag{2.21}$$

$$M_{W_R}^2 \simeq \frac{1}{4} g^2 (v^2 + \kappa^2 + \kappa'^2) \qquad \text{(LRSM heavy } W^\pm\text{)} \tag{2.22}$$

$$M_A = 0 \qquad \text{(SM photon)} \tag{2.23}$$

$$M_Z \simeq \frac{M_{W_L}}{\cos\theta} \qquad \text{(SM } Z^0\text{)} \tag{2.24}$$

$$M_{Z'} \simeq \frac{M_{W_R} \cos\theta}{\sqrt{\cos 2\theta}} \qquad \text{(LRSM heavy } Z^0\text{)} \tag{2.25}$$

where g_R=g_L=g and the angle θ is similar but not identical in definition to the Weinberg angle:

$$\sin^2\theta \equiv \frac{g'^2}{g^2 + 2g'^2} \quad \text{(cf. Eq. 2.15).}$$

After symmetry breaking, we find additional mixing angles that are relations between coupling constants g_L, g_R, and g' analogous to Eq. 2.15. Two such angles describe the mixing between heavy and light gauge bosons W and heavy and light neutrino eigenstates. As before, the model has no *a priori* prediction for these angles, but experimental observation places strict limits on the level of mixing that must occur between the known and hypothetical states, so that to good approximation one may identify the light mass eigenstates to the left-handed Standard Model particles and the heavy mass eigenstates to the hypothetical right-handed electroweak eigenstates.

Majorana neutrinos

Now that the right-handed neutrinos are restored, the first consequence is that the known neutrinos ν_e,ν_μ,ν_τ must have small but nonzero masses; it was therefore necessary for theorists to explain how this comes about. In [16], Mohapatra and Senjanovic first made the explicit connection between the phenomena of parity violation and the smallness of neutrino mass. Their explanation *starts* with the postulate that the neutrinos are "self-conjugate", or Majorana, in nature. In terms of quantum fields, the Majorana condition for a fermion field ψ may be written $\psi^C = \psi$, where $\psi^C = \hat{C}\psi$ and $\hat{C}$ is the particle conjugation operator; this relationship codifies the particle/antiparticle equivalency of a Majorana neutrino.

From this starting point they derived the relation

$$m_{\nu_\ell} \simeq m_\ell^2/gM_{W_R} \quad (\ell = e, \mu, \tau) \quad . \tag{2.26}$$

This shows that since the W_R must be well beyond the electroweak symmetry breaking scale, requiring parity to be violated, the corresponding neutrino masses must also be small. Taking M_{W_R} to infinity drives the neutrino masses to zero and recovers the Standard Model completely.

The Majorana nature of neutrinos is now the generally favored view [6]. Modern formulations of neutrino masses (e.g. [17, 18]) start with the Lagrangian mass terms before spontaneous symmetry breaking, written succinctly as a matrix multiplication of the chiral (L and R) fields and their conjugates:

$$\mathcal{L}^\nu_{mass} = -\tfrac{1}{2}\left[(\overline{\nu^c_L}\ \overline{\nu_R})\ \mathcal{M}\ \begin{pmatrix} \nu_L \\ \nu^c_R \end{pmatrix}\right] + \text{h.c.} \quad , \tag{2.27}$$

$$\mathcal{M} = \begin{pmatrix} m_L & m_D \\ m_D^T & m_R \end{pmatrix} \quad , \tag{2.28}$$

where each element in the central square mass matrix $\mathcal{M}$ is in itself a 3×3 matrix for all lepton generations; however, for simplicity, we take these elements as belonging to one generation. Here also a mixture of Dirac (subscript D) and Majorana mass terms is assumed in the Lagrangian. The corresponding terms after spontaneous symmetry breaking are

$$\mathcal{L}^{\nu}_{mass} = -\tfrac{1}{2}\left[(\overline{\nu}\ \overline{N})\ \mathcal{M}' \begin{pmatrix} \nu \\ N \end{pmatrix}\right] + \text{h.c.} \ , \tag{2.29}$$

$$\mathcal{M}' = \begin{pmatrix} m_\nu & 0 \\ 0 & M_N \end{pmatrix} \ , \tag{2.30}$$

where ν and N are now the neutrino mass eigenstates, and $M_N \gg M_\nu$. Matrix $\mathcal{M}$ can be thought of as a rotation through a tiny mixing angle δ of the matrix $\mathcal{M}'$; i.e.,

$$\mathcal{M} = \begin{pmatrix} \cos\delta & \sin\delta \\ -\sin\delta & \cos\delta \end{pmatrix} \begin{pmatrix} m_\nu & 0 \\ 0 & M_N \end{pmatrix} \begin{pmatrix} \cos\delta & -\sin\delta \\ \sin\delta & \cos\delta \end{pmatrix} \ ; \tag{2.31}$$

setting $m_\nu = 0$ (yielding a pure Majorana mass matrix with no coupling to the Higgs field for ν) for simplicity yields

$$\mathcal{M} = \begin{pmatrix} M\sin^2\delta & M\sin\delta\cos\delta \\ M\sin\delta\cos\delta & M\cos^2\delta \ . \end{pmatrix} \tag{2.32}$$

Comparison with Eq.2.28) suggests a mass hierarchy $m_R \gg m_D > m_L \approx 0$; applying this approximation to 2.28 and taking the eigenvalues of the matrix yields the relation

$$m_L m_R = m_D^2 \ . \tag{2.33}$$

Given this hierarchy m_D is then the geometrical mean of m_L and m_R; for a given m_D, since $m_R \approx M$ is large, then m_L must be small, hence the origin of the term "seesaw mechanism".

The existence of Majorana neutrinos has consequences in the physical world, since it leads to interactions that violate lepton number, with $\Delta L = 2$. The most well-known of these is the so-called neutrinoless double beta decay. Experimental searches for interactions of this type are ongoing.

Local B-L Symmetry

The new hypercharge generator for U(1) in the LRSM has since come to be identified with a symmetry denoted "B-L" for baryon number minus lepton number. It has been noted that B-L is already an "accidental" global symmetry of the Standard Model. The motivation for this identification derives from the continued investigations into similarities between groups of quarks (baryons are particles made of three quarks) and leptons that suggested a larger symmetry to combine the two into a GUT. This was explained by Mohapatra and Marshak [19] as follows:

> ... unlike the case of the SU(2)$_L$⊗U(1) model, the vector U(1) generator in the left-right symmetric model can be identified with B-L symmetry. One implication of this observation is that the mass scale associated with spontaneous breakdown of parity could be associated with the breakdown of local B-L electroweak symmetry...the left-right-symmetric model enables us to study the phenomenological implications of *local B-L* breaking and the possible existence of intermediate mass scales without reference to grand unification models.

In other words, one of the problems with some implementations of the LRSM arise with their embedding into GUTs; the symmetry breaking scale is far out of reach of experimental observation ($\sim 10^{15}$ eV, or 2-3 orders of magnitude higher than the operating energy of the LHC). Identification of the U(1) hypercharge with B-L accomplishes several purposes at once: 1) the "accidental" global symmetry of the Standard Model becomes a gauged local symmetry, 2) the weak hypercharge, which appeared to have no strong physical content, is now part of a larger picture, and 3) the breaking of the B-L symmetry can possibly be found at a lower, more accessible energy scale outside of a GUT framework. What follows are Marshak's later recollections of these developments in a symposium address in 1985 [20], which concludes this description of the LRSM:

> It is true that the LRS group has a form similar to another left-right symmetric $SU(2)_L \otimes SU(2)_R \otimes U(1)_{L+R}$ group studied extensively as an alternative model of the electroweak interaction... However, it was the crucial observation, based on baryon-lepton symmetry, that $U(1)_{L+R}$ should be

identified with $U(1)_{B-L}$, that led to the now generally accepted LRS group $SU(2)_L \otimes SU(2)_R \otimes U(1)_{B-L}$. Much of the physical interest of this LRS group derives from the breaking of $B-L$ local symmetry.

What does the LRS group tell us? First it predicts the existence of a trio of right-handed gauge bosons that are necessarily more massive than the left- handed ones already observed. Secondly, the LRS group implies a weak Gell-Mann-Nishijima relation of the form

$$Q = T_{3L} + T_{3R} + \frac{B-L}{2} \tag{2.34}$$

from whence it follows that $Y = B - L$ for both helicities of quarks and leptons. Implicit in Eq. 2.34 is a finite mass neutrino since the right-handed neutrino, together with the right-handed charged lepton, constitute a doublet of $SU(2)_R$. ...The structure of the LRS group also implies that parity is restored at higher energies; indeed, above 100 GeV (where $SU(2)_L$ is no longer broken), Eq. 2.34 yields

$$-\Delta T_{3R} = \frac{\Delta(B-L)}{2} \quad , \tag{2.35}$$

which relates the (spontaneous) breaking of parity to the (spontaneous) breaking of $B-L$ local symmetry. Since $\Delta T_{3R} = 1$, it follows that for purely leptonic processes (where $\Delta B = 0$), $\Delta L = 2$, and two Majorana neutrinos (one light and one heavy) are predicted per generation. The prediction of a very heavy Majorana neutrino sharply differentiates the LRS model from the standard electroweak model and some of the tests of this prediction (neutrinoless double β decay, $\mu \to e + \gamma$, muon conversion into electrons or positrons, etc.) are being carried out in laboratories around the world.

The LRS enlargement of the standard electroweak group thus relates parity breaking to the breaking of $B-L$ local symmetry, in addition to unifying the electromagnetic and weak interactions.

2.2.4 Summary

A comparison of the essential properties of the Standard and Left-Right Symmetric Models is shown in Table 2.1.

Table 2.1: A comparative summary of the properties of the Standard and Left-Right-Symmetric models.

	Standard Model	Left-Right Symmetric model
Gauge Group	$\mathrm{SU}(2)_L \otimes \mathrm{U}(1)_Y$	$\mathrm{SU}(2)_L \otimes \mathrm{SU}(2)_R \otimes \mathrm{U}(1)_{B-L}$
Fermions	Left-hand doublets $\begin{pmatrix} e \\ \nu_e \end{pmatrix}_{\mathrm{L}} \begin{pmatrix} \mu \\ \nu_\mu \end{pmatrix}_{\mathrm{L}} \begin{pmatrix} \tau \\ \nu_\tau \end{pmatrix}_{\mathrm{L}}$ Right-hand singlets $(e_{\mathrm{R}})\ (\mu_{\mathrm{R}})\ (\tau_{\mathrm{R}})$	Left-hand doublets $\begin{pmatrix} e \\ \nu_e \end{pmatrix}_{\mathrm{L}} \begin{pmatrix} \mu \\ \nu_\mu \end{pmatrix}_{\mathrm{L}} \begin{pmatrix} \tau \\ \nu_\tau \end{pmatrix}_{\mathrm{L}}$ Right-hand doublets $\begin{pmatrix} e \\ \nu_e \end{pmatrix}_{\mathrm{R}} \begin{pmatrix} \mu \\ \nu_\mu \end{pmatrix}_{\mathrm{R}} \begin{pmatrix} \tau \\ \nu_\tau \end{pmatrix}_{\mathrm{R}}$
Neutrinos	ν_{L} are massless ν_{R} do not exist	ν_{L} have small nonzero mass $\mathrm{N_R}$ are heavy partners ν and N are Majorana particles
Gauge Bosons (after symmetry breaking)	$W_L^\pm$, Z^0, γ	$W_L^\pm$, $W_R^\pm$, Z^0, Z', γ
Higgs sector (before symmetry breaking)	$\begin{pmatrix} \Phi^+ \\ \Phi^0 \end{pmatrix}$	bi-doublet $\mathbf{\Phi}$, triplet $\mathbf{\Delta_{L,R}}$

2.3 Model constraints and channel selection

The Left-Right Symmetric Model has a number of free parameters that allow for this search to proceed along several possible avenues. Among several reactions of N_R and W_R production in pp collisions the most interesting are:

- $p + p \to 2\ell^{\pm} + X$ due to the W_R fusion mechanism,
- $p + p \to W_R \to N_{R,\ell} + \ell + X$ and
- $p+p \to 2N_{R,\ell} + X$ with the subsequent decay of $N_{R,\ell}$ into charged leptons $\ell^{\pm}$ and jets.

The first reaction is quite similar to the process of lepton number violation in the double-β decay and has a clear experimental signature as an advantage. However, its cross section (that is, its probability of occurrence) is small compared to the other processes [21]. The Feynman diagram corresponding to the process $pp \to W_R \to \ell + N_{R,\ell} + X$ followed by the decay $N_{R,\ell} \to \ell + q + q'$, with the quarks reconstructed as jets in the detector, is shown in Figure 2.1.

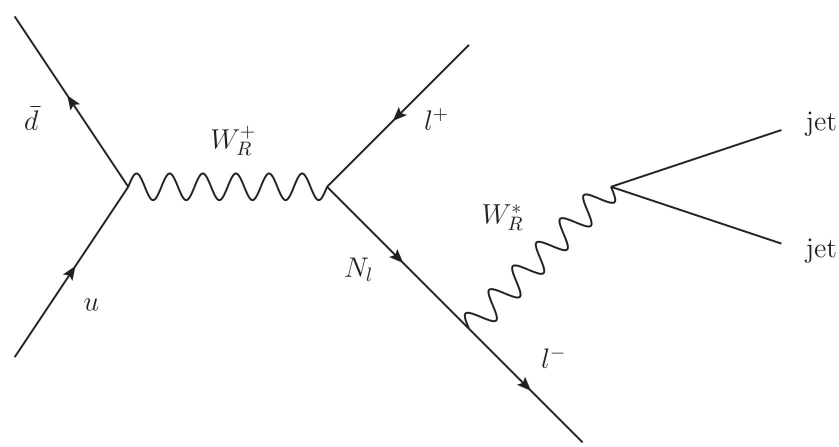

Figure 2.1: Feynman diagram for the production of the heavy neutrino through W_R bosons. The initial state quarks are constituents, called “partons”, of the colliding protons.

The cross sections of these reactions depend on the value of the coupling constant g_R, the masses M_{W_R} and $M_{N_{R,\ell}}$, the elements of the Cabibbo-Kobayashi-Maskawa (CKM) mixing matrix (which defines the mixing for all quark flavors between their mass eigenstates and their electroweak eigenstates) for the right-handed sector, and the $W_R - W_L$ and $Z' - Z$ mixing strengths. Some of these parameters are constrained by experiment, while others are not. For those that are not, the following assumptions were adopted for expediency:

- The mixing between left and right sectors is negligible.
- The right-handed CKM matrix is identical to the left-handed one.
- The left and right coupling constants are identical ($g_R = g_L$).
- The heavy neutrino N_ℓ associated with the selected search channel ($\ell = \mu$) is assumed to be the only one of three presumed neutrino flavors, the other two being $\ell = e, \tau$, that has a mass light enough to be observed at the LHC.

Under these conditions, and given the Higgs sector with Majorana masses for neutrinos, the heavy neutral right-handed Z' boson is about 1.7 times heavier than W_R [21, 22]. For this reason the process going through Z' has a smaller cross section. In addition, its signature is more complicated. Hence, this study focuses on the process depicted in Fig. 2.1 going through the direct production of W_R. As shown there the right-handed neutrino decays into a charged lepton $\ell^{\pm}$ and an off-shell W_R boson, which decays into a pair of quarks (jets (j) after hadronization). This results in a final state with four objects, two muons and two jets:

$$pp \to W_R \to \ell_1 N_{R,\ell} \to \ell_1 \ell_2 W_R^* \to \ell_1 \ell_2 + 2 \text{ jets}, \qquad \ell = \mu \ . \tag{2.36}$$

If the $N_{R,\ell}$ is a Majorana-type particle, it could decay into either leptons or antileptons with almost equal branching fractions. Therefore, the decay of the W_R shown in Fig. 2.1 into same-sign leptons is possible. Same sign lepton events would provide a very clean signature of the W_R production and would simultaneously be a direct powerful test of the Majorana nature of the $N_{R,\ell}$ [23]. However, although the requirement of the presence of two same-sign leptons reduces drastically the background level, the cost paid is in additional complexity in the form of charge misidentification studies, and in a 50% signal reduction; hence the sensitivity of the search reported for the amount of data gathered, as well as the additional effort, is not improved. Therefore, in this thesis no requirement on lepton charge is made.

For the signal event generation and calculation of the leading-order cross sections, PYTHIA 6 [24] was used with the default CTEQ6L parton distribution functions [25]. The code includes the LR symmetric model with the standard assumptions mentioned above. The dependence of the leading-order W_R total production cross section on the masses $M(W_R)$ and $M(N_R)$, as reported by PYTHIA, is shown in Figure 2.2.

The quantum field theories governing the Standard Model interactions are generally perturbative in nature; they are somewhat akin to infinite power expansions of a small-valued variable in that the first one or more terms in the expansion can be taken as a reasonable estimate of the true value. As such, the cross section values plotted in Fig. 5.2 represent the first order estimate depicted in the first-order ("tree-level" in the professional parlance) diagram Fig. 2.1. Higher order diagrams can be drawn simply by adding lines and vertices (representing particles and their interactions) that conform to the rules of the underlying Lagrangian equation. The resulting processes depicted are realized in nature; summing the additional corrections arising from these diagrams yields a more accurate estimate of the true cross section.

The accuracy of such estimates depends on the coupling constant associated with the interaction. In the case of the strong interaction, the coupling constant α_S varies as a function of energy scale; at low energies its value is too large for use with perturbative techniques, and the leading order calculation is not sufficiently accurate when compared to the accuracy from mountains of data that can be accumulated at the LHC. Calculating higher order terms for various SM processes, the so-called next-to-leading order (NLO) and next-to-next-to-leading order (NNLO) terms, is therefore necessary but difficult; it has taken years of effort that is still ongoing.

This analysis makes use of some of that effort through a software package that calculates "k-factors" for Standard Model W and Z bosons [26]. The k-factor is defined simply as the ratio of NLO/LO. SM k-factors are valid for the LRSM, since QCD does not distinguish left- and right-handed particles. In these calculations α_S has been taken at the W_R mass; for this reason the k-factor is a slowly decreasing function of the W_R

mass (Figure 2.3).

As for those model parameters that are constrained by existing data, the primary bound is provided by the DØ Experiment [27]. They performed direct searches for W' at the Tevatron, yielding a bound on the invariant mass of a right-handed W' of 739 GeV/c^2 for semi-leptonic decay modes such as the one investigated here.

However, more stringent limits have been set on M(W_R) as long ago as 1982, not by performing a direct search, but by inference from already existing data on the mass difference between the two kaon particle mass eigenstates, $\Delta m_K = K_L - K_S$ [28]. This is because the properties desired from the LRSM bosons also require them to participate in many of the same interactions as their Standard Model equivalents. The lower bound on the W' mass so derived from Δm_K plus theoretical considerations is quite stringent, $M_{W'} \gtrsim 1.6$ TeV, however with some uncertainties from the low energy QCD corrections to the kaon system.

The bound on the mixing angle between W_L and W_R is as low as $\xi_W \lesssim 0.013$ [29], which justifies our prior assumption of negligible mixing. The Z' mass is constrained to values $O(1)$ TeV and the mixing among the neutral gauge bosons to the values below $O(10^{-4})$ [30, 10].

These bounds are less stringent in more general LR models (cf. [31], in which variations on the g_R coupling constant, the right-handed CKM matrix and the right-handed neutrinos are explored). Effects of the lepton flavor violation induced by heavy Majorana neutrinos and some other limits are discussed in [32] and [33], respectively.

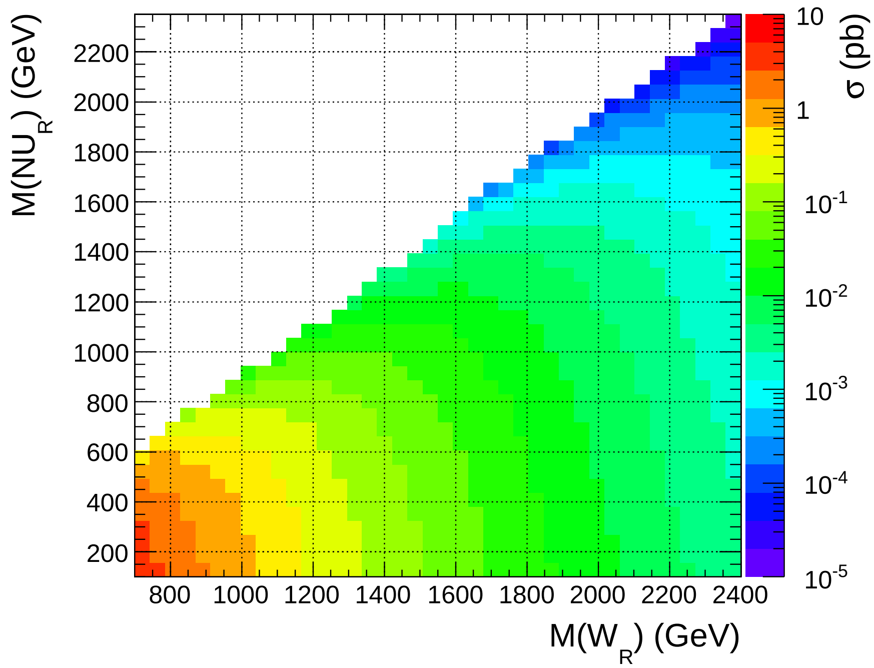

Figure 2.2: PYTHIA leading order cross section as a function of M_W and M_N.

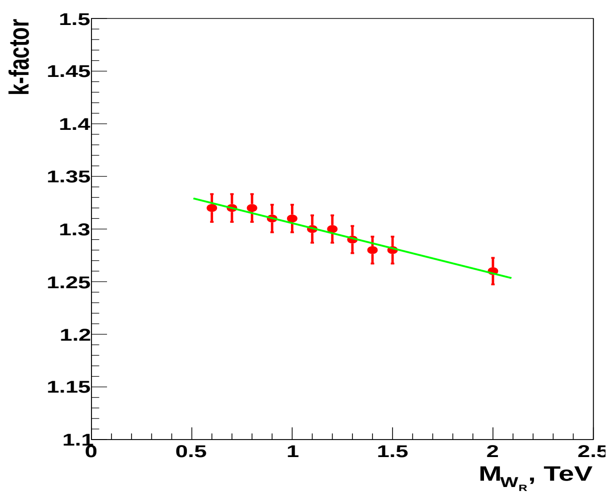

Figure 2.3: The dependence of the NNLO k-factor on the W_R mass.

Chapter 3

CMS Detector Description

Homer:	Uh, excuse me, Professor Brainiac, but I worked in a nuclear power plant for ten years, and, uh, I think I know how a proton accelerator works.
Brainiac:	Well, please, come down and show us.

Homer Goes To College

This chapter summarizes key design aspects of the CMS detector in relation to the analysis presented herein. A comprehensive reference for the CMS design exists in [34].

3.1 The LHC Machine

The design of CMS cannot be fully understood without at least a brief description of the collider parameters that drive many of the requirements that the detector must fulfill. Located at CERN, straddling the border between France and Switzerland near Geneva, the LHC [35] is by now well-known as the most powerful particle collider in the world today; it holds the current world record collider center-of-mass energy of 7 TeV, first set on March 30, 2010. It was built to discover the Higgs boson, thereby completing the Standard Model description of the subatomic world, and also to search for new "Beyond the Standard Model" physics, as represented by such theories as the Left-Right Symmetric Model.

The strategy behind the LHC design is to collide protons into protons, where the protons are grouped into thousands of "bunches". These proton bunches are injected sequentially into two evacuated pipes that together form a ring 100 meters underground with a circumference of 26.7 km, thus forming two counter-rotating beams. The beams are made to cross at certain points in their orbits, 4 points to be precise, which mark the location of particle detectors each with multi-million euro price tags and multi-national collaborations of scientists. A birds-eye view of the LHC ring and the location of the experiments is shown in Fig. 3.1.

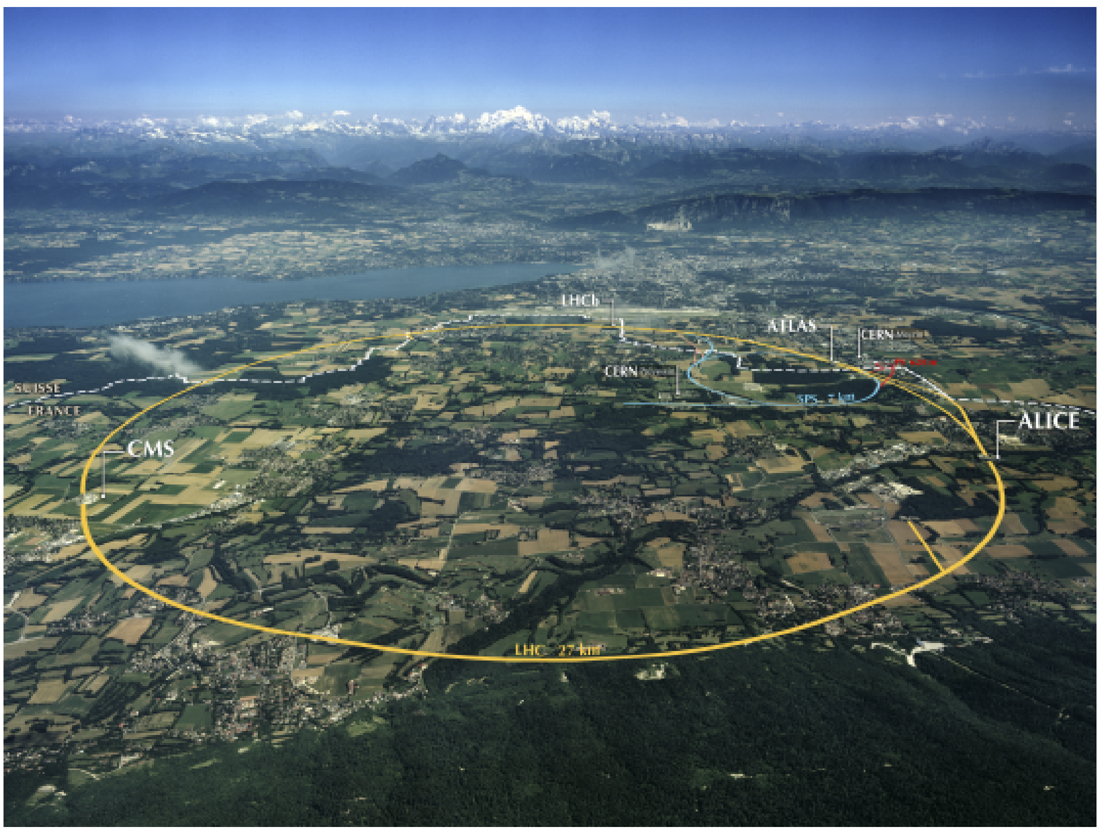

Figure 3.1: A schematic of the LHC ring and associated experiments overlaid on a photo of the surrounding countryside.

Besides the center-of-mass energy, one other fundamental parameter of the machine alludes to its potential for new science, the luminosity. The luminosity of each beam is measured in the number of protons that pass through a unit area per unit time. The higher the luminosity is, the higher the rate of collisions and the faster one achieves the potential for discovering rare new processes and particles. The LHC was designed to achieve the maximum possible luminosity for the available technology and budget. The luminosity is determined by a number of other machine parameters and can be expressed mathematically as[1]

$$\mathcal{L} = \frac{\gamma f k_B N_p^2}{4\pi \varepsilon_n \beta^*} \quad ; \tag{3.1}$$

these parameters and others are defined and evaluated in Table 3.1.

Table 3.1: LHC Machine Parameters

Parameter	Symbol	Design	2010	Units
Inst. Luminosity	$\mathcal{L}$	10^{34}	2×10^{32}	$\mathrm{cm}^{-2}\,\mathrm{s}^{-1}$
Relativistic gamma	γ	7460	3730	
Orbit frequency	f	11.2	11.2	kHz
No. of bunches	k_B	2808	~ 400	
No. protons per bunch	N_p	1.15×10^{11}	3.5×10^{13}	
Normalized transverse emittance	ε_n	3.75		μm
Betatron function at the IP	β^*	0.55		m
Beam crossing angle	θ_c	285	0	μrad
Energy per proton	E	7	3.5	TeV
Dipole field strength	B	8.33	4.17	T
Bunch separation		25	150	ns
LHC clock frequency		40	40	MHz

The LHC timing structure shown in Table 3.1 has ripple effects through all of the CMS detector front-end and counting electronics, as will be seen later, particularly in Chapter 4.

3.2 CMS Detector Essentials

The name chosen for this experiment, "Compact Muon Solenoid", yields clues to the nature of the fundamental choices made for the detector design. Figure 3.2 shows a

[1] To be precise Eq. 3.1 should also include a reduction factor F when the beam crossing angle is nonzero; however, even at design luminosity the angle is so small that F is very, very close to 1.

perspective drawing of the CMS detector with the primary subsystems labeled.

The LHC produces a large rate of hadronic events with little scientific interest to the collaboration; by comparison, the rate of muon production from proton-proton collisions is small, but the signal they produce in the detector is generally clean and well-identified; as such a detected muon signifies an event worth investigating further. CMS is therefore designed to achieve good muon identification, muon charge identification, and muon momentum resolution over a wide range of momenta, up to 1 TeV/c. For this purpose three different types of muon detection systems are contained in CMS.

CMS makes use of the $\vec{F} = q\vec{v} \times \vec{B}$ Lorentz force to measure the momentum and charge of charged particles. The magnetic field $\vec{B}$ bends the trajectory of charged particles; the higher a particle's transverse momentum ("p_{T}"), the "stiffer" or straighter its trajectory becomes. This means, however, that the p_{T} resolution for high pt muons is degraded relative to that for low p_{T} muons. The key, therefore, to quality measurement of muon momentum and charge is a particularly strong magnetic field, which maximizes the bending of the muon's trajectory relative to the fundamental uncertainty of the position measurements that are used to reconstruct the trajectory. For this reason, the CMS is built with a superconducting solenoid capable of generating a 4 Tesla uniform magnetic field within its volume, making it the largest magnet of its kind ever built, in terms of its total stored energy. Key characteristics of the solenoid magnet are given in Table 3.2.

In order to control such a powerful magnetic field, CMS was designed with an iron return yoke surrounding the exterior to capture and direct the return field lines. This makes CMS "compact" relative to its main competitor, the ATLAS detector, which uses a smaller magnetic field spread over a wider volume.

The other major subsystems of CMS can be divided by their location with respect to the solenoid. Surrounding the solenoid's exterior are eleven major components that provide structural support to the rest of the detector and largely determine its "compact" bulk : the five "barrel wheels" denoted YB0 (the central wheel), YB+1,YB-1,YB+2, and YB-2, and the six endcap disks, three on each side, YE$\pm$1, YE$\pm$2, and YE$\pm$3. The "Y" refers to the magnet return yoke, made up of construction grade steel and used to channel and contain the return field of the solenoid magnet.

Internal to the solenoid volume are the other major components of CMS, which

Table 3.2: CMS Solenoid Parameters

Magnetic length	12.5m
Cold bore diameter	6.3m
Central magnetic induction	4 T
Total Ampere-turns	41.7 MA-turns
Nominal current	19.14 kA
Inductance	14.2H
Stored energy	2.6 GJ
Weight of cold mass	220 t
Radiation thickness of cold mass	3.9 X0
Total mass of iron in return yoke	10 000 t

include electromagnetic and hadronic calorimeters, and also fully silicon-based tracker and pixel detectors. These detector subsystems will be described in more detail in the following paragraphs.

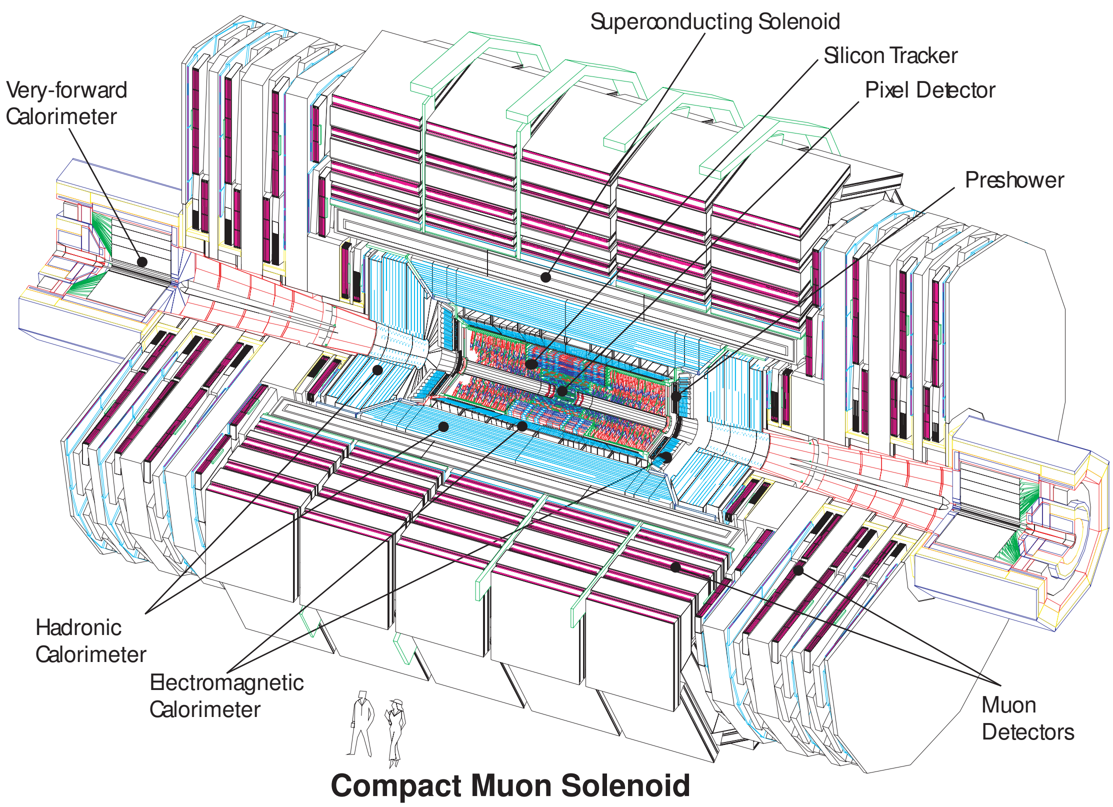

Figure 3.2: The primary components of the CMS detector

3.3 CMS Coordinate Systems

The coordinate system utilized by the CMS collaboration has the origin centered at the nominal interaction point inside the experiment. The Cartesian system defines the z-axis as coaligned with the beam. Positive z points along the beam toward the Jura Mountains from LHC Point 5 where CMS resides. This corresponds to the direction of the counter-clockwise beam (beam 1) of the LHC as seen from above. The y-axis points vertically upward, and the x-axis points radially inward toward the center of the LHC.

The azimuthal angle ϕ is measured from the x-axis in the $x-y$ plane. The polar angle θ is measured from the z-axis. Pseudorapidity is defined as $\eta = \ln \tan(\theta/2)$. Thus, the transverse components of momentum and energy (perpendicular to the beam direction), denoted by p_T and E_T, respectively, are computed from the x and y components.

The (η,ϕ) coordinate system is the native 2-D Cartesian coordinate system for locating collision remnants in the CMS detector [36], and as such is used frequently in this thesis.

3.4 CMS Tracking System Description

The tracking system of CMS was designed to address the physics needs of the experiment, to reconstruct efficiently and resolve precisely the momenta of collision products, and also of decay vertices for τ's and b-jets close to the interaction region. Such requirements tend to push the design to increased density of active material; however at the same time the tracking system had to be designed also to minimize early showers, electron/photon conversions, multiple scattering, etc. The anticipated high flux of particles - about 1000 every 25 ns at the LHC design luminosity - also imposed the need to limit the occupancy per channel both for physics and detector lifetime requirements.

The solution to these challenges was to develop a fully silicon-based tracking system with two major components. The first is a pixel detector placed closest to the interaction region with a high density of pixels of 100×150 μm size each. The pixel detector consists of 3 layers of such pixels ranging from 4.4 to 10.2 cm radius from the beampipe axis. On each end of these concentric cylindrical layers are two endcap disks with two layers apiece. In total, the pixel detector comprises 66 million channels of data. With this level of segmentation, the pixel detector achieves a spatial resolution of about 10 μm in the $r - \phi$ plane and 20 μm in z, and keeps the per-pixel occupancy to a minimal 10^{-4} per pixel per bunch crossing.

Surrounding the pixel detector is the second major component of the tracking system, the silicon strip tracker. A cross-section layout of the two components together, as well as their dimensions and η coverage, is shown in Fig. 3.3. The tracker consists of an inner barrel (TIB), outer barrel (TOB), inner disks (TID) and endcaps (TEC) on each side. Each of these components consists of silicon microstrips of varying sizes, the largest ($25\times180\,\mu$m) being in the outermost layers. Altogether the silicon strip tracker comprises 9 million additional channels of data.

Altogether the tracking system provides up to 17 hit points per trajectory, each with a spatial resolution typically measuring in the tens of μm. With such resolution the tracking system has demonstrated the ability to reconstruct tracks to better than 99% efficiency and (after alignment exercises using cosmic ray muons) resolve track momenta for muons to better than $0.1\%/\,\mathrm{GeV}/c \times p_{\mathrm{T}}$ ([37],[38]).

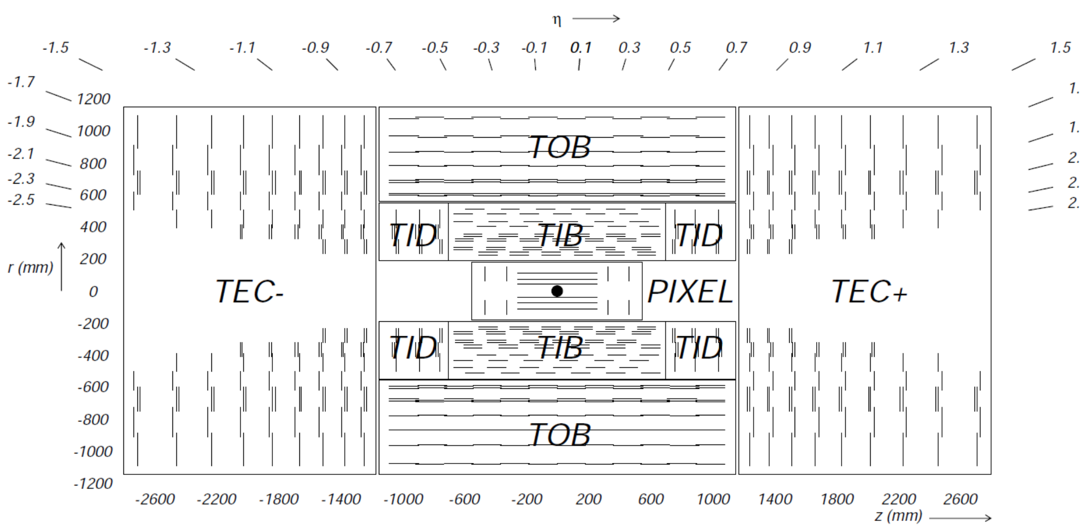

Figure 3.3: A cross-sectional diagram of the CMS Silicon Strip Tracker and Pixel Detectors.

3.5 CMS Muon Systems Description

The muon detection and measurement system is, as described previously, central to the physics mission of the CMS detector, and is also of particular relevance to this analysis, since the data used for this search was collected using a muon trigger, and the expected final state includes two reconstructed muons.

The CMS Muon detection system comprises several subsystems. Three different types of gaseous detectors are dedicated to the identification and measurement of muons: drift tubes (DTs), resistive plate chambers (RPCs) and cathode strip chambers (CSCs). The placement of muon detecting stations is shown in a cross-sectional diagram of CMS (Fig. 3.4). The silicon strip tracker rounds out the set of components within the muon system.

The type of technology used differs as a function of its location in the detector and the associated radiation environment. The tracker has already been discussed. Drift tubes are used outside the solenoid in the barrel region ($|\eta| < 1.2$) since the rates of muons and also background radiation products are low, and the fringe magnetic field is also small and spatially uniform.

The unit of installation for the DTs is called a chamber. Each DT chamber is composed of 2 or 3 "superlayers", themselves consisting of four layers of drift cells, each layer staggered by a half-cell from its neighbors for optimal coverage. The DT chambers are interleaved between the steel return yoke layers in each barrel wheel, located in 12 sectors around the ϕ coordinate, times 4 concentric rings counting outwards from the beamline along the depth coordinate, for a total of 48 chambers per wheel (Fig. 3.5(a)). Therefore, when the barrel wheels are pushed together the chambers comprise 4 concentric cylinders surrounding the beam line.

The cathode strip chambers (Fig. 3.5(b)) are used exclusively in the endcap, where the background radiation and muon rates are higher, and the magnetic field is stronger. There are a total of 468 CSCs in CMS arranged in groups of eighteen 20° or thirty-six 10° sectors per hemisphere and provide complete ϕ coverage, and η coverage between $1.2 < |\eta| < 2.4$. They are trapezoid-shaped multi-wire proportional chambers consisting of 6 anode wire planes interleaved with 7 cathode panels with strips milled perpendicular to the anode wires; this allows for simultaneous measurement of both θ and position in the $r-\phi$ plane. Their gas gaps are shorter than the DTs in order to decrease detection latency. With 6 layers, the CSCs provide superior background rejection and facilitate track matching to hits in the tracker or RPC subsystems.

However, whereas excellent spatial resolution is the hallmark of the DTs ($\mathcal{O}(100\,\mu\mathrm{m})$) and CSCs (2 mm at Level-1, 75-150 μm offline) the timing resolution is best provided by the resistive plate chambers, which are deployed in both the barrel and endcaps ($|\eta| < 1.6$ at startup) to complement the other two technologies. RPCs are comparable to scintillators in speed, and are capable of tagging a muon in much less time than a single bunch crossing period (25 ns), on the order of 1 ns. They can therefore unambiguously identify the correct crossing to which the muon is associated even at high luminosities, background rates, and pileup conditions.

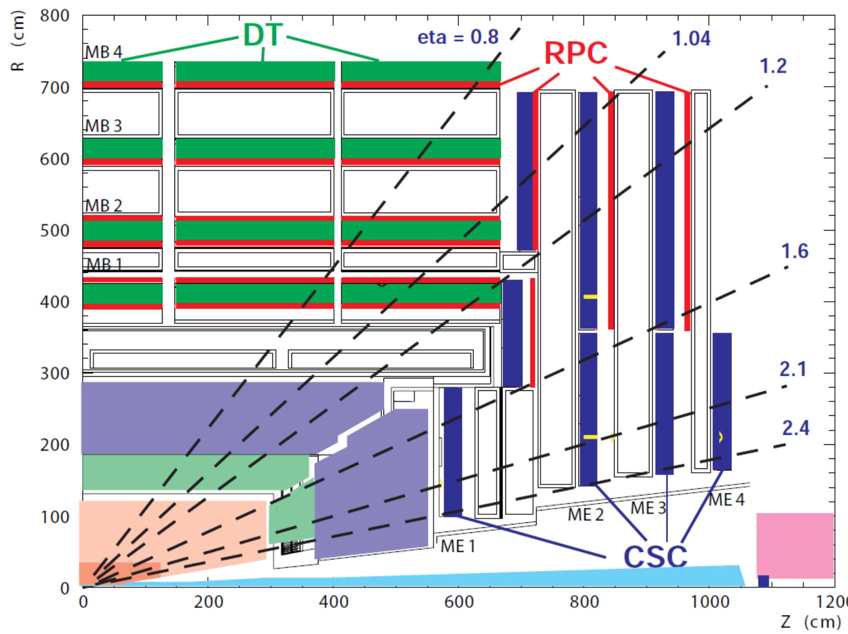

Figure 3.4: An $r-z$ cross-sectional quarter view of the subsystems comprising the CMS muon detection and triggering system.

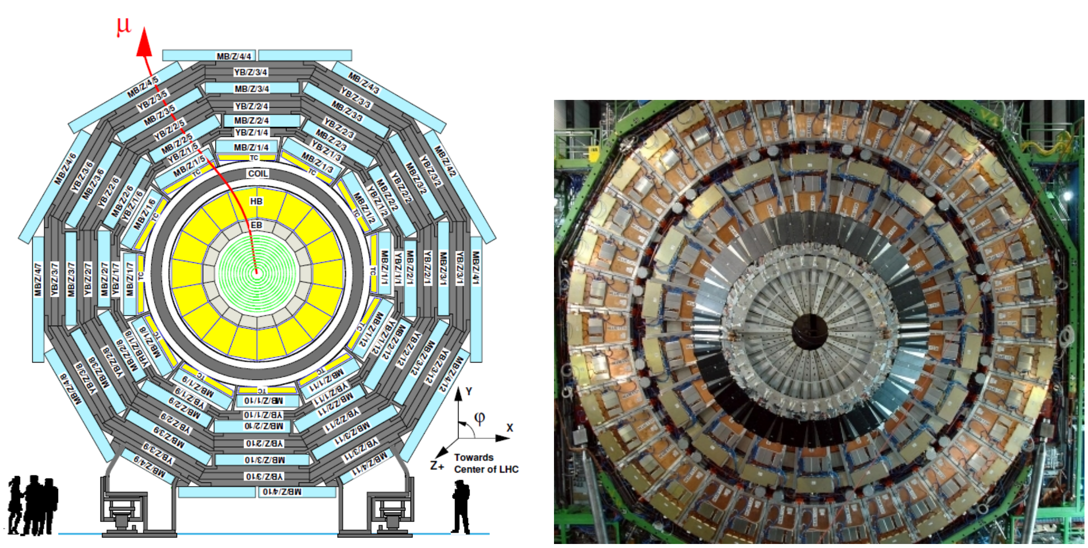

(a) Barrel wheel DT chamber schematic.

(b) Endcap disk Cathode Strip Chambers.

Figure 3.5: Views in $r-\phi$ of muon stations in a barrel wheel and endcap disk.

3.6 CMS Electromagnetic Calorimeter Description

The CMS detector includes an electromagnetic calorimeter, the ECAL, which is designed to absorb and identify EM objects, namely electrons and photons. The design of ECAL is driven by the primary goal of CMS to discover the Higgs boson via its decay to two photons. This is the preferred decay channel for discovery for a Higgs mass of $m_H < 2m_Z$, since decays to hadrons are expected to be swamped by QCD backgrounds. Therefore the ECAL is designed for good EM energy resolution and diphoton / dielectron mass resolution around 1% in the vicinity of the hypothesized light Higgs mass.

For the sake of this analysis, however, the ECAL is used primarily to add together with the HCAL inputs the total calorimetric response to jets of particles passing through both.

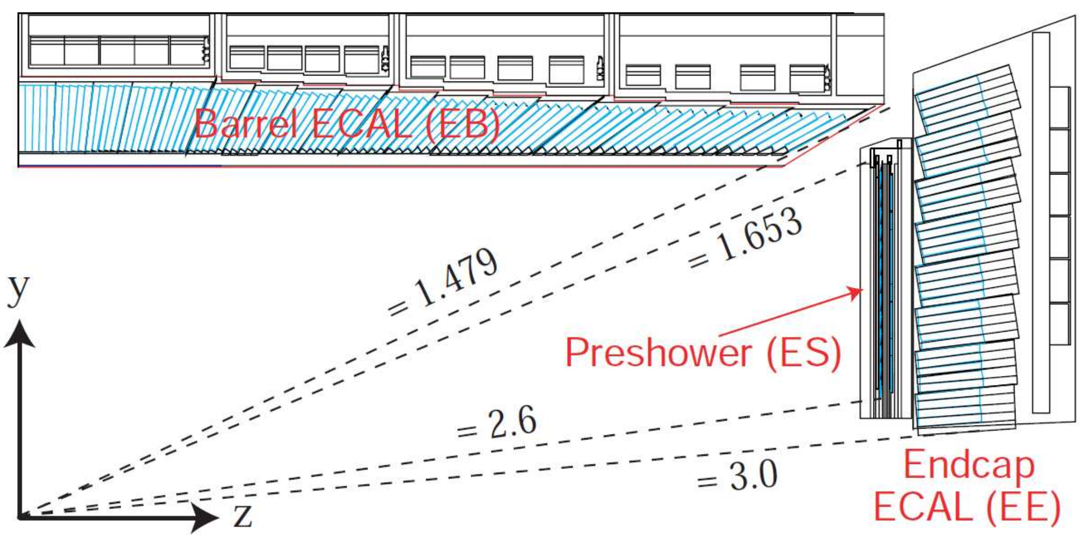

Figure 3.6: A cross-sectional quarter-view of the CMS Electromagnetic Calorimeter.

A cross-sectional diagram of the ECAL is shown in Fig. 3.6. The ECAL is divided into two barrel sections and two endcaps. The primary strength of the ECAL is its use of lead-tungstate ($PbWO_4$) crystals as a fully active absorbing material. There are 61 200 such crystals in the barrel sections and an additional 7324 crystals in each of the two endcaps. Each crystal is 230 mm in length, providing 25.8 radiation lengths of absorption, as well as a small Moliere radius. This makes the ECAL a compact, fine granularity calorimeter, necessary for minimizing space inside the solenoid.

The crystals are "quasi-projective"; the axis of each crystal is tilted about 3° with respect to the radius vector of the crystal whose origin is the IP. The crystals are intrinsically radiation hard, although changes in response in both short and long time scales are expected; therefore the crystal responses are monitored *in-situ* coincident with data-taking using a laser system and corrected for offline.

The crystals have a relatively fast but low-amplitude light response, requiring therefore a high-gain photodetector that is insensitive to the magnetic field and also to ambient particle flux levels. Avalanche photo-diodes (APDs) were chosen for the barrel sections and vacuum photo-triodes were chosen for the endcaps. The combined response of the crystals and APDs are sensitive both to temperature and to the power supply voltage; therefore both are controlled precisely to maintain the required ECAL energy resolution.

The performance of the ECAL was measured in combination with the HCAL in single particle beam tests (so-called "test beams", cf. Sec. 3.7.4) and during extensive cosmic ray muon runs ([39]).

3.7 CMS Hadron Calorimeter Description

3.7.1 Overview

The HCAL is used for this analysis in a manner similar to ECAL: to sum the calorimetric response to jets of particles arising from collisions. In addition, the author will describe other measurements taken with the HCAL in Chapter 4 to optimize its use for data-taking, therefore additional background on the HCAL design and performance is given here.

The HCAL was designed in accordance with the placement of two of its principal components inside the CMS solenoid, and with certain design goals in mind. Chief among these was to capture as much of the energy from particle showers as possible, thereby providing better energy resolution, and to supply an accurate measurement for missing transverse energy (MET). It was necessary, therefore, to maximize the number of interaction lengths inside the solenoid, as well as provide a hermetic design that eliminates all cracks and gaps through which particles may escape undetected.

The HCAL therefore consists of a set of sampling calorimeters that intermix absorbing material with active material. The barrel [40] and endcap ([34] pp. 131-137) calorimeters, referred to as "HB" and "HE" respectively, utilize alternating layers of brass as absorber and plastic scintillator as active material. Brass was chosen as the absorbing material since it is dense, non-magnetic, and affordable. The specific type of brass chosen has a density of 8.83 g/cm, a radiation length of X0 =1.49 cm and an interaction length of $\lambda = 16.42$ cm. Plastic scintillator was chosen as the active material to alternate layers with the absorber since it takes up minimal space while providing the needed sensitivity.

The light generated from passage of charged particles through the scintillator layers registers in the blue-violet part of the visible spectrum; this light is converted by wavelength-shifting fibers embedded in the scintillator. The light is then channeled to the photodetectors via clear fibers, which are spliced to the WLS fibers outside the scintillator tile, in order to minimize attenuation losses.

With 1.1m of material measured longitudinally from the beam axis, the HCAL barrel provides 5.82 interaction lengths at $\eta = 0$ (numbers don't match?). Very energetic jets at the LHC are capable of "punching through" this material; therefore an additional couple layers of scintillator are provided outside the solenoid for the central region of the barrel to improve the jet energy resolution. This part of HCAL is referred to as the outer calorimeter [41] or "HO". The HO utilizes the CMS magnet coil/cryostat and the steel of the magnet return yoke as its intervening absorber, and uses the same active material, photo-detection and readout systems as the HB and HE calorimeters.

To increase the hermeticity of the HCAL for the MET measurement, two "very forward" calorimeters ("HF") are positioned at 11m on either side of the interaction point. The HFs together increase the η coverage from $|\eta|$=2.9 to $|\eta|$=5.0. At this latter boundary, a jet or particle with transverse energy equal to 100 GeV would have to have a total energy of 7.4TeV. Since the cross section for so-called "minimum bias" interactions increases rapidly with η, the HF is expected to receive the largest flux of particles in all of CMS, from 35 ($|\eta|$=3.5) to 350 ($|\eta|$=5.0) kGy per hour at LHC design center-of-mass energy and luminosity.

Therefore the materials from which HF was constructed were chosen to help separate signals from closely spaced events (making the HF a "fast" detector), to desensitize the detector to radioactive decay products, and to survive 10 years of operation at such a dosage rate. The HF therefore consists of steel absorber with embedded radiation hardened quartz fibers as the active material. Charged particles passing through the fibers generate Cherenkov light that is transmitted through the fibers and collected by photo-multiplier tubes located "behind" the HF with respect to the IP, where the fringe magnetic field is relatively low and can be effectively shielded. This type of light production yields a signal 3-4 times faster than do the scintillator layers in the barrel and endcap.

Since the HF occupies a range of η not occupied by any other subsystem in CMS (most notably the tracker), it was decided that the HF should have the ability to distinguish hadrons from electromagnetic particles. This was accomplished by interleaving fibers with shortened lengths. The shorter fibers do not extend to the front face of HF as do the longer fibers. Since EM particle showers are shallower, the short fibers will not register them nearly as much as hadronic particle showers. The short fibers are therefore read out separately from the long fibers for each cell in HF.

3.7.2 Segmentation

The HCAL is segmented into individual calorimeter cells along the three coordinates, η, ϕ, and a third coordinate referred to as "depth". The depth is an integer coordinate used specifically to enumerate the segmentation longitudinally, along the direction radially outward from the center of the nominal interaction region. Exceptionally, in the forward calorimeter the depth coordinate has an entirely different meaning. Depth 1 refers to the readout of long fibers from the associated cell, and depth 2 refers to the readout of the short fibers from the associated cell.

The HCAL cells are "projective"; i.e., their boundaries in η and ϕ coordinates are designed to converge at the collision interaction point (IP). (One exception to this rule is the transition from barrel to endcap; the gap between them, which exists to provide room for electronics and cooling services, is pointed away from the IP to ensure hermeticity. The other exception is the HF cells, whose boundaries are parallel to the beamline.)

In the barrel and the endcap, all cells within $|\eta| < 1.74$ subtend a solid angle of $(\Delta\eta, \Delta\phi) = (0.087, 0.087)$. The barrel covers the range $|\eta| < 1.3$.

The layout of the HB, HE, and HO calorimeter cells is illustrated in Fig. 3.7. Most cells include several scintillator layers; for example, in most of the barrel all 17 scintillator layers are combined into a single depth segment.

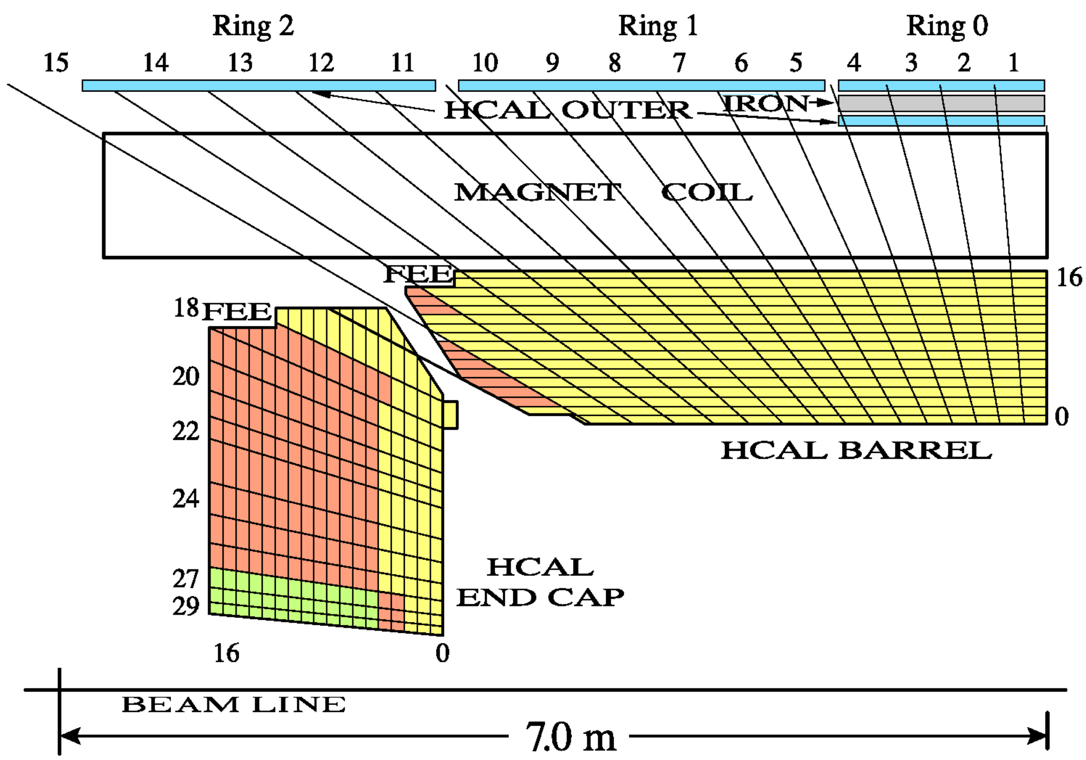

Figure 3.7: A quarter slice of the CMS HCAL detectors. The right end of the beam line is the interaction point. FEE denotes the location of the Front End Electronics for the barrel and the endcap. In the diagram, the numbers on the top and left refer to segments in η, and the numbers on the right and the bottom refer to scintillator layers. Colors/shades indicate the combinations of layers that form the different depth segments, which are numbered sequentially starting at 1, moving outward from the interaction point. The outer calorimeter is assigned depth 4. Segmentation along ϕ is not shown.

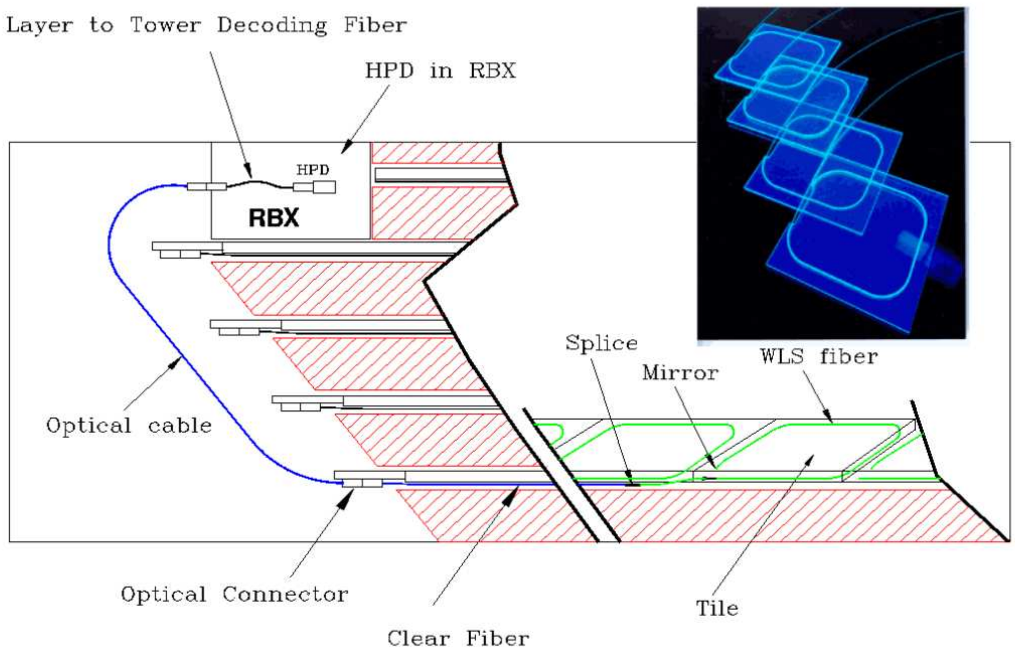

Figure 3.8: This diagram shows the alternation of absorber and scintillation layers, the collection of light using a loop of wavelength-shifting fibers within each layer tile, and the transmission of light via clear fiber (optical cable) to the HPD, which resides within a readout box (RBX).

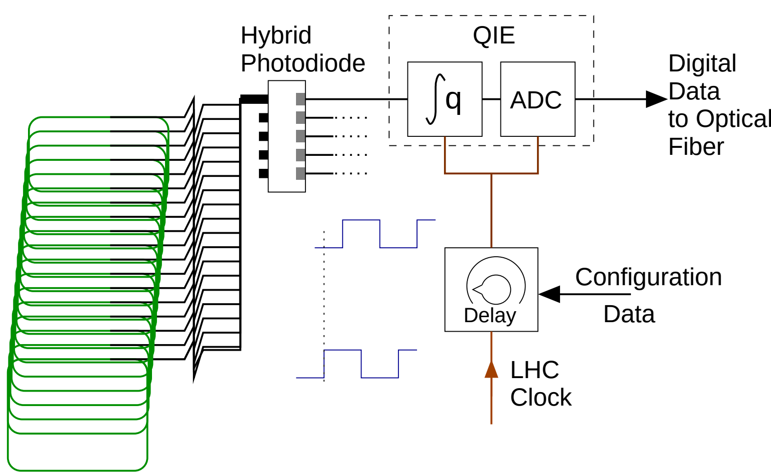

Figure 3.9: A schematic view of the HCAL front-end readout electronics. The readout for one HCAL cell/channel is shown. Key features are the optical summing of layers, charge integration followed by sampling and digitization, and per-channel programmable delay settings. The "QIE" [42] is a custom chip that contains the charge-integrating electronics with an analog-to-digital converter (ADC). The Configuration Data input defines the sampling delay settings.

3.7.3 Photo-detection, Readout, and Slow Controls

Calorimetric measurements are acquired using the HCAL readout electronics, shown schematically in Fig. 3.9. Each electronics channel collects and processes the signal of a single cell. One calorimetric measurement is acquired with each LHC clock tick (25 ns) from each cell in the HCAL. This defines a "time sample". Upon digitization the data is serialized and sent via Gigabit Optical Links (GOL) from the on-detector electronics in the underground experimental cavern ("UXC55") to the off-detector counting electronics in the adjacent service cavern ("USC55"). There the electronics deserialize the signals and convert the data to trigger primitives to be sent up the trigger system hierarchy 3.8.1.

The primary photo-detection device used for HCAL is the hybrid photo-diode, or HPD. The HPD is used in the barrel, endcap and outer calorimeters. Internally the HPD consists of a photocathode held at a potential of -6 to -8kV, at a distance of $\sim$3.3 mm from a silicon PIN diode array containing 19 hexagonal 20-mm^2 pixels (Fig. 3.10, 3.11). The array is reverse-biased at a nominal 80V. This design provides a gain of approximately 2000. The HPD was chosen over the avalanche photodiode (APD) because, as a sampling calorimeter, HCAL required a higher gain device.

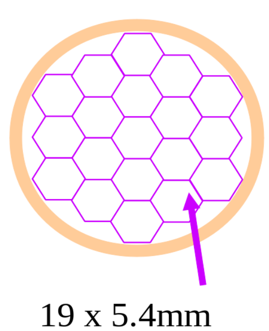

Figure 3.10: Schematic of the Hybrid Photodiode (HPD) hexagonal pixel arrangement.

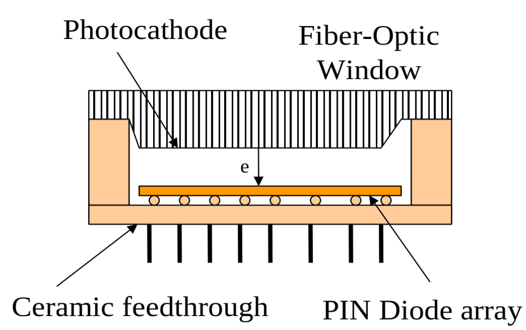

Figure 3.11: Schematic side view of the HPD construction with identified components

Since the forward calorimeters exist outside of the central magnetic field, conventional photomultiplier tubes are used instead (Hamamatsu R7525HA). Shielding from radioactive decay products is provided for the PMTs by 95cm of steel, concrete, and polyethylene. All of the fibers for one depth (long or short) of a cell run parallel to the beamline and are gathered behind the HF into a bundle that illuminates one end of an air-core light guide, which guides the light through the shielding to the window of the PMT.

The electrical signal from each pixel of an HPD (and from each PMT in HF) is fed into a custom ASIC referred to as the QIE, which highlights its primary functions of integrating charge and encoding the analog signal to digital. The QIE includes a bank of four capacitors; for each 25ns sample period one of the capacitors in the bank is connected to the input and integrates the current from the associated HPD channel. At the end of the sample period the collected charge is digitized by a 7-bit ADC, and then the next capacitor in sequence is connected. Therefore the sample clock is also properly referred to as the integration clock.

In order to maintain good bit resolution over a wide dynamic range with so few bits, the scale of the ADC is made to be non-linear; the quantization increases with the charge amplitude at fixed setpoints. In this way the contribution of quantization error to the energy resolution is negligible (Fig. 3.12).

One HPD, 18 QIEs and another custom ASIC called the Channel Control ASIC (CCA) constitute one readout module; four such readout modules are contained in one readout box (RBX). In the barrel this maps to four 5° ϕ slices in a half-barrel (or "hemisphere"); this constitutes one 20° HB ϕ sector, or "wedge", yielding 18 RBXes per barrel hemisphere (the front-end to detector mapping for the endcap and outer calorimeters is more complicated). In total there are 72 channels/RBX $\times$ 72 RBXes for a total of 5192 channels in the barrel and endcaps, not counting the 6 additional channels per RBX used exclusively for calibration purposes.

Each RBX also contains a "Clock and Control Module" that communicates to the outside world (the so-called "slow controls") and has the capability of programming various registers that exist inside the four CCAs on the readout modules, for optimal functioning of the wedge. For instance, each channel is assigned one "pedestal" DAC register, which controls the zero-input response of the channel. All the pedestal DAC register settings are subsequently calibrated in order to achieve the smallest possible RMS for the zero-input response distribution. The calibrated values are stored in an Oracle-based configuration database for tracking and consistency, and downloaded to each RBX during the initialization stage of each data-taking run.

There are analogous registers in each CCA to control the integration clock phase on a per-channel basis. The integration clock for each channel can be independently delayed in 1 ns steps with respect to the LHC clock by means of these programmable settings, referred to as QIE sampling delay settings. The purpose of these settings is to compensate for channel-dependent timing variations at the hardware level, and to permit the energy estimate from each LHC crossing to be reconstructed consistently for use in the Level-1 trigger 3.8.1 for all pulse amplitudes and for all channels. They also provide an initial coarse timing calibration.

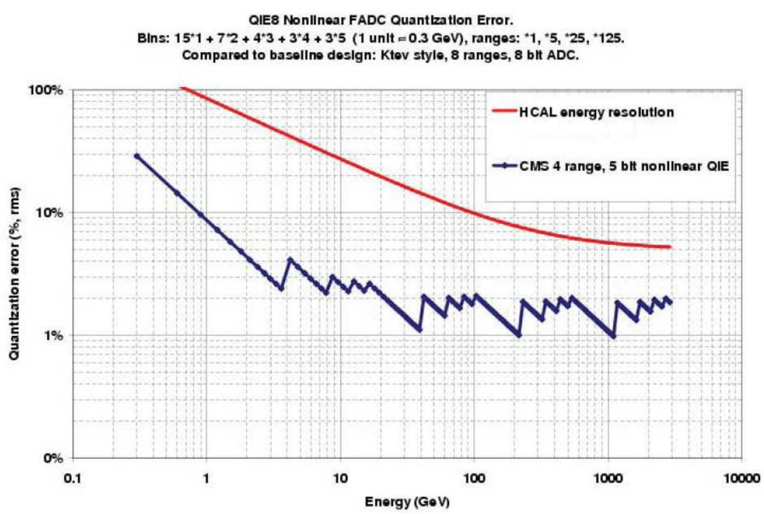

Figure 3.12: Quantization error induced by the QIE nonlinear ADC as a function of energy, compared to the expected energy resolution of HCAL.

3.7.4 Calorimeter Performance In Test Beam

This section summarizes the performance of sections of the barrel CMS Electromagnetic and Hadron Calorimeters as measured in single particle beam tests performed during

2006. The complete report may be found in [43].

The single particle beam tests were performed at the CERN H2 test beam facility. Figure 3.13 is a photograph taken of the movable platform on which two production HB wedges and one production ECAL barrel supermodule were mounted. The platform is capable of moving in the η and ϕ directions such that the in-situ geometry was mimicked, and the beam could be directed at any calorimetric cell.

Figure 3.14 shows the test beamline elements. The so-called "dog-leg" on the right half of the figure was used for very low energy operation and shall not be discussed further. For high energy operation (15-350 GeV), the particles were produced when 400 GeV protons from CERN's Super Proton Synchrotron were slammed into a target roughly 590 m upstream from the unit under test. Both electron and hadron beam types could be selected.

The beamline elements ahead of the calorimeters were used for particle identification and for triggering. Key among these elements were the muon veto and beam halo veto scintillation counters. These were used to discriminate muons from hadrons, since they have fundamentally different response functions in the HCAL. The beam halo counters were used to veto all products arising from beam halo and interactions in the beamline producing large angle deviations.

Events were triggered by coincidence hits in three of the four trigger counters shown in Fig. 3.14. Since in contrast to the in-situ CMS these triggers were asynchronous to the sample clock, a separate truth reference provided by a Time-to-Digital Converter (TDC) was used to tag both the coincidence signal and the issuance of the Level-1 trigger signal, which is synchronous to the integration clock and used to latch the data. In this way all relative sample clock phases could be measured to the accuracy of the TDC bit resolution, which was 0.78 ns (32 TDC units per time sample).

Figure 3.15 displays the measured energy resolution and the response linearity of the combined ECAL/HCAL system for pions. The circles represent the uncorrected data and the squares represent the corrected data. The corrections were applied to rectify the different "e/h" responses of the ECAL and HCAL. The data in Figure 3.15 are compiled after having fit each energy response with a Gaussian down to 5 GeV. The energy resolution is parametrized as $\sigma/E = a/\sqrt{E} \oplus b$ where a is the stochastic coefficient, b is the constant term, and the terms are added in quadrature. The linear

Figure 3.13: Photograph showing the platform used in combined HCAL/ECAL test beams.

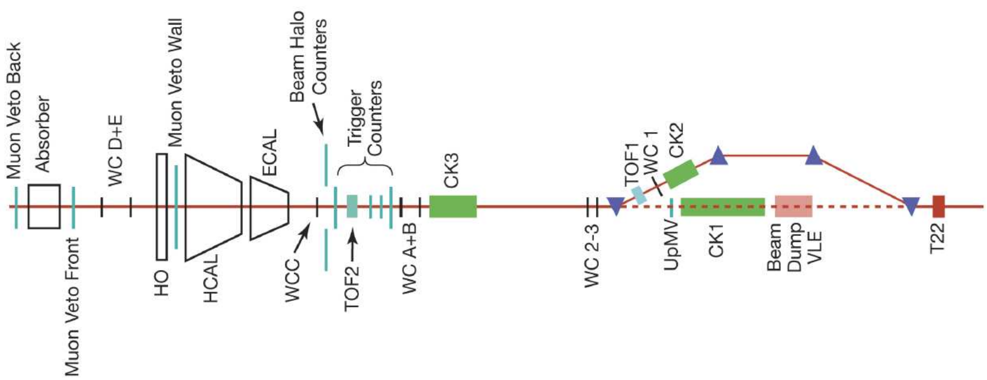

Figure 3.14: Schematic of the arrangement of test beam elements.

fits to the data yield values of a = 110.7% and b = 7.3% prior to corrections and a = 84.7% and b = 7.4% after corrections. The corrected mean response in Figure 3.15 (right) remains constant within 1.3% RMS over the tested range.

Timing results from test beams are handled in subsequent sections.

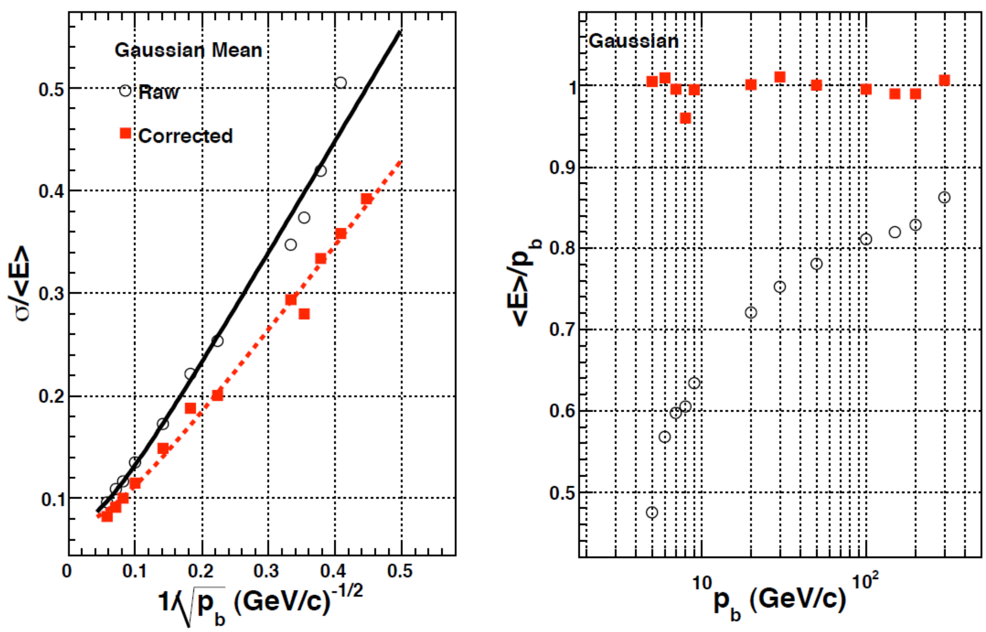

Figure 3.15: Left: The energy resolution of the combined ECAL/HCAL system from 2006 single particle beam tests, both before and after corrections (described in the text). Note that the particle energy increases as the x-axis variable tends toward zero. Right: the response before and after corrections of the combined ECAL/HCAL system is plotted.

3.8 CMS Trigger System

Of the remaining detector subsystems, the physics analyst is required to pay particular attention to the trigger system, since it directly shapes the data to be analyzed, sometimes in subtle ways. The first goal of the trigger system is so fundamental that often it is not even mentioned: to perform a radical time compression on the generation of physics data. That is, even if we could record every scintilla of collision information collected by the detector, we would still want to squeeze out the vast inefficiency represented by the majority of time that it waits for those brief moments when a collision has taken place. Once the LHC has achieved design luminosity every bunch crossing will be filled and the time compression will only involve those brief gaps in the orbit filling scheme left as a safety margin; but during the 2010 running period only about one tenth of the available occupancy was achieved, and that only at the very end of proton running.

But in fact it is known that the CMS detector can and does generate data in amounts far in excess of our ability to stream or store; even a single proton bunch circulating in the LHC will collide with its counterpart at a rate of 11 kHz and thereby exceed our bandwidth limitations for modern storage media. Fortunately the vast majority of this data is dominated by physics processes of limited physical interest. This is where the trigger system comes in. The trigger system is designed to reduce the fire hose of data generated at bursts of up to 20 interactions per crossing times the 40 MHz crossing rate, down to a relative trickle of 200-500 Hz suitable for long-term storage. The rest is irretrievably lost; therefore the trigger system is programmed to discern collision events of the most interest to us.

The CMS Trigger system does this in two stages, or “levels”. The “Level-1” trigger system, or “L1”, takes a rough measure of the quantities of interest for every 25 ns bunch crossing; fortunately it is given 128 times as long to make a decision about whether the information contained in that bunch crossing is of interest; all the precision data is held for about 3.2 μs in data pipelines before it is overwritten. If the Level-1 trigger system determines in that period of time that a given collision event warrants a second look, the data collected by the entire CMS detector for that event is “read out”.

That second look is accomplished by the CMS High-Level Trigger or “HLT”. The HLT makes a storage decision: whether the event information sent by the L1 system is of sufficient interest to be stored permanently or thrown away. The complete set of event data is shipped to one of hundreds of “event builder” computing nodes to reconstruct the event; dozens of algorithms are then run over a period of milliseconds on these data and a storage decision is made.

These two levels of the trigger system are described further below.

3.8.1 The Level-1 Trigger

The L1 trigger processing starts at its most fundamental level with pieces of information that are quite specific to the subsystem in question; these pieces of information are referred to as “trigger primitives”. The major subsystems that contribute primitives to the L1 trigger are the calorimeters and the muon subsystems. The pixel and tracker detectors do not feed the L1 trigger system independently, particularly because of the amount of time it takes to formulate meaningful event information out of the millions of channels involved.

Therefore the L1 trigger system architecture exhibits a well-defined, modularized hierarchy, as shown in Fig. 3.16. Local trigger information is fed to regional trigger processors, which synthesize the information and present the top candidates ultimately to the Global Trigger, or GT.

Since the presence of an isolated muon in an event axiomatically signifies an event of interest, particularly for this analysis, the muon trigger subsystems play a prominent role. The Global Muon Trigger (GMT) receives track information from the local triggers dedicated to each of the muon subsystems. The DT trigger and DT Track Finder (DTTF) together synthesize muon track segments and hit patterns in the individual chambers into tracks with momenta and track quality criteria assigned; the top four muon candidates ranked by these criteria from the DTTF are forwarded to the GMT. In like fashion the CSC local trigger/CSC Track Finder (CSCTF) and RPC local triggers forward their top four candidates to the GMT. The GMT also receives minimum ionizing particle (MIP) and isolation (ISO) information from the regional calorimeter trigger pertinent to these muon candidates.

In addition to the trigger candidates from the regional trigger systems, the GT receives information about the readiness of the system to receive a new trigger from the Trigger Control System. It subsequently adjudicates whether, given the worthiness of the trigger candidates and the availability of the system, to issue an Accept (L1A). The L1A signal is distributed back to the detector electronics to initiate readout of all the precision data. The maximum allowable L1-Accept rate is 100 kHz; an additional safety factor of 3 is ensured by both the pipeline depth and the trigger rules that prohibit successive events from triggering.

The L1 Trigger system is implemented in custom-built electronics cards either mounted

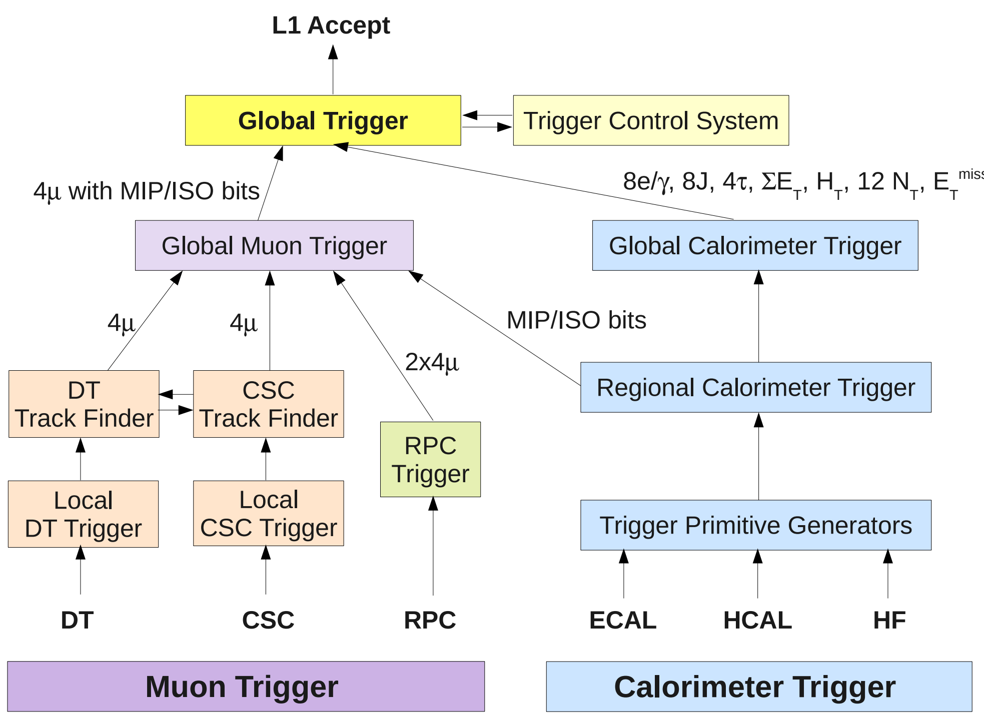

Figure 3.16: Architecture of the CMS Level-1 Trigger System.

on the detector itself ("on-detector or "front-end" electronics; this is the case for the muon local trigger electronics) or are housed in racks (the so-called "off-detector" or "counting" electronics) located in the underground service cavern, which is adjacent to the experimental cavern wherein the detector itself resides. While several feet of rock and earth thereby shield the counting electronics from the high radiation environment of the experimental cavern, the additional cabling required to connect the two imposes additional constraints on timing and storage, because the signal propagation delay for both read-out and trigger control signals eats into the trigger decision time budget.

3.8.2 The High-Level Trigger

The High-Level Trigger system, or HLT, takes the place of the Level 2 and Level-3 systems historically used by previous particle detector experiments such as CDF and DØ. By stark contrast to the L1, the HLT is implemented as a collection of software algorithms that run on a "filter farm" comprising thousands of CPUs and networking switches. The specialization is contained entirely in the algorithms that these nodes execute. Since the HLT farm has access to the entire collection of precision read-out data from the detector, the only limitation on the complexity of the algorithms run on the farm is time. An optimized form of the full offline reconstruction software is run online, represented by multiple execution "paths" in a trigger "menu". All paths in the trigger menu are required to complete in 10 ms or less in order to maximize what might be called the "meaningful physics to disk" rate; however, the execution latency varies widely from event to event depending on their content.

For this analysis, the key additional component added by the HLT is the track reconstruction software used to improve the quality of muons detected at Level-1. The HLT makes use of the full complement of muon reconstruction algorithms (cf. Sec. 6.2) to determine whether the muons seen at Level 1 pass the quality and threshold requirements.

The trigger menu for the 2010 running period was evolved over time according to the plans announced by the LHC operations team, and according to rates of occurrence for each path both projected and measured by the CMS Trigger Studies Group. The impact of the trigger menu evolution on this analysis is discussed in Sec.5.1.

Chapter 4

HCAL Hit Time Reconstruction

Time flies like an arrow, but fruit flies like a banana.

— Groucho Marx

Once properly synchronized and calibrated, the CMS HCAL electronics allow the precise reconstruction of both the energy and time of each single calorimetric energy deposit (or "hit"). The goal of precise time reconstruction is to obtain the time of each hit to much better resolution than the 25 ns time sample width. The purpose of measuring the precise time of a hit is to take advantage of the phase control of the LHC collision and CMS sampling clocks; by means of this control the collision products are expected to arrive in the detector within a narrow window of time, on the order of 1 ns or less. If the spread of the reconstructed hit time distribution can be reduced to a comparable width, then background processes that are uncorrelated with the sample clock (cosmic rays, detector noise) can be largely rejected on the basis of timing.

4.1 Description

Precise time reconstruction of calorimetric hits can be achieved mainly because each hit appears as a pulse that stretches over several time sample intervals. Precise time reconstruction requires detailed knowledge of the pulse shape generated by a single hit. The pulse shape is determined by several characteristics of the subdetector in question. In the case of the HB and HE, these characteristics include time constants associated with the scintillator material, with the photodetector, and with the read-out electronics.

However, the electronics introduce an additional complication in that the pulse is not sampled, but rather integrated over each time sample interval (25 ns), as described previously. The concept of a relative phase between any particular characteristic of the pulse and the integration clock ticks (the edges of the time sample bins) must be introduced; also the question of what constitutes a precise hit time of t=0 must be addressed.

A robust definition of precise hit time t=0 requires careful consideration of the pulse features. One might intuitively select as time t=0 the phase whereby energy from the leading edge of the pulse just begins to enter a time sample; however, this subjects the definition to variation due to noise on the order of the signal itself. An alternative definition is chosen instead to define time t=0 to coincide with the phase whereby the second of the first two nonzero bins begins to exceed the first in amplitude; i.e., the pulse peak straddles a sample boundary. This is a technical definition used for the purposes of reconstruction; a subsequent section of this chapter discusses how one may define a different t=0 suitable for physics analysis.

Figure 4.1 shows both the simulation pulse shape and its digitized, integrated form positioned at time t=0ns and at a later time t=15ns. The gridlines represent time sample boundaries.

By virtue of the signal distribution over several bins, a first order time reconstruction that calculates an amplitude-weighted peak bin is commonly employed, as follows:

$$\text{Weighted peak bin} = \left[\frac{(p-1)A_{p-1} + pA_p + (p+1)A_{p+1}}{A_{p-1} + A_p + A_{p+1}}\right] \times C \quad , \tag{4.1}$$

where A_i represents the amplitude of an arbitrary time sample i, and p is the value of i such that A_p is maximum over the set of samples (represented by bin 2 in Figure 4.1). The constant C is an amplitude-independent normalization constant that rescales the first order estimate to a range from zero to one. Normalizing the range of possible peak bin values (and offset, according to the t=0 definition above) and subsequently multiplying by the time sample width (25 ns) immediately yields a linear approximation (t_ℓ) to the precise time of the hit within the peak time sample.

$$t_\ell = (25 \text{ ns}) * \text{Norm}(\text{Weighted peak bin}) \tag{4.2}$$

From this first order estimate of the time numerous corrections are applied, as follows.

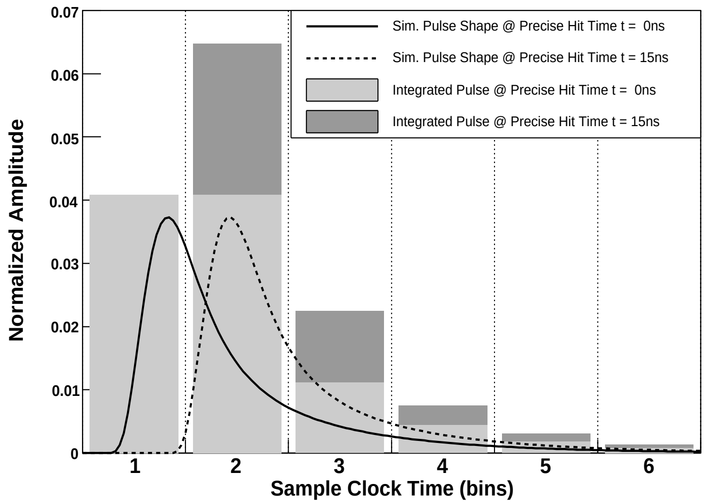

Figure 4.1: Simulation pulse shape and its integrated form positioned at Precise Hit Times t=0 and 15 ns

The first correction is necessitated by the asymmetry of the pulse shape and therefore requires detailed knowledge of the precise pulse shape. To this end the pulse shape was reconstructed from test beam data and then fit to a functional form (4.3.1). This functional form was then used to derive the correction as a function of the normalized weighted peak bin:

$$t_p = t_\ell + F_{correction}(\text{Norm(Weighted peak bin)}) \quad . \tag{4.3}$$

A second correction is required to compensate for an effect induced by the QIE ASIC described in 4.2.3.

This algorithm yields accurate time measurements except when consecutive bunch crossings yield energy measurements of similar amplitude within the same HCAL cell. Such events can be identified by their anomalous pulse shape, and the time measurement can be marked as having poor resolution.

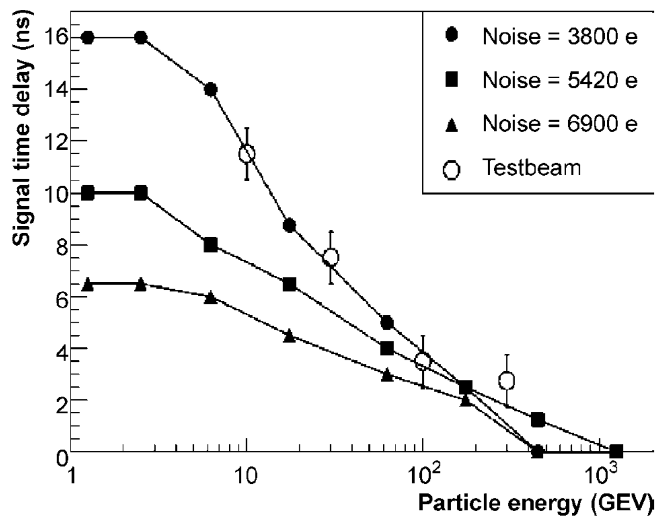

Figure 4.2: Time slew caused by the front-end electronics as a function of energy for three choices of pedestal noise.

4.2 Sources of timing variation, uncertainty, and bias

4.2.1 Channel-to-channel variations

There are two dominant sources of channel-dependent timing variation: the different time-of-flight of particles from the interaction region to each HCAL cell and the different signal propagation times through optical fibers of different lengths. Within the barrel, the first effect tends to skew reconstructed times later for higher η. The second effect, because of the location of the front-end electronics, tends to skew reconstructed times earlier for higher η, and this is the effect that dominates. The combination of these two effects induces a timing dependence on η, with a spread in each half-barrel of about 15 ns. Smaller variations as a function of ϕ are induced by clock distribution differences and other effects. By applying proper sampling delay settings, this spread can be reduced substantially. In addition, the reconstruction software utilizes a set of per-channel calibration constants to synchronize the mean timing of energy measurements to less than 1 ns.

4.2.2 Timing uncertainty from shower fluctuations

Fiber lengths also differ within each calorimeter cell along the radial coordinate, but in this case there are no means available to compensate for these differences. Since the signals from all the scintillator layers comprising one cell are optically summed, and the optical path lengths are not equalized across the layers, the resulting signal is smeared in time. For hadrons, which exhibit large shower-to-shower fluctuations in longitudinal development, the optical summing of layers imposes a limit on the timing resolution, estimated to be approximately 1 ns. For signals with uniform energy deposit in each layer (such as those arising from the beam-collimator interactions described later), the resolution is not limited by shower-development fluctuations and can be significantly smaller than 1 ns.

4.2.3 Time slew injected by front-end electronics

The QIE ASIC input stage has an amplitude-dependent input impedance, which induces a "time slew" that increases with lower energies. It was determined that this time slew could be reduced or increased with different input amplifier configurations; however, the trade-off characteristic was an increase or decrease in the consequent induced electronics noise. These effects were seen in test beam data and quantified using test bench measurements, shown in Figure 4.2. The final QIE ASIC configurations for the barrel and endcap were chosen to limit the time slew to the medium case in exchange for somewhat increased noise; the time slew in this case is measured to be

$$\Delta_{\mathrm{slew}} = (3.59\ \mathrm{ns}) \log_{10}\left[\frac{1TeV}{E(TeV)}\right] \quad . \tag{4.4}$$

The maximum value of Δ_{slew} is taken to be 10 ns. In the outer calorimeter, the noise level is a critical factor for muon identification and pile-up is much less important, so the quieter slow characteristics were chosen for the HO QIEs. There was no substantial time slew identified at the time for the forward calorimeters.

The time slew effect is subsequently corrected for during hit time reconstruction according to this parametrization, as mentioned in section 4.1.

4.2.4 Time-of-flight variations for collision products

Several lower-order effects create additional uncertainty and bias in the measured time of arrival for products from collisions in the nominal interaction region.

Since the proton bunches have an extent to them along the z-direction, an interaction can occur over a wider range of z than either of the two other rectangular coordinates. (Rarer production processes such as the decays of longer-lived particles can of course cause secondaries to arrive at an HCAL cell from a vertex displaced some distance from the interaction region.) These are referred to as beam spot fluctuations. These fluctuations have a larger effect on high-$|\eta|$ cells than for the central region. Still, for even these cells the effect is small compared to the other sources of variation previously mentioned.

Additionally, the 3.8T magnetic field bends charged particle trajectories according to their transverse momentum. The change in flight time induced by the arced trajectory, from particles with low momenta (ignoring the probability of decay, scattering or absorption) to those with arbitrarily high momenta (trajectory essentially straight), from the IP to the front face of an HCAL tower in the barrel, is depicted in Fig. 4.3, where ψ is the angle subtended by the arc with length s of a low momentum particle traveling from the interaction point (IP) to the front face of an HCAL tower, which is a distance r_{ff} away.

The Larmor radius of gyration r_g of a singly charged particle in a magnetic field B is given by

$$r_g = \frac{p_{\mathrm{T}}}{eB} \tag{4.5}$$

$$= 3.3 \times \frac{p_{\mathrm{T}}(\,\mathrm{GeV}/c)}{B(\mathrm{T})} \quad \mathrm{m} \tag{4.6}$$

whereas, from Fig. 4.3 it is observed that

$$\sin\psi = \frac{r_{ff}}{2r_g} \tag{4.7}$$

$$s = 2r_g\psi \tag{4.8}$$

$$= 2r_g \sin^{-1}\frac{r_{ff}}{2r_g} \quad . \tag{4.9}$$

In the high momentum limit ($p_{\mathrm{T}} \to \infty$), ψ is small, so that $\sin^{-1}(\psi) \simeq \psi$ and $s \to r_{ff} = 1.777$ m. The low limit is determined by the smallest value of p_{T} that still

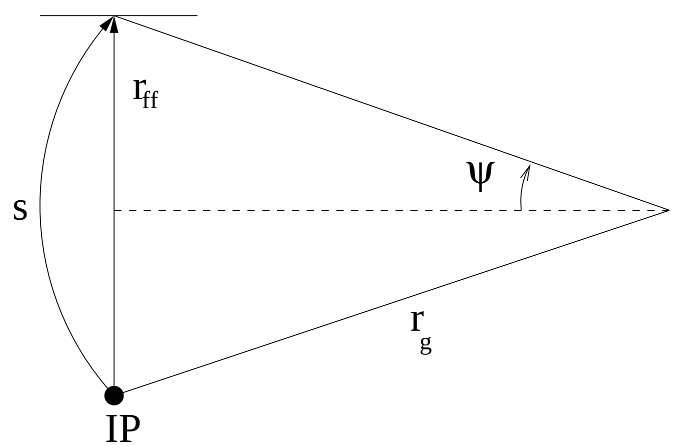

Figure 4.3: Diagram showing the projection onto the transverse plane of low and high momentum trajectories of a charged particle traveling from the interaction point IP to the front face of an HCAL tower.

allows the particle to reach the HCAL tower before being turned back by the magnetic field:

$$\begin{aligned} r_g &= r_{\mathrm{ff}}/2 = \frac{p_{\mathrm{T}}}{eB} \quad , \\ p_{\mathrm{T}} &= \frac{r_{\mathrm{ff}}}{1.74 \text{ m}} \quad \mathrm{GeV}/c. \\ &\simeq 1 \ \ \mathrm{GeV}/c \end{aligned} \tag{4.10}$$

The difference in time for the general case, using $B = 3.8\mathrm{T}$, is:

$$\begin{aligned} \Delta t &= \frac{(s - r_{ff})}{c \sin\theta} \\ &= \frac{1}{c}(2r_g \sin^{-1}\frac{r_{ff}}{2r_g} - r_{ff}) \cosh\eta \qquad (4.11) \\ &= 5.8\mathrm{ns}(\frac{p_{\mathrm{T}}}{\mathrm{GeV}/c} \sin^{-1}\frac{1.02\,\mathrm{GeV}/c}{p_{\mathrm{T}}} - 1.02) \cosh\eta \quad . \qquad (4.12) \end{aligned}$$

(Eq. 4.11 uses the identity $\csc\theta = \cosh\eta$.) This represents a systematic variation of time as a function of the particle p_{T} and η. The η dependence is compensated for by downloading per-tower sampling clock delay adjustments to the front-end electronics, as described in Sec. 3.7.3. The residual p_{T} dependence of the time-of-flight with respect to the high momentum limit is plotted in Fig. 4.4, and is shown to be negligible for momenta that are resolvable from detector noise. For particles that impact the endcap and forward calorimeters, particles with less than 1 GeV/c of momentum can theoretically spiral for indefinite periods of time (particularly for those particles with their η pointed in the barrel region, since they have insufficient momenta to reach the HCAL barrel), again neglecting any potential interactions or decays in the intervening media.

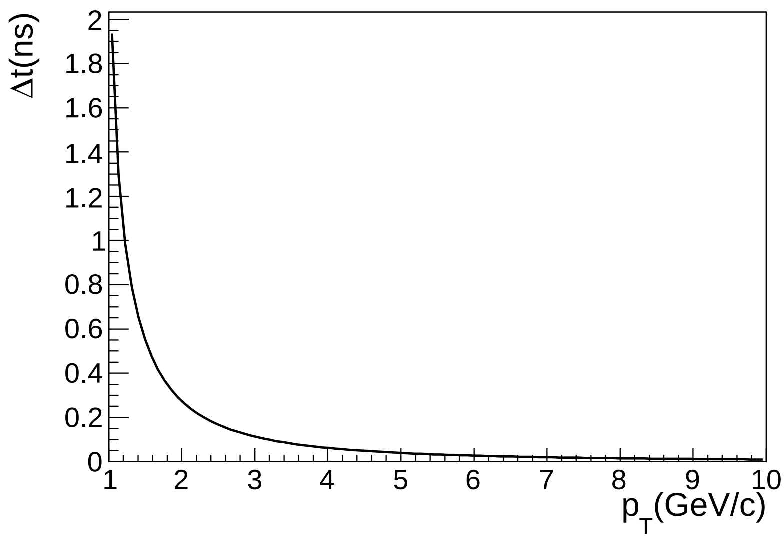

Figure 4.4: The residual dependence of time-of-flight on p_{T} for charged particles reaching the HCAL barrel, due to the Lorentz force, after the η dependence has been removed.

4.3 Validation and Performance Characterization from Test Beam Data

Test beam activities in 2004 and 2006 provide the foundation of timing measurement and validation for HB and HE. The test beam setups for HB for these years were very similar and was described in Section 3.7.4. Position and energy scan runs were taken to determine timing performance for multiple channels (eta and phi coordinates) and energy settings. Data from both HB-only and combined ECAL/HCAL runs were analyzed as described below. Additional beamline elements such as Cherenkov counters, beam halo and time-of-flight scintillators were used for particle identification and veto, to boost the purity of the beam events during post-analysis.

4.3.1 Pulse Reconstruction

Initial assessments of the precise time reconstruction algorithm indicated that perhaps the simulation pulse shape used to generate the correction function was no longer correct when ran against actual data. In order to validate the simulation pulse shape it became necessary to derive the pulse shape from test beam data. This section describes how the pulse shape reconstruction and validation were performed.

For pulse reconstruction a single 300 GeV pion run was selected from TB2004. From this run only those events were chosen with reconstructed energy greater than 200 GeV, and with a TDC phase within the expected range of 32 units, plus or minus 1 unit on each end. The pulse reconstruction was performed again on a single 150 GeV run from TB2006, cutting on hit energies greater than 100 GeV.

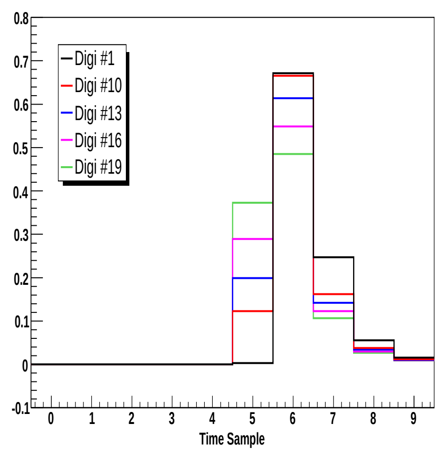

Figure 4.5: Digis A_k, overlaid

As mentioned in the previous section, the read-out ADCs for HB and HE are charge summing, not voltage sampling. The resulting digitized pulse shapes, or "digis," are therefore an integration of the underlying pulse shape. Reconstructing the underlying pulse shape therefore required a numerical differentiation technique that utilizes the phase between particle arrival and the integration clock, as measured by the TDC, which ran at 32 times faster than the sample clock rate. This allowed the separation of the data sample into subsamples S_n, with n =1..32, ordered by TDC phase. These subsamples represent the integration of the pulse $P(t)$ shifted successively by the TDC bit resolution ($\Delta t = 0.78$ ns). Then,

$$\langle I_m \rangle_{S_{n+1}} - \langle I_m \rangle_{S_n} \simeq \int_{\tau}^{\tau+\Delta t} P(t)dt \simeq P_{\text{avg}}(\tau)\Delta t \quad , \qquad P_{\text{avg}}(\tau) \simeq \left.\frac{\Delta\langle I \rangle}{\Delta t}\right|_{\tau} \quad , \tag{4.13}$$

where $\langle I_m \rangle_{S_n}$ is the average integrated amplitude for time bin m of data subsample S_n, $\tau = m\Delta t$ is the phase within that time bin, and $P_{\text{avg}}(\tau)$ is the average value of $P(t)$ over Δt at $t = \tau$. Equation 4.13 is valid to reconstruct the first 25 ns of the pulse shape, for which $m = 0$. For each remaining 25 ns interval, bin m is incremented and a second integral term appears in the equation that corresponds to the Δt-sized portion of the pulse “leaving” the time bin. In this manner, the whole pulse was reconstructed to approximately 0.78 ns resolution.

Figure 4.6 shows a comparison of TB2004 and TB2006 reconstructed pulse shapes, as well as the results of the fit, both before (in green) and after (in black) the pre-amp shaping parameter was adjusted. The TB2006 results were consistent with those of TB2004, as expected. The new value for the shaping parameter was put into official use within the collaboration software framework.

Using the new simulation pulse shape, the correction function described in the introduction was generated. The correction function takes the form of a lookup table (LUT); its generation is described subsequently.

The pulse shape digitization was simulated by integrating the simulation pulse over 25 ns bins. The phase of the bins was systematically shifted to cover a total of 25 ns, with a granularity of 1 in 10^{-4}. The weighted peak bin for each shift value was calculated per Eq.4.1 and then normalized to a range of 0 to 1. This value corresponds to the first order time estimate with which the correction would be looked up. At regular intervals of normalized weighted peak bin, the corresponding time shift correction was stored into the LUT. This LUT was then incorporated into the CMS software for online and offline reconstruction. The code takes un-normalized weighted peak bin as an input, and returns a precise time estimate of the hit as an output.

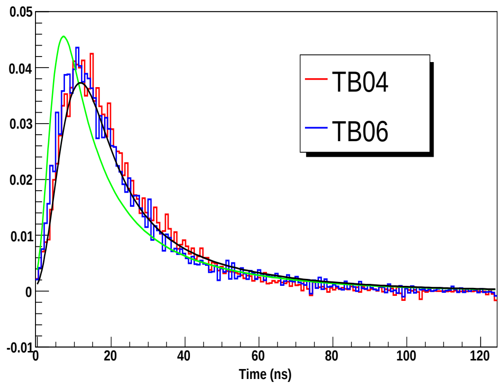

Figure 4.6: Reconstructed pulse shapes from TB2004 and TB2006, plotted against pre-fit and post-fit simulation shapes

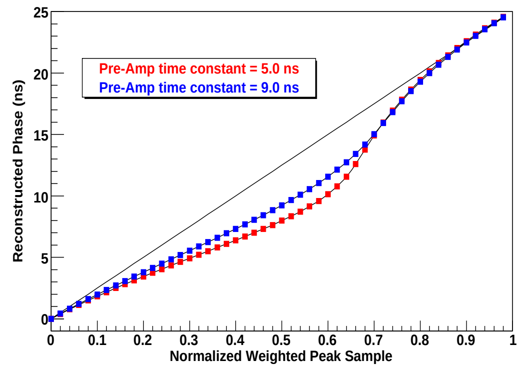

Figure 4.7: The correction function applied in signal reconstruction software to compensate for pulse shape asymmetry, pre- and post- pulse shape reconstruction.

The results of the LUT generation, both for pre- and post-pulse reconstruction, are shown in Figure 4.7. The straight line represents a linear relationship between weighted peak bin and precise reconstructed time; this would correspond to the case of a perfectly symmetric pulse shape, for which a correction function would not be required. The blue and red data sets represent the correction function determined for the actual HB pulse shape, both before and after the pre-amplifier shaping parameter was adjusted, respectively.

4.3.2 Timing Resolution

To measure both the channel-to-channel variations and the hadronic timing resolution limit of the HCAL, a 150 GeV pion beam was directed at every cell in the unit under test. From these data the variation of the timing of signals as a function of η between HCAL cells in the barrel was mapped. As the test setup mimicked the geometry and fiber lengths of the final barrel detector, a set of final sampling delay settings could be derived. The HCAL timing resolution was determined by removing the channel-to-channel variations and combining the data. A Gaussian function was then fitted to the distribution of the leading energy deposit from each event, producing a best-fit width of $\sigma = 1.2$ ns (Fig. 4.8). This result is consistent with the expected effect of the uncorrectable sources of timing spread described in Sec. 4.2, averaged over many hadronic shower events. The measured resolution is consistent across the full set of channels studied.

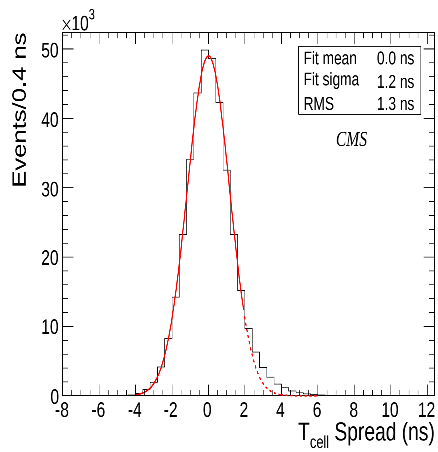

Figure 4.8: Resolution performance of the HCAL barrel from 150 GeV pion test beam data. The non-Gaussian tail is attributed to a combination of factors: 1) beam contamination from electrons and photons that shower in the first layers of the HCAL and thus reconstruct with later signal times, and 2) ion feedback within the HPD that adds low energy late in time to the pulse; the effect on hit time from this noise source becomes more significant as the primary in-time signal energy decreases.

The variation of HCAL timing resolution as a function of energy was also measured with pion beam data. In this measurement the HCAL unit under test was paired with its corresponding section of the ECAL in front, as in the CMS detector. Events in two categories were considered: those with no interaction in the ECAL (<1 GeV energy deposited) and those with a significant interaction (>5 GeV energy deposited). The results indicate that the presence of the ECAL does not substantially alter the timing resolution of the HCAL as a function of energy (Fig. 4.9(a)). CMS software was subsequently adjusted by smearing the times of simulated HCAL energy deposits so that simulated data of the test beam configuration exhibited the same energy-dependent time resolution (Fig. 4.9(b)).

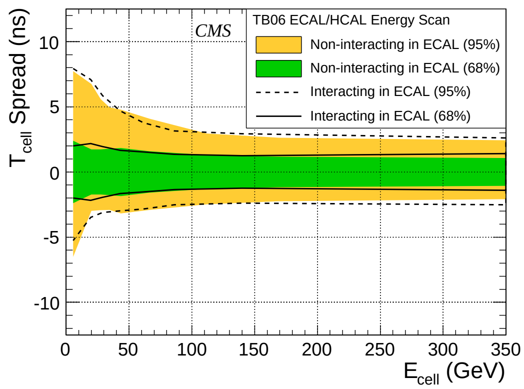

Figure 4.9: (a) Timing resolution as a function of energy measured during test beam runs in 2006, showing the consistency of time reconstruction for particles that begin showering in the ECAL (lines) and those that do not (areas). (b) Timing resolution as a function of energy of reconstructed deposits generated from CMS simulations. The lines marked “Time Filter” indicate the boundaries of a timing window discussed later and used to accept or reject deposits for distinguishing signal from background.

Chapter 5

Data Samples

This chapter describes the data and computer simulation ("Monte Carlo") samples used to perform the analysis described in this thesis.

5.1 Collision Data Sample

Data samples used in this analysis were collected from March, 2010 to November, 2010. During this period the LHC provided proton-proton collisions at a center-of-mass energy of 7 TeV. During the course of the year, the LHC operators steadily increased the instantaneous luminosity of the beams, starting from less than $\mathcal{L} = 1\times10^{26}\,\mathrm{cm}^{-2}\,\mathrm{s}^{-1}$, or $1\times10^{-4}\,\mu\mathrm{b}^{-1}\,\mathrm{s}^{-1}$, on "First Physics Day" up to a maximum of over $\mathcal{L} = 2\times10^{32}\,\mathrm{cm}^{-2}\,\mathrm{s}^{-1}$, or over $200\,\mu\mathrm{b}^{-1}\,\mathrm{s}^{-1}$. A plot of the integrated luminosity curve over the period is shown in Figure 5.1. [1]

CMS Data Operations divided this data into two run periods, "Run2010A" occurring before the September 2010 3-week technical stop ($3.1\,\mathrm{pb}^{-1}$) and "Run2010B" ($40\,\mathrm{pb}^{-1}$) occurring after. The data used for this analysis had additional quality restrictions placed on it; only runs certified with all subsystems marked "good" were included in the analysis, reducing the total analyzed data set over both runs to $36.1\,\mathrm{pb}^{-1}$.

Managing a change in instantaneous luminosity over the course of the year that spans six orders of magnitude presented a challenge both to the trigger and data acquisition groups and to the data operations and processing groups. For the HLT trigger menu

[1] https://twiki.cern.ch/twiki/bin/view/CMSPublic/LumiPublicResults2010

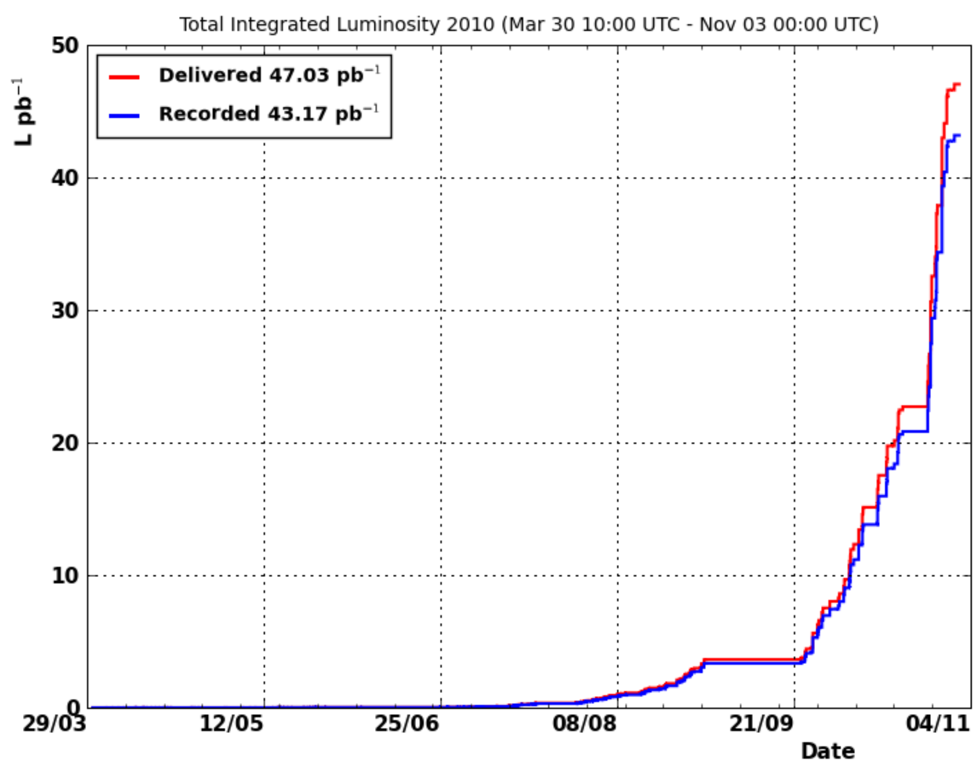

Figure 5.1: Total integrated luminosity as a function of time delivered to and recorded by the CMS detector during the year 2010.

development team, the challenge was to maintain a reasonable "to tape" acquisition rate while servicing the needs of the individual physics analysis groups. They had at their disposal several tools to throttle the trigger rate as luminosity increased: they could increase the p_{T} threshold of the triggered object, or they could "prescale" the trigger by accepting only 1 out of every N such triggers, or they could add other conditions to the trigger, for instance, requiring quality conditions on muons, or requiring two low p_{T} threshold objects simultaneously instead of one. The HLT trigger menu team thus produced about 12 major menu revisions over the course of the year's running, with many more minor revisions in between.

In synchronization with these menu changes the data operations teams designed "primary datasets" classified primarily by the major physics objects of interest: for example, "/Electron", "/Jet", "/Mu"; these classifications became more refined, and the number of primary datasets increased, over the course of the year. The data acquired by sets of similar HLT trigger paths were merged into "streams" that together defined the content of the primary datasets.

Such numerous changes also pose a challenge to analyses such as this. In order to avoid proliferation of systematic studies for different triggers, or for triggers that evolved over time, these complexities were reduced by considering only two unprescaled triggers, which represent the early and later data-taking periods.

In particular, this analysis makes use of the "/Mu" dataset, which over the course of the year had anywhere from a dozen to two dozen HLT trigger paths assigned to it; the two most consistently available trigger paths, unprescaled, were called "HLT_Mu9" and "HLT_Mu15", which are relatively simple single muon triggers with p_{T} thresholds of 9 and 15 GeV/c, respectively, and no other associated quality requirements (such as isolation). The data for which HLT_Mu9 existed unprescaled in the menu are classified as being from the "low luminosity" portion of the run period, and covers approximately 8 pb^{-1} from Run2010A and part of Run2010B. (This requirement excludes the earliest data taken in Run2010A, before this trigger path came into existence; the total amount of data excluded is far less than $0.1\,\mathrm{pb}^{-1}$, however.)

After that point, in order to throttle the trigger rate from "HLT_Mu9", the trigger prescale factor had to be increased; at this point the analysis makes use instead of the "HLT_Mu15" trigger path for the remainder of Run2010B, which is classified as the "high luminosity" portion, covering approximately 28 pb^{-1} of collected data.

5.2 Simulated Signal Samples

The signal samples consisted of 105 Monte Carlo simulated samples generated using PYTHIA 6 [24], one for each M_{W_R},M_{N_R} mass hypothesis. The mass hypotheses for the W_R boson were allowed to vary from 700 GeV/c^2 (to provide overlap with the Tevatron exclusion region) to 1600 GeV/c^2 in 100 GeV/c^2 increments. The mass hypotheses for the heavy neutrino N_R were allowed to vary from 100 GeV/c^2 to (M_{W_R}-100 GeV/c^2) in 100 GeV/c^2 increments. PYTHIA was set to generate 10,000 events containing direct production of the W_R for each input mass. The W_R was also restricted by the mass settings of the other neutrino flavors to decay to a heavy muon neutrino $N_{R,\mu}$. A plot of the leading order PYTHIA cross section as a function of M_{W_R} and M_{N_R} is shown in Fig. 5.2; the selected mass point values are highlighted. These samples were then normalized to the same integrated luminosity as in data, using also the calculated NLO k-factors shown in Table 5.1.

M_W (GeV/c^2)	k
700	1.32
800	1.32
900	1.32
1000	1.31
1100	1.30
1200	1.30
1300	1.29
1400	1.28
1500	1.28
1600	1.28

Table 5.1: K-factor values as a function of M_{W_R}

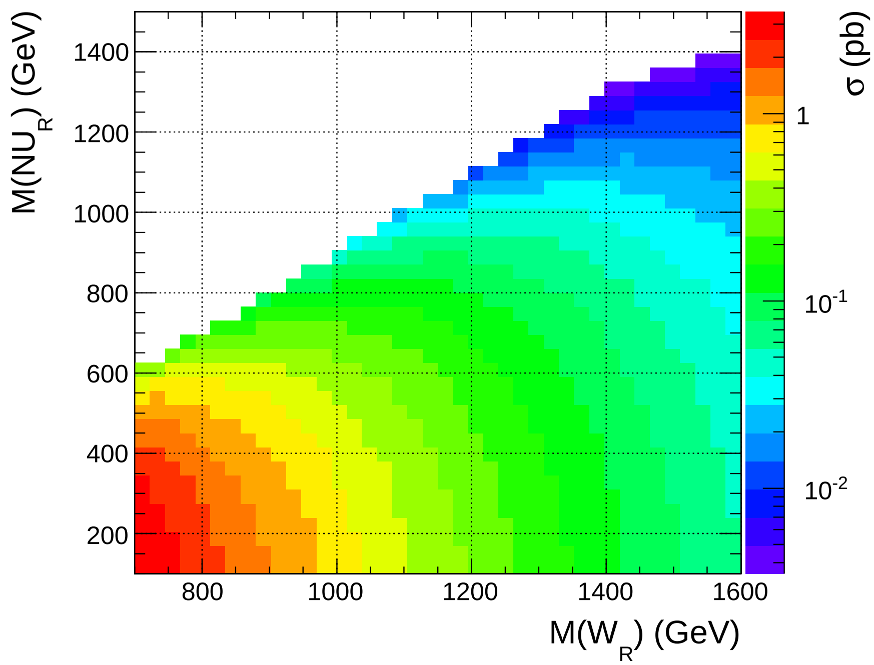

Figure 5.2: Fig. 2.2 zoomed in to that region of mass phase space over which the PYTHIA MC signal samples were generated. A grid of 105 mass hypotheses was chosen to span the space depicted here with a 100 GeV/c^2 grid spacing in both axes.

5.3 Simulated Background Samples

The electroweak background samples were generated in simulation by the CMS collaboration according to Table 5.2. The hadronic dijet background was estimated from the collision data sample as described in section 7.3.

Table 5.2: Summary information for the Monte Carlo samples used in the analysis including the process name, generators used, the number of generated events, cross section and associated error, and the cross section order and provenance (NLO or NNLO). The Z+jets and W+jets samples are generated in separate files for 0-5 jets in several p_{T} bins.

Process	Generator	N events	σ, pb	$\delta\sigma$, pb	Order/Provenance
Z+jets	ALPGEN [44]+TAUOLA [45]	2.5M	3160	-	NNLO [46]
W+jets	ALPGEN +TAUOLA	7.2M	31314	1558	NNLO [46]
$t\bar{t}$	MadGraph [47]+TAUOLA	1.2M	167	24	Measured [48]
Inclusive WW	PYTHIA 6+TAUOLA	2M	43	1.5	NLO [46]
Inclusive WZ	PYTHIA 6+TAUOLA	2M	18.2	0.7	NLO [46]
Inclusive ZZ	PYTHIA 6+TAUOLA	2M	5.9	0.15	NLO [46]
$tW \rightarrow bl\nu$	MadGraph	500k	10.6	0.8	NLO [46]

Chapter 6

Object and Event Reconstruction and Selection

> It is the glory of God to conceal things, but it is the glory of kings to search things out.
>
> —King Solomon

The challenge presented to the designers of CMS reconstruction software, both for online (HLT) selection and offline analysis, is essentially to transform faithfully the detector-based signals (e.g., calorimetric deposits, tracker or muon station "hits"), which present little in the way of physical insight into the event being studied, into reconstructed objects that have a great deal of physical content. In this transformation the details of detector design fade into the background, and the properties of the underlying particle or particles arising out of the collision event come to the fore, properties such as energy, transverse momentum, charge, and so on. The panoply of reconstructed objects in CMS includes electrons, photons, muons, "jets" (which are collimated streams of hadronic and electromagnetic particles arising from the hadronization of a high p_{T} gluon or quark), and missing transverse energy (MET). This analysis concerns itself primarily with reconstructed muons and jets, but also with electrons for one of the background processes studied; this chapter describes how these objects are first reconstructed in general, and then selected in particular for the analysis presented herein.

6.1 Jet Reconstruction and Selection

Jets are reconstructed from combinations of HCAL and ECAL cells located in the same region of (η,ϕ) space (cf. Sec. 3.3); these cell combinations are referred to as calorimeter "towers". Towers are clustered together using the anti-k_{T} clustering algorithm [49]. A jet "cone" is visualized with its vertex located at the collision vertex, and its central axis co-aligned with an energy-weighted axis through the center of the jet. Jet clustering algorithms typically make use of such cones to determine what tracks or towers to include in the total jet energy/momentum calculation; a cone with angular radius $\Delta R = \sqrt{(\Delta\eta)^2 + (\Delta\phi)^2} = 0.5$ was used to reconstruct jets for this analysis. Jets are required to pass the following quality requirements, which are intended to suppress backgrounds from calorimetric noise:

1. The number of calorimeter towers contributing 90% or more of the jet's energy must exceed one.

2. The electromagnetic fraction of the jet (i.e., the fraction of the jet's energy that comes from the electromagnetic calorimeter) must exceed 1%.

3. The fraction of the jet's energy that comes from a single photodetector in the hadron calorimeter (which spans multiple towers) must be less than 98%.

In addition, after jet identification and before any selection on the jet p_{T} is performed, jet energy scale corrections are applied. The corrections are factored into stages; currently two stages of corrections are applied. The first stage levels the jet response as a function of pseudorapidity, and the second stage levels the jet response as a function of p_{T}. These corrections are derived currently from MC truth; therefore the data are subjected to a third residual correction in the relative energy scale that compensates for known differences between the MC and data [50].

Once quality criteria are met, two jets reconstructed with $p_{\mathrm{T}} > 40$ GeV/c and $|\eta| < 2.5$ (within the silicon tracker η acceptance) are required. In the case of more than two jets passing, the two highest p_{T} jets are chosen.

6.2 Muon Reconstruction and Selection

Muons are reconstructed offline from a combination of silicon tracker hits and muon chamber hits, as described in [51]. For each event two such reconstructed muon objects are required.

Initially, both muons are required to pass a set of loose requirements. The kinematic loose requirements include $p_{\mathrm{T}} > 20$ GeV/c and $|\eta| < 2.4$. The other requirements include enforcement of track fit quality and agreement between the silicon tracker and muon detector subsystems, and muon isolation defined as an upper limit of 10% of the muon p_{T} on the allowed Σp_{T} of tracks surrounding the muon within an angular cone of radius $\Delta R < 0.3$. Since muons rarely form jet candidates, muons found within $\Delta R = 0.5$ of a valid jet are also rejected.

One of the two muons must then pass a set of tighter quality requirements. This includes a track fit impact parameter of less than 2 mm from the reconstructed beam spot, which suppresses cosmic ray backgrounds, tighter track fit quality requirements, and a trigger matching requirement that ensures this higher quality muon is represented in the list of objects triggered for that event. The trigger-matching is performed by requiring that the candidate offline-reconstructed muon be within $\Delta R < 0.2$ and $\frac{|\Delta p_{\mathrm{T}}|}{p_{\mathrm{T}}} < 1.0$ of one of the muon trigger objects for the chosen trigger path as defined in 5.1. In the case of multiple muons passing these requirements, the muon of interest is required to have the smallest ΔR to its associated muon trigger object. This matching is required within a restricted η region of $|\eta| < 2.1$. (Beyond this region the muon trigger efficiency drops substantially, as described in [51]).

Together the two muons and two jets are required to originate from vertices whose Z projections are within 0.03 cm of each other, which suppresses in-time pileup backgrounds; the Z-coordinates of uncorrelated vertices are typically separated by about 1 cm.

6.3 Electron Reconstruction and Selection

While this analysis focuses primarily on the signal decays into the muon channel, electrons are reconstructed for the sake of studying one of the primary backgrounds, top quark pair production ($t\bar{t}$) and decay (Sec. 7.1). The decay of the quark-antiquark pair to one electron and one muon was studied in collision data in order to cross-check the predicted rate of $t\bar{t}$ from computer Monte Carlo simulations. The reconstruction of electrons for this analysis is described here.

Detailed information about electron reconstruction and identification in CMS during this running period can be found in [52]. Electron candidates are reconstructed offline [53] starting from clusters of energy deposits in the ECAL crystals. The energy from electrons is spread out in ϕ because of the bending of their trajectories by the magnetic field and because of the "bremsstrahlung" radiation they emit in the process. Therefore in the reconstruction of electron candidates, clusters of energy deposits are combined with other clusters of deposits along ϕ, creating "superclusters". For this analysis a transverse energy threshold of $E_T > 20$ GeV is applied to superclusters.

Subsequently, special selection criteria are applied to electrons, criteria that were developed by the CMS collaboration specifically optimized for electrons with energies of hundreds of GeV. To meet these selection requirements, the electron must have been seeded by an ECAL supercluster (as opposed to a tracker track) and be spatially matched to a reconstructed track in the central tracking system in both η and ϕ. Electron candidates must also have a shower shape consistent with that of an electromagnetic shower, and be isolated both with respect to other energy deposits in the calorimeter and to reconstructed tracks in the central tracking system. A full breakdown of the electron selection criteria is presented in Table 6.1.

To remove fake electrons produced by the overlap of anomalous ECAL single-APD noise signals with a reconstructed track, a topological cut on the lateral shape of the supercluster associated with the electron candidate [54] is applied. The electron is rejected if the seed energy of the cluster is more than 20 times the sum of the energies of the four adjacent ECAL crystals.

6.4 Event Selection

The signal event candidates were selected by requiring at least four reconstructed objects that pass the above criteria in the final state; additionally, one muon (not necessarily the higher quality muon) is required to have $p_T > 60$ GeV/c. To suppress Standard Model $Z \to \mu\mu$ backgrounds, since the Z-boson mass is approximately 91 GeV/c^2, a dimuon

Table 6.1: Summary of the High-energy electron selection criteria. Only electrons whose reconstruction were seeded by ECAL superclusters are considered.

Variable	Barrel	Endcap
Supercluster position	$\lvert\eta_{SC}\rvert < 1.442$	$1.56 < \lvert\eta_{SC}\rvert < 2.5$
$\Delta\eta_{in}$	< 0.005	< 0.007
$\Delta\phi_{in}$	< 0.09	< 0.09
H/E	< 0.05	< 0.05
Cluster shape	$E^{2x5}/E^{5x5} > 0.94$ OR $E^{1x5}/E^{5x5} > 0.83$	$\sigma_{i\eta i\eta} < 0.03$
ECAL + HCAL$_{\text{Depth 1}}$ Isolation (GeV)	$< 2 + 0.03 \times E_T$	$< 2.5 + 0.03\times$ $\max(E_T - 50), 0)$
HCAL$_{\text{Depth 2}}$ Isolation (GeV)	N/A	< 0.5
Track p_T Isolation (GeV/c)	< 7.5	< 15

mass requirement of ($M_{\mu\mu} > 200$ GeV/c^2) is imposed. Additional studies indicated that this value of dimuon cut was optimal within approximately 10% deviation from the calculated exclusion limit across all signal hypothesis (Fig. 6.1). The final event requirement is imposed on the reconstructed invariant mass for the combination of the two jets and two muons ($M_{\mu\mu jj}$), which would be the candidate reconstructed mass for the heavy right-handed W boson ($M_{W_R}^{\text{cand}}$). For this analysis, $M_{\mu\mu jj} > 520$ GeV/c^2.

The total effect of these requirements on the final numbers of events for each of the signal samples is shown in Table 6.4. The event selection impacts low-mass neutrino hypotheses the most because the neutrino is highly boosted and its decay products typically fail the separation and isolation requirements described previously.

M(W_R) =	0.7 TeV/c^2	0.8 TeV/c^2	0.9 TeV/c^2	1.0 TeV/c^2	1.1 TeV/c^2	1.2 TeV/c^2	1.3 TeV/c^2	1.4 TeV/c^2	1.5 TeV/c^2	1.6 TeV/c^2
M(N_R) (GeV/c^2)										
100	17 (9.4%)	7.9 (7.9%)	4.1 (6.9%)	2.2 (6.3%)	1.2 (5.5%)	0.65 (4.7%)	0.32 (3.6%)	0.19 (3.2%)	0.12 (3.1%)	0.069 (2.7%)
200	45 (28%)	27 (30%)	16 (29%)	9.3 (28%)	5.5 (26%)	3.3 (25%)	1.9 (23%)	1.1 (20%)	0.67 (18%)	0.42 (17%)
300	49 (37%)	32 (40%)	20 (42%)	13 (43%)	8.2 (43%)	5.1 (41%)	3.2 (40%)	2.1 (39%)	1.3 (38%)	0.83 (35%)
400	38 (39%)	29 (46%)	20 (48%)	13 (50%)	8.7 (50%)	5.8 (50%)	3.7 (50%)	2.5 (50%)	1.6 (48%)	1.1 (48%)
500	21 (37%)	21 (47%)	17 (52%)	12 (54%)	8.5 (57%)	5.8 (58%)	3.8 (57%)	2.5 (56%)	1.7 (56%)	1.2 (56%)
600	4.9 (26%)	11 (43%)	12 (53%)	9.6 (57%)	7.3 (59%)	5.2 (60%)	3.7 (62%)	2.4 (61%)	1.7 (61%)	1.2 (60%)
700	–	2.7 (33%)	6.1 (50%)	6.4 (56%)	5.5 (59%)	4.3 (62%)	3.1 (63%)	2.3 (64%)	1.6 (65%)	1.1 (64%)
800	–	–	1.5 (38%)	3.2 (53%)	3.6 (59%)	3.2 (63%)	2.5 (64%)	1.9 (66%)	1.4 (66%)	1.0 (66%)
900	–	–	–	0.82 (42%)	1.8 (56%)	2.0 (60%)	1.8 (64%)	1.5 (66%)	1.2 (67%)	0.88 (68%)
1000	–	–	–	–	0.45 (44%)	1.0 (57%)	1.2 (63%)	1.1 (65%)	0.92 (67%)	0.71 (68%)
1100	–	–	–	–	–	0.27 (49%)	0.57 (59%)	0.68 (64%)	0.66 (67%)	0.56 (68%)
1200	–	–	–	–	–	–	0.15 (50%)	0.33 (61%)	0.41 (65%)	0.4 (68%)
1300	–	–	–	–	–	–	–	0.088 (52%)	0.19 (61%)	0.24 (66%)
1400	–	–	–	–	–	–	–	–	0.054 (55%)	0.11 (63%)
1500	–	–	–	–	–	–	–	–	–	0.032 (55%)

Table 6.2: Final number of expected events per signal mass point (and associated efficiencies) in 36.1 pb^{-1}.

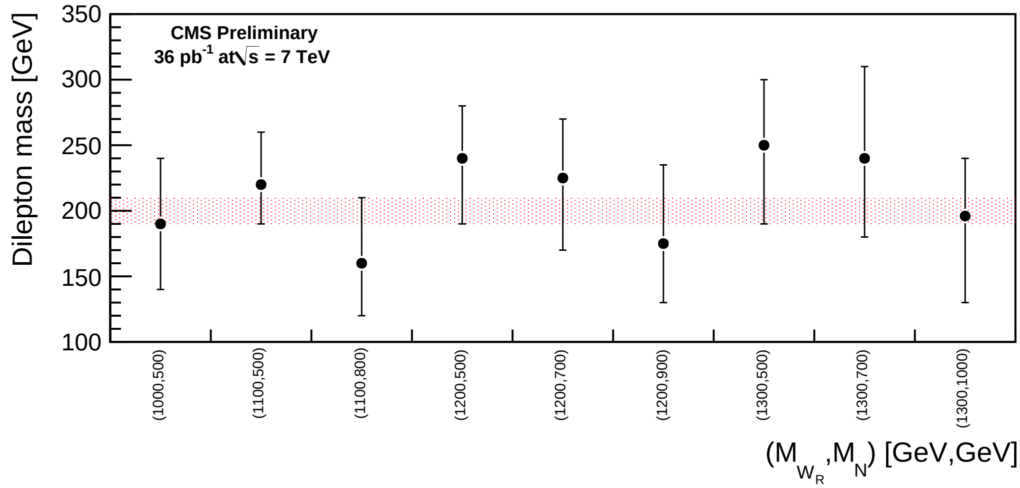

Figure 6.1: Optimal dilepton mass requirement as a function of (W_R, N_R) mass point for selected mass points. The central value for each mass point indicates the $M_{\mu\mu}$ value with the best expected limit and the error bars indicate a $+10\%$ change in the limit with respect to the central value.

Chapter 7

Background Estimation

Backgrounds for the W_R and heavy neutrino search are expected from Standard Model processes with either two real leptons or with fake leptons, for example jets misidentified as leptons. The most important backgrounds are $t\bar{t}$ and Z+jets. Less significant backgrounds include diboson (WW, WZ, ZZ) production and decay, single top, and the ubiquitous QCD multijets background. Most of these backgrounds are modeled in Monte Carlo simulations with normalization to actual data measurements. Since QCD multijet backgrounds are notoriously difficult to model accurately, this background is estimated directly from data. All of these backgrounds and the techniques for estimating their contributions are described below.

The sum total of background events after all the individual estimation procedures described here, with attendant errors, are compared with results from data and signal expectations in Chapter 9. The inputs to the limit setting procedure described in Section 9.2 include the parameters from fits to the exponentially decaying high-mass tails to the invariant four-object mass distributions $M_{W_R}^{\mathrm{cand}}$ of each of these backgrounds.

7.1 Top Background Estimation

One of the most significant backgrounds to the W_R search arises from $pp \rightarrow t\bar{t} + X$ production (Fig. 7.1). A quark/antiquark pair contained within the colliding protons annihilate by means of the strong interaction, producing a gluon, which hadronizes into a top/antitop quark pair. The top quark decays predominantly into a Standard Model

W boson and the next lower quark on the mass hierarchy, the bottom or b-quark. Since the top and antitop quarks are produced in pairs, the two quarks together produce two oppositely charged W bosons, both of which can decay into muon-neutrino pairs with substantial transverse momenta. (Each W boson decays into a muon-neutrino pair about 11% of the time; however, each W boson decay can also proceed as $W \to \tau\nu \to \mu\nu\nu$). Meanwhile, the b-quarks proceed to hadronize and produce two "b-flavor" jets. Such jets are often distinguishable from other types of jets, so that "b-tagging" techniques can be developed to identify them. In particular, an additional muon can be produced from the decay chain of the b-quark.

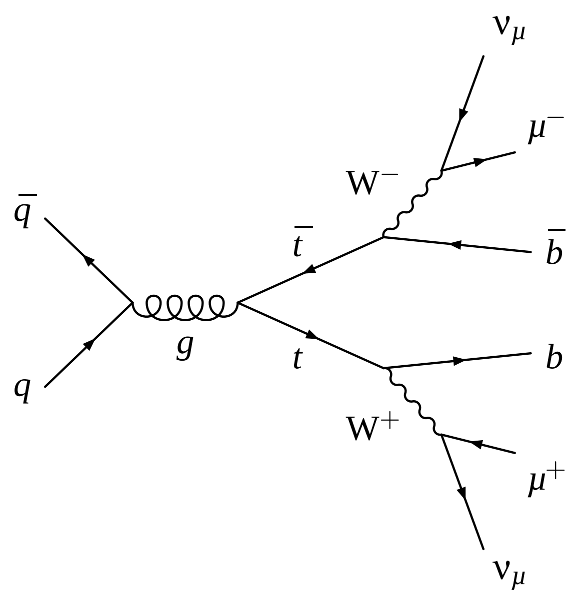

Figure 7.1: Feynman diagram of $t\bar{t}$ production and decay leading to a signal-like final state.

Therefore, in the scenario of muonic decay of the W bosons, the final state for $t\bar{t}$ production is two muons, at least two jets (there may be more), and missing energy from the neutrinos. This explains the challenging nature of the top background to this analysis, since the final state is very nearly the same as the final state from the hypothesized signal. The distinguishing factor for our signal is the invariant mass of the originating products, which are heavier still than the top quark.

The background contribution from $t\bar{t}$ for this analysis is estimated using Monte Carlo simulation. The absolute normalization is taken from the CMS cross section measurement [48] of 167 ± 24 pb. After all selection cuts are applied to the simulated $t\bar{t}$ event sample, the $M_{\mu\mu jj}$ distribution is fitted to an exponential to model the background shape. The fit results are shown in Fig. 7.2.

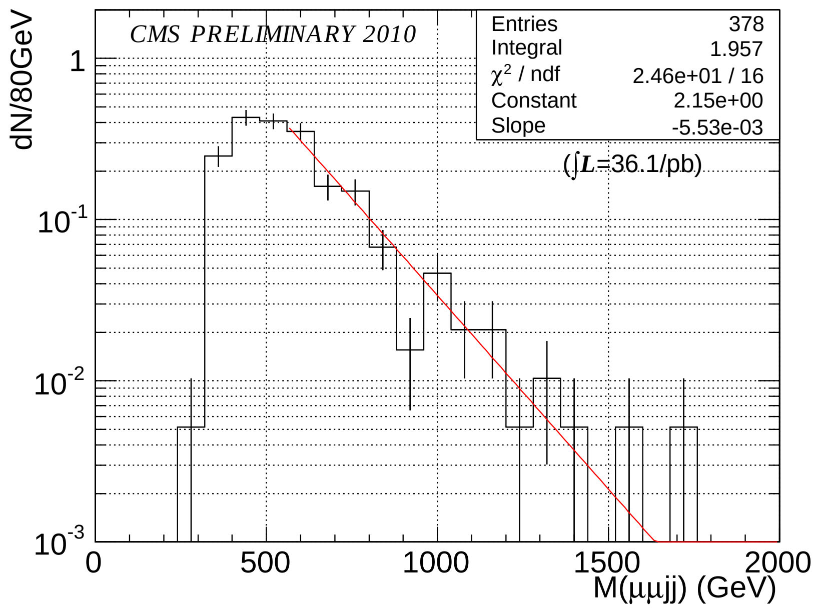

Figure 7.2: Exponential fit to expected $t\bar{t}$ background after all selection requirements are applied.

As a cross-check on the estimation of the $t\bar{t}$ background, our collaborators from INR performed a comparison study of Monte Carlo simulation to data in the $e\mu$ channel, where other Standard Model processes have negligible contribution. They reconstructed one electron according to the requirements described in Sec. 6.3 and one tight muon as defined in Sec. 6.2. They also required two reconstructed jets that satisfy all requirements specified in Section 6.1, and the resulting $e\mu jj$ combination must satisfy the 0.03 cm vertex requirement. While techniques exist to "tag" the jet arising from the b quark in the top decay chain $t \to W + b$, they applied no such b-tagging requirement here, since the selection of the $e\mu$ channel itself removes most other backgrounds, and because of the immaturity of the standard b-tagging algorithms currently available to the collaboration at large. However, they examined the number of b-tagged jets as an additional comparison between data and MC.

The resulting comparison between data and Monte Carlo appears in Figure 7.5, both for the relaxed $p_{\mathrm{T}} > 20$ GeV/c requirement on both leptons and also in Figure 7.6 for a tighter $p_{\mathrm{T}} > 60$ GeV/c selection on of the two leptons. The data are in good agreement with expectations from Monte Carlo, as shown in Figures 7.3 and 7.4 , which implies that no additional corrections to the Monte Carlo normalization are required.

It is noted also that even though the $e\mu$ channel is expected to yield twice as many events as either the ee or $\mu\mu$ channels, the $M_{e\mu}$ distribution in data is still devoid of sufficient statistical coverage beyond 200 GeV/c^2, which emphasizes the need to estimate the $t\bar{t}$ background contribution using simulated events.

The single top production process ($pp \to t \to W + b \to \mu + \bar{\nu}_\mu + b$-jet) represents a relatively minor contributor to the overall background, simply because the second muon is absent, and the rate of fake muons from jets is small. Its contribution was estimated from Monte Carlo, but since the final contribution was negligible (< 0.05 events after all selections are made), its fit parameters were not included in the limit setting procedure described later.

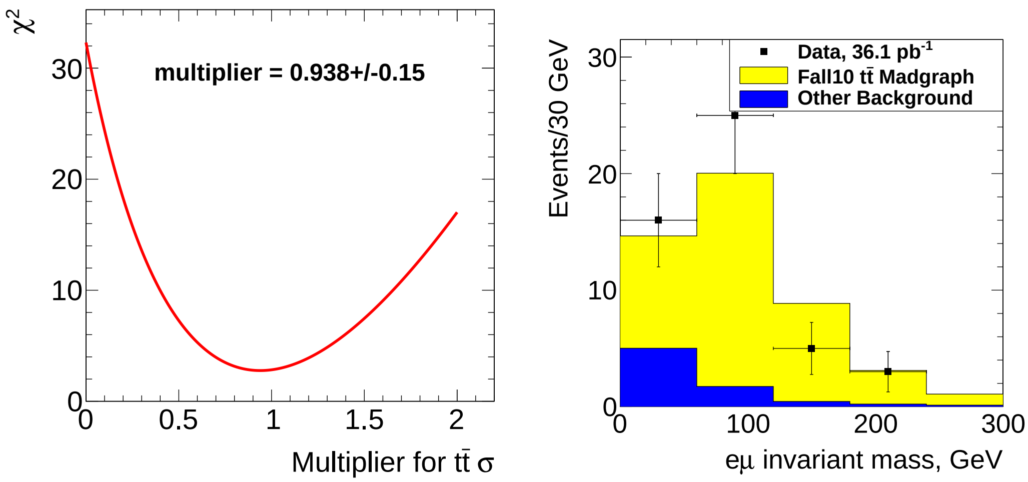

Figure 7.3: Normalization of $t\bar{t}$ Monte Carlo to data in the $e\mu$ channel, $p_T > 20$ GeV/c.

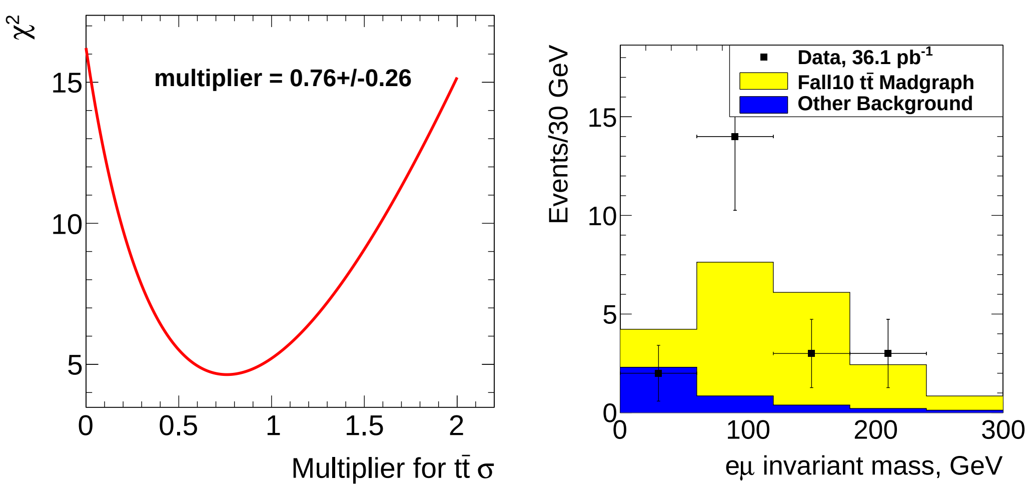

Figure 7.4: Normalization of $t\bar{t}$ Monte Carlo to data in the $e\mu$ channel, where $p_T >$ 60 GeV/c for first lepton, $p_T > 20$ GeV/c for the second lepton.

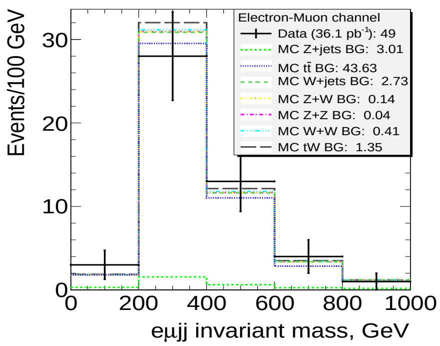

(a) Reconstructed $M_{e\mu jj}$ distribution.

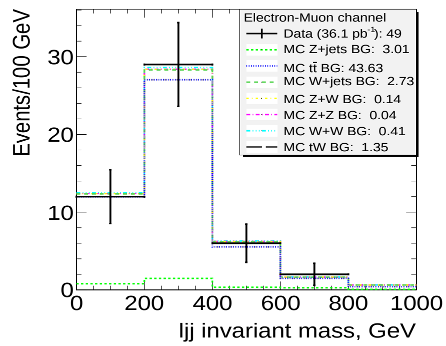

(b) Reconstructed M_{ljj} distribution.

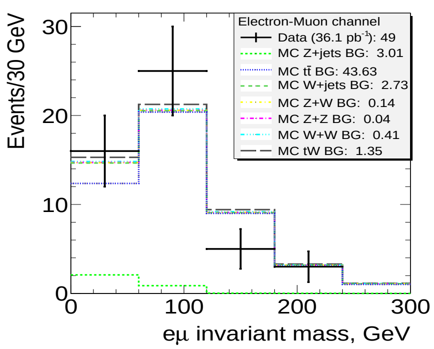

(c) Reconstructed $e\mu$ invariant mass.

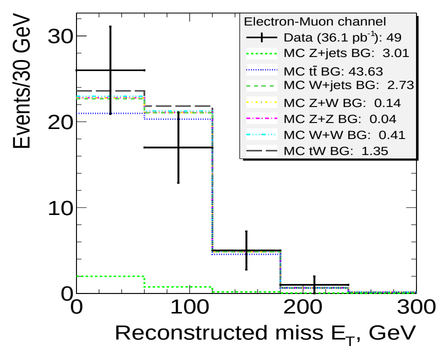

(d) Reconstructed missing transverse energy.

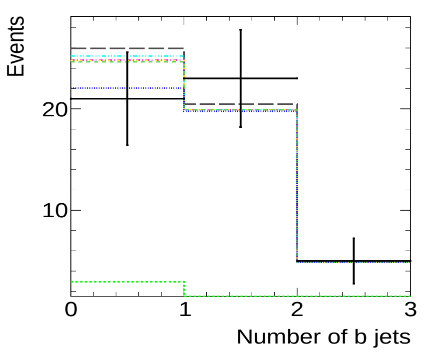

(e) Reconstructed b jet multiplicity.

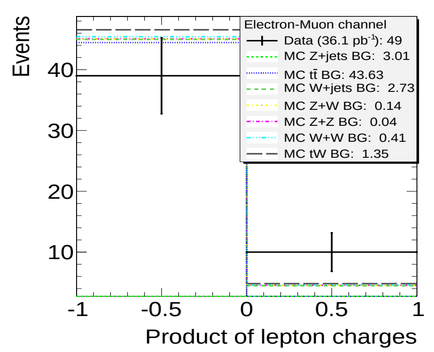

(f) Reconstructed product of lepton charges.

Figure 7.5: Comparison of critical kinematic variables using selected $e\mu jj$ events in data and Monte Carlo with $p_{\mathrm{T}} > 20$ GeV/c requirement on both leptons. The number of expected (MC) or observed (data) events for each sample are included in the legend of each Figure.

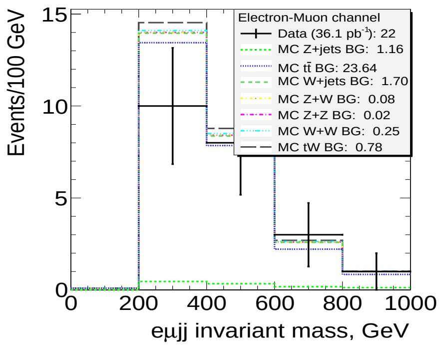

(a) Reconstructed $M_{e\mu jj}$ distribution.

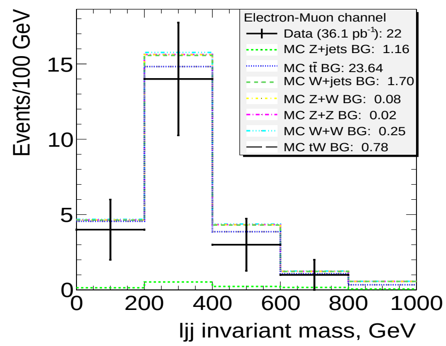

(b) Reconstructed M_{ljj} distribution.

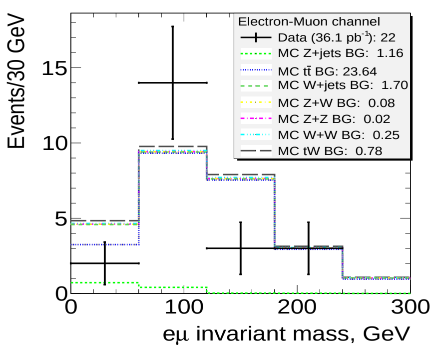

(c) Reconstructed $e\mu$ invariant mass.

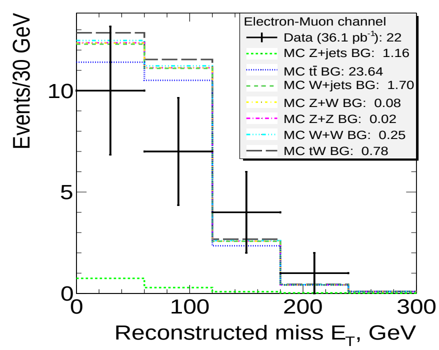

(d) Reconstructed missing transverse energy.

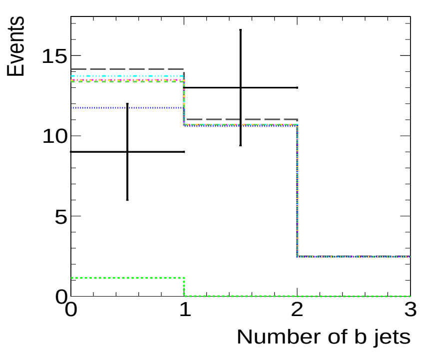

(e) Reconstructed b jet multiplicity.

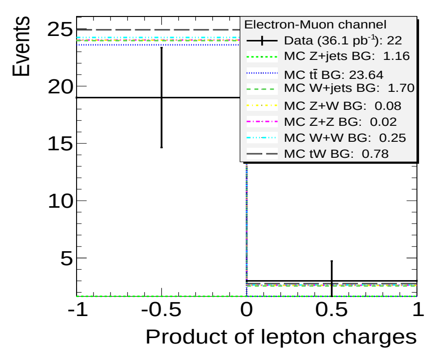

(f) Reconstructed product of lepton charges.

Figure 7.6: Comparison of critical kinematic variables using selected $e\mu jj$ events in data and Monte Carlo with $p_{\mathrm{T}} > 60$ GeV/c for the first lepton and $p_{\mathrm{T}} > 20$ GeV/c required on the second lepton. The number of expected (MC) or observed (data) events for each sample are included in the legend of each Figure.

7.2 Electroweak Background Estimation

The electroweak backgrounds arise from production of one or two Standard Model W or Z bosons. The Z boson in particular, since it is neutral, can decay into two real, oppositely charged muons, whereas for single W boson production, any additional reconstructed muon must be fake. Two additional jets can come about through the radiation by the initial state quarks of two gluons, which then hadronize. Figure 7.7 shows two such possible processes leading to a signal-like $\mu\mu jj$ final state. The difference in this case from a top pair background is the relative lightness of the Z-boson compared to the top quark, and the absence of missing energy from neutrinos.

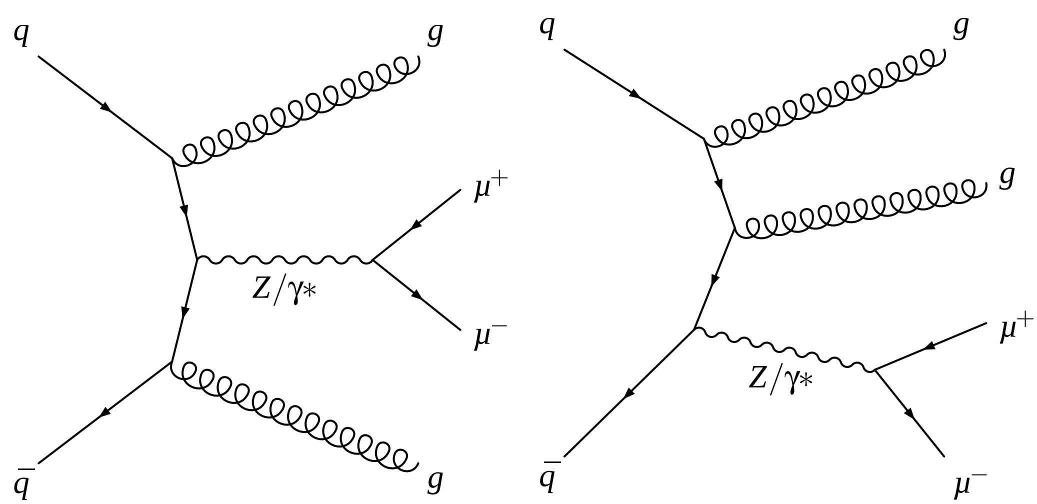

Figure 7.7: Feynman diagrams of Z+X production and decay leading to a signal-like final state.

Two bosons may also be produced in tandem, in all three combinations WW, WZ and ZZ; each one of these combinations can then decay into a number of leptons, including anywhere from zero to four muons of same (only in the case of exactly two muons produced) or mixed charge. The rate of diboson production is substantially less than for single boson production.

The electroweak backgrounds are determined using Monte Carlo simulation. Z+jets, W+jets, ZZ, ZW, and WW processes using the samples shown in Table 5.2. The Z+jet background provided the most background events among all electroweak backgrounds for our analysis. However, there is significant uncertainty in the differential cross section for Z+jet processes due to the high orders of α_s (the strong interaction coupling constant) involved in the Monte Carlo calculations. As a result, the overall Z+jet contribution to the background is constrained using data.

The Z+jets background is estimated (and its uncertainty thereby constrained) by optimizing the weight factor to the NNLO MC calculation of the cross section using a χ^2 fit of the Standard Model Z-boson mass resonance peak from MC to that seen in data prior to the $M(\mu\mu)$ cut. The results are shown in Fig. 7.8. The final $M_{\mu\mu jj}$ distributions and exponential fits for the two largest background contributors, Z+Jets and $t\bar{t}$ are shown in Fig. 7.9.

For the Z+jets background, the fit slope is taken from the distribution before the $M_{\mu\mu} > 200$ GeV/c^2 requirement. This slope is consistent with the slope after the $M_{\mu\mu} > 200$ GeV/c^2, but has a significantly smaller uncertainty due to background Monte Carlo statistics.

The backgrounds from diboson production ($pp \rightarrow VV$, where VV represents WW, WZ, or ZZ), as well as for single W to muon plus jets ($pp \rightarrow W + X \rightarrow \mu\nu j$) were also estimated from Monte Carlo, but as with the single top background, their total background was deemed to be negligible after all selections were applied in comparison to the primary contributors (< 0.05 events apiece), so their fit parameters were excluded from the limit setting procedure described later.

7.3 QCD Background Estimation

The so-called "QCD" background is more properly termed a "hadronic multijet" background; it is so termed since the most common outcome of a collision between two hadrons (protons) is the generation of new hadrons from gluons or quarks according to the rules of Quantum Chromodynamics (QCD). These new hadrons typically form jets as described previously.

It is possible during collision product reconstruction to mistakenly identify a jet as something fundamentally different, such as an electron, a photon, or even a muon. The rate at which this misidentification occurs is called a fake rate from jets for the

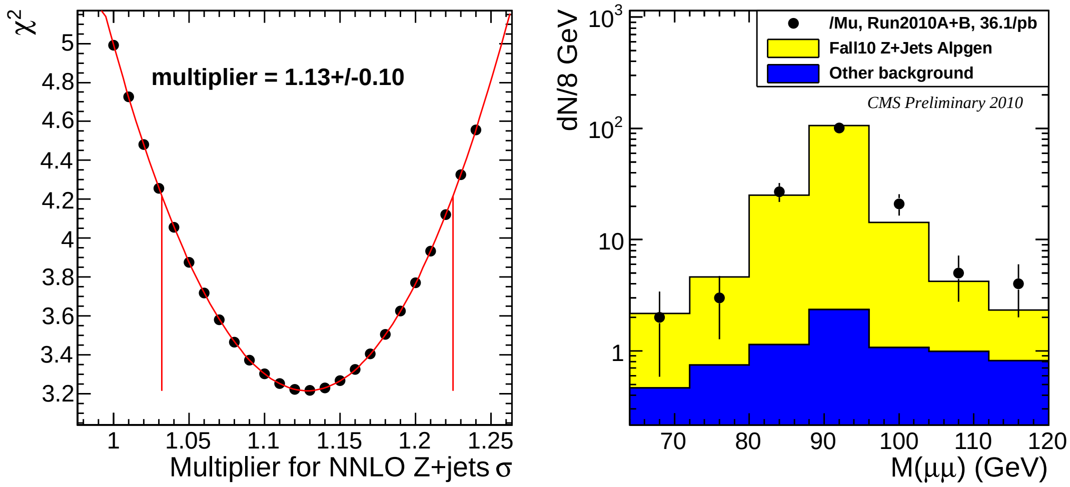

Figure 7.8: Normalization of Z+Jets (NNLO) MC to data in around the Z-boson mass resonance.

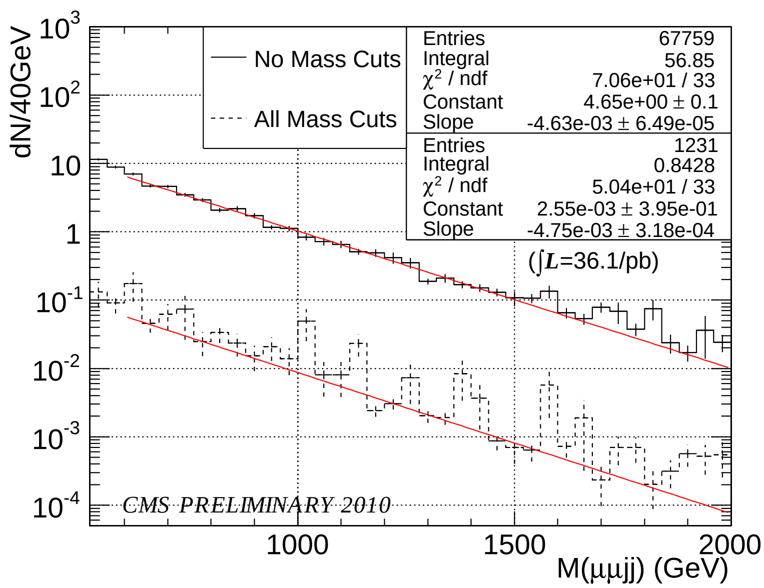

Figure 7.9: Fitted background rate for Z+jets. The high fluctuations seen in the data after all mass cuts is caused by the Z p_{T}-binned nature of the MC samples; the distribution combines low-statistics (large error) events from the tail of a sample with higher-statistics (smaller error) events from the next higher Z p_{T} bin, which are weighted less. The fit reflects the preference for the events with smaller error bars. Since the slope of the two distributions are statistically consistent, the slope from the fit to the no-mass-cut distribution is taken.

misidentified object. Such fake rates must be reduced to a minimum and the remainder estimated in order to enhance the accuracy of the analysis. This is the purpose of the many quality criteria applied during reconstruction to objects such as electrons and muons, in order to minimize the fake rate from jets or other sources. In the case of muons, all of the fake rate from jets comes from actual muons contained within them; however, these muons do not arise from the collision event itself, but from the decay of other particles within the jet occurring "in flight", a distance away from the original event. Such muons arise from the decay of pions (hadrons consisting of two quarks instead of the three found in protons and neutrons) or from heavy-flavor quarks (such as b-quarks) within the jet.

The QCD contribution to the $\mu\mu jj$ distribution was estimated by one of our other University of Minnesota collaborators using a dijet event sample extracted from the Mu dataset. First, a sample of events with a muon and a jet reconstructed "back-to-back" ($\delta\phi(\mu, j) > \frac{9\pi}{10}$) was extracted from the collision dataset. The muon was required to satisfy the loose criteria defined in Section 6.4. The jet was required to satisfy the identification requirements defined in Section 6.1, although the p_{T} requirement was lowered to $p_{\mathrm{T}} > 10$ GeV/c. In order to further enrich the dijet event sample, candidate events were removed from the sample if:

- the missing transverse energy ($E_{\mathrm{T}}^{\mathrm{miss}}$) exceeded 20 GeV,
- a second loose-quality muon existed that met the following combined tracker and calorimeter relative isolation requirement within a cone of $\Delta R < 0.3$ around the muon (excluding the muon's contributions in the sums),

$$\frac{1}{p_{T,\,\mu}}\left(\sum_{i\in\text{tracks}} p_{T,\,i} + \sum_{i\in\text{HCAL cells}} E_{T,\,i} + \sum_{i\in\text{ECAL cells}} E_{T,\,i}\right) < 0.15 \tag{7.1}$$

- a second loose-quality muon was found such that $70 < M_{\mu\mu} < 110$ GeV/c^2,
- a muon was found within the $\Delta R = 0.5$ cone of the selected jet with at least 75% of the total jet p_{T}, or
- any jet with $p_{\mathrm{T}} > 20$ GeV/c was found outside the mu-jet axis.

Additionally, at least 10 GeV of transverse energy in ECAL was required in the vicinity of the muon. Monte Carlo studies imply that an isolated muon from W decay will not deposit significant energy in the calorimeter. This requirement is therefore intended to lower the W+jet pollution in the QCD dijet sample.

For each dijet event, the muon was examined to determine the survival rate for the isolation requirement as a function of the muon quality. The results are presented in Figure 7.10, where in this study a loose quality muon passes the loose identification criteria but fails tight identification requirements. The survival rate increases with muon p_{T} for both muon quality criteria. The relative tracker isolation is expected to allow more fakes at high p_{T}, but it is also likely that the dijet sample may be polluted from good quality (isolated) muons from W decay. For this reason, these results are expected to overestimate the muon survival rate, and consequently should bound the QCD background contribution from above.

Given the QCD survival rate as a function of muon quality and transverse momentum, the QCD background levels in data were estimated using a sample of 4-jet events. For this step, the $\mu\mu jj$ selection described previously was duplicated with the exception of muon-jet separation; each muon was required to be found within $\Delta R < 0.5$ of one of the four jets in the event. Each muon was given an event weight corresponding to the results from the dijet study, taking the muon quality and p_{T} into consideration. An example four-object mass distribution appears in Figure 7.10. The distribution is fit to an exponential function and the fit parameters are included in the Figure.

Nearly all of the QCD background events surviving the muon and jet p_{T} requirements have a dimuon mass below the 200 GeV/c^2 threshold. The lack of QCD statistics makes it impossible to fit the W_R distribution reliably after the full selection is applied. For this reason, the QCD background expectation and exponential slope are taken after all other cuts (ignoring the $M_{\mu\mu}$ requirement) and the expected background are scaled by the fraction of events (4.3%) with $M_{\mu\mu} > 200$ GeV/c^2.

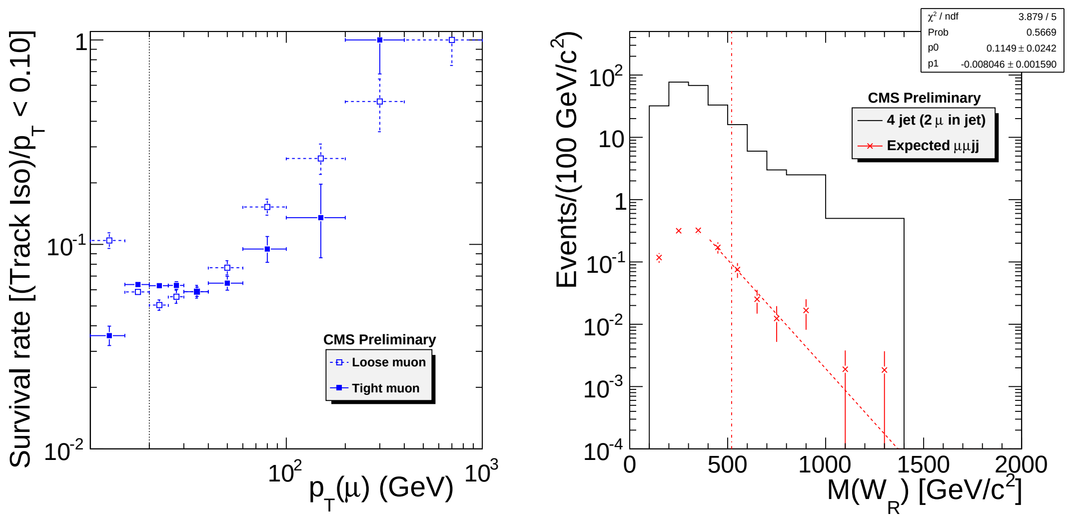

Figure 7.10: Data-based muon fake rate and total QCD background estimate. At left, the estimated probability that a muon from a dijet event will pass the 10% relative tracker isolation requirement is given as a function of muon quality and transverse momentum. At right, the four jet distribution is used to estimate the QCD $\mu\mu jj$ background. The events in the four jet distribution (histogram) are weighted by the muon survival rate to produce an expected $\mu mujj$ distribution from QCD (red points). The distribution is fit to an exponential, where parameter p0 indicates the fitted number of QCD events above 520 GeV/c^2 for the full 2010 dataset and p1 gives the slope of the exponential. In the plot at right, all selection requirements (except $M_{\mu\mu}$ and $M_{\mu\mu jj}$) are applied.

Chapter 8

Systematic uncertainties

> If any one imagines that he knows something, he does not yet know as he ought to know.
>
> —St. Paul

This chapter attempts to detail all of the major sources of uncertainty in the final event yields for the signal and background Monte Carlo simulation samples. The methods for minimizing systematic biases and estimating residual systematic uncertainties in this analysis are described below. The effect of these uncertainties on signal and background yields are summarized in Table 8.3.

One tremendous advantage that the Standard Model Z production background provides for all analyses involving leptons is that the Z-boson mass is very well known (M(Z)=91.1876 GeV/c^2, with a one-sigma decay width to leptons of 3.3658 GeV/c^2, both known to a precision of $\pm 0.0023\%$ [10]); Z decay can produce two quality muons with no inherent missing energy. This provides the analysis with a ready, relatively pure source of muons for use to study various detector and reconstruction effects, albeit within a limited range of muon momentum scale. Several of the studies described below made use of this property of the Z background. One technique used commonly with muons from Z is termed "tag and probe". The tag and probe method in the context of this analysis requires that one of two identified muons has passed whatever selection criteria is being studied; this muon is labeled the "tag". The efficiency of the selection criterion on the probe muon, and the uncertainty on the efficiency is then determined and applied as an estimate of the efficiency of the selection criterion being probed on all real muons.

8.1 Jet energy scale

The energy scale of jets and their uncertainties have been studied in-depth by the CMS Collaboration [50]. As stated previously (Sec. 6.1), the jet energy corrections have been factorized into levels. These corrections and uncertainties were most recently determined from Spring 2010 studies of 2009 data and Monte Carlo simulations and stored in a database of detector conditions. These uncertainties can then be accessed for offline analysis such as the one presented here.

To determine the effect of jet energy scale uncertainty on the final event yields for signal and background, the full event selection was repeated by rescaling jet energies by the uncertainty on their energy scales, with factors both greater and less than unity. The uncertainties are dependent on jet p_{T} and η, and are therefore applied on a jet-by-jet basis when selecting jets and when applying a selection threshold on their p_{T}. To these jet-dependent uncertainties, additional constant uncertainty terms taken for all jets are added in quadrature to yield a total uncertainty, in accordance with the CMS Jet Energy Scale Group recommendations. These additional uncertainty estimates, which are considered to be conservative, include:

- 5% for b-jet scale uncertainty
- 1% for pileup, which is the contribution from other (uncorrelated) interactions occurring during the same bunch crossing
- 1.5% for "calibration changes and release differences".

Subsequently, the total number of events after all selection criteria were tabulated for the nominal case as well as for uncertainty scale factors both greater and less than unity. The total effect on each sample is shown in Table 8.3. In particular, note that the uncertainty for Z+Jets is suppressed because of the normalization to data described in Sec. 7.2. Additionally, since this study is essentially determining the uncertainty of MC compared to data, the QCD background, which is estimated from data, does not participate at all.

For the signal Monte Carlo samples, the effect of jet energy scale uncertainty seems to vary smoothly with the mass hypothesis of the heavy neutrino, since the two jets in the signature originate from its decay. The heavier the neutrino, the more energetic and well-separated are the consequent jets, and therefore the smaller the uncertainty and its effect.

Since the Z+Jets background is normalized to data (cf. Sec. 7.2), the effect of jet energy scale uncertainty is at least partially constrained. To determine the residual uncertainty each of the distributions that were fluctuated up and down were also normalized to data; the residual variation in the final event yield was taken as the systematic uncertainty.

8.2 Muon energy scale

It is expected that for the muon momenta, there will be a certain systematic shift between MC simulation and the real world due to miscalibration or misalignment that is not properly modeled, or a value of the magnetic field, which determines the amount of bending of the muon trajectories, that is different between MC and the real world. Such effects can cause the muon accept/reject rates to differ between MC and real data, based on the analysis selection criteria.

The CMS Collaboration has done detailed studies of this systematic, and estimates a total of 0.5% effect or less on a per-muon basis for muon p_{T} from 10 to 100 GeV/c [51]. To determine how the muon scale uncertainty propagates through this analysis, a study similar to jet energy scale was done for muons as well. A flat, conservative 1% variation on muon p_{T} was applied "up" or "down" to each reconstructed muon during muon and event selection; the effect of this variation leads to a change of one standard deviation in the signal event numbers of less than 1% for most mass hypotheses, but as much as $\sim$2% for the lightest ($M(N_R) = 100$ GeV/c^2) and heaviest ($M(N_R) = M(W_R) - 100$ GeV/c^2) neutrino mass hypotheses. As in the case of jet energy scale uncertainty, the residual Z+jets error after fitting the mass peak is estimated at 2%, and the estimate for QCD was set once again to 0% for the same reasons given above. The total effect on the summed background is estimated to be 4%.

8.3 Muon Trigger Efficiency

The efficiency of the muon trigger system has been studied by the CMS Collaboration, and is known to be less than 100% efficient on a muon-to-muon basis in general. The trigger efficiency for this analysis was studied using the sample of dimuons from data that form an invariant mass within a narrow window around the Z boson resonance. A tag-and-probe method was used to estimate, given that one of the two muons was matched to a trigger object, how often the second muon was also matched. (The trigger-matching criteria is as described in Sec. 6.2). The ratio of matched probe muons to total possible matches was binned as a function of muon p_T. The results are shown in Fig. 8.1.

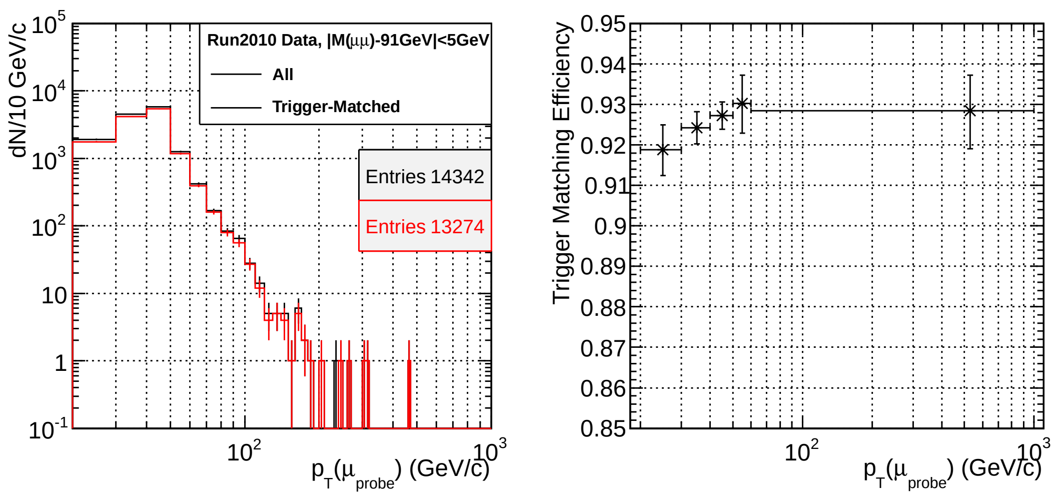

Figure 8.1: Estimate of the trigger efficiency as a function of p_T. The estimate was taken from a sample of dimuons from collision data within a narrow window of the Z-peak.

Since the true performance of the muon trigger system is not well modeled in simulation, a trigger matching criterion was not applied to simulation samples; rather the trigger efficiency determined from this study on data was then coded into the analyzer software to apply directly to each possible trigger selection. Events were randomly rejected based on a probability drawn from a uniform distribution with a cutoff value appropriate to the p_T of the test muon.

The systematic uncertainty in the final result derived from the trigger efficiency uncertainty was estimated by varying the cutoff values according to the statistical errors shown in Fig. 8.1. The results for each Monte Carlo sample are tabulated in Table 8.3.

8.4 Muon reconstruction, identification and isolation

The muon identification and selection efficiency was studied for both data and Z+Jets Monte Carlo; this was done to identify and minimize the systematic bias in efficiency for Monte Carlo, and to estimate the residual uncertainty. A tag-and-probe method was used first to estimate the combined efficiency of "loose" muon identification and track isolation requirements. The requirements for an event to be included in the study were as follows:

- The event was required to have exactly two muons that both exceeded the minimum loose p_{T}, η and jet separation requirements defined in Sec. 6.2.
- The tag muon must have passed all "tight" muon identification (track quality/track matching) and track isolation requirements.
- The two muons together must have formed an invariant mass within 91 ± 5 GeV/c^2.

The ratio of probe muons passing loose identification and track isolation to total possible candidates was binned as a function of muon p_{T}. In a similar way the efficiency for "tight" muon identification was also studied, this time with the candidate probe muon having passed as a prerequisite all loose identification and isolation requirements. The results for both studies are shown in Fig. 8.2. In both cases, good consistency is seen between data and Monte Carlo within statistical precision. Since no trend is observed in the comparison between data and Monte Carlo, a residual uncertainty of 1% is taken for both the single muon loose/isolation and tight identification efficiencies based on combining all events from data into a single bin.

The effect of the uncertainty was estimated by varying the additional rejection rate up or down by one standard deviation. The results for each Monte Carlo sample are tabulated in Table 8.3.

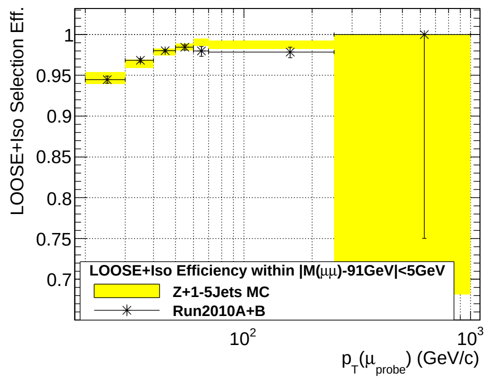

(a) Loose identification and relative tracker isolation comparative efficiencies.

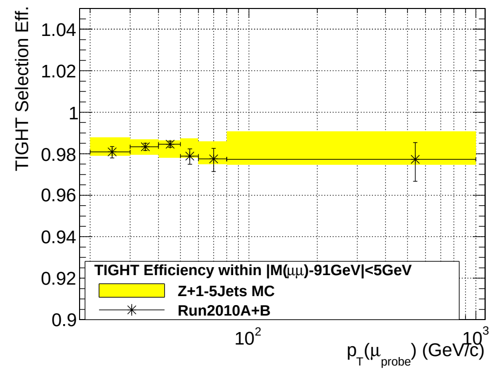

(b) Tight identification comparative efficiencies.

Figure 8.2: Efficiency of muon identification and track isolation requirements from tag-and-probe studies as a function of probe muon p_{T}. The estimates were obtained from samples of reconstructed dimuon events from Monte Carlo and collision data with $86 < M_{\mu\mu} < 96$ GeV/c^2.

8.5 Statistical uncertainty on the MC samples

The statistical uncertainties in the predicted numbers of MC events were calculated as $1/\sqrt{N}$, where N is the raw number of events after the full event selection (see Table 9.1).

8.6 MC modeling of background

An uncertainty of the Z+jet background estimate is derived from a combined analysis of data and MC samples, as described in Sec. 7.2. The uncertainty is taken from the fit shown in Fig. 7.8. For the $t\bar{t}$ background, according to the studies of $e\mu$ events as described above, no renormalization is needed. The statistical accuracy of this check is 14%. For "other backgrounds" the uncertainty of the cross sections (Table 5.2) and the luminosity uncertainty of 4% [55] are combined.

8.7 Initial and final state radiation

Initial and final state radiation (ISR/FSR) are consequences of the quantum mechanical rule that, stated colloquially if imprecisely, says "anything that can happen *does* happen". The Feynman diagrams shown in Fig. 2.1 represent ground state or "tree-level" interactions. However, one may adorn these diagrams with all manner of additional interactions; each vertex added to the interaction reduces the probability of occurrence of the depicted process by the application of a coupling constant that is less than unity.

In the case of initial and final state radiation, one or more additional 'gluon lines' may be added to the initial state or final state quarks, representing a strong interaction process by which a quark radiates a gluon, which forms a jet, and simultaneously reduces the total energy of the quark. The Feynman diagrams shown for Z+Jets production depicts two such examples of interest to this analysis (Fig. 7.7); removing the gluons from these diagrams produces the tree-level single Z boson production diagram. To the charged particles one may also add initial or final state photon lines representing the electromagnetic process by which a charged particle emits a photon that reduces the total energy of the particle. These processes are depicted in Fig. 8.3.

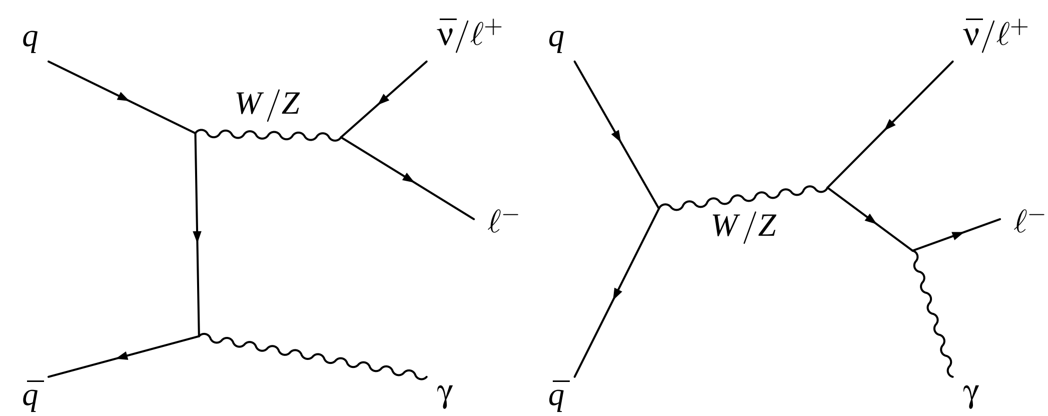

Figure 8.3: Feynman diagrams of example processes exhibiting initial (left) and final (right) state radiation of photons γ.

There are uncertainties in the frequency of occurrence of such processes and the amount of energy that is involved, in particular whether the Monte Carlo accurately models the real world. These uncertainties affect mainly the selection efficiency for both signal and background events. To study this effect, our collaborators from INR produced MC samples of signal event in the electron channel and background ($t\bar{t}$ processes events with modified ISR/FSR parameters (corresponding to larger or smaller ISR/FSR) using the generator PYTHIA and full simulation of the CMS detector. The full selection efficiencies obtained using these samples were compared with the efficiencies from samples produced with nominal ISR/FSR values. The variation is interpreted as a systematic uncertainty on the signal efficiencies due to ISR/FSR modeling.

This analysis adopts the electron channel results for signal and $t\bar{t}$ background. For the Z+Jets background, the process of normalization to data described in Sec. 7.2 constrains the effect of FSR on the analysis results by performing the normalization after applying a 60 GeV p_{T} minimum threshold to the most energetic muon.

8.8 Parton Distribution Function

The Parton Distribution Function (PDF) describes the fraction of momentum of the proton carried by each of its constituent "partons" (quarks and gluons). Uncertainties in the PDF of the proton lead to changes in the total cross section and the selection efficiencies for both signal and background processes.

The PDF uncertainties on the signal and background were estimated by our INR collaborators using an event re-weighting technique implemented in the CMS software. The LHAPDF package [56] was used to assign a weight to each event due to variations in the PDF (according to the known uncertainties on PDF parameters). The selection was performed at the generator level (without full detector simulation and reconstruction) with selection criteria similar to the ones used in the standard selection. The events passing the full selection criteria were re-weighted accordingly, and the selection efficiencies re-calculated. The comparison of the new selection efficiencies multiplied by the new cross section with ones obtained with the nominal PDF set provides an estimate of the systematic uncertainty on signal and background due to PDF uncertainties.

Variation of the PDF leads to uncertainties both in the total cross section for the process being studied as well as changes in the "acceptance" of the analysis; some fraction of events being accepted or rejected differently based on changes in their p_{T} or η.

However, for the $t\bar{t}$ and Z+jets backgrounds the uncertainty on the total cross section was constrained by virtue of their renormalization to data. Therefore the final systematic from PDF uncertainty shown in Table 8.3 is taken as the quadrature subtraction of the cross section uncertainty from the convolved cross section times acceptance uncertainty, quantities shown in Table 8.2. The PDF uncertainties on the signal cross sections and acceptance are listed in Table 8.1.

Table 8.1: Signal PDF systematic uncertainties after full selections are applied.

W_R mass	N_l mass (GeV/c^2)	σ unc.	$\sigma\times$ acceptance unc.
1200	500	7.82%	8.15%
1000	400	7.15%	7.64%

Table 8.2: Backgrounds PDF systematic uncertainties.

BG process	σ unc.	$\sigma\times$ acceptance unc.
$t\bar{t}$	7%	9%
Z + jets	5%	10%

8.9 Factorization/Renormalization Scales

As described in Sec. 2.3, the value of the strong coupling constant α_S is dependent on the energy/momentum scale; it is unclear in many cases what the appropriate scale is when objects of varying p_{T} are in the same event. This therefore represents an uncertainty induced by our imperfect knowledge as modeled in the MC generator software. To study the effect of this uncertainty, our INR collaborators changed the parameter within the generator that defines the boundary between the perturbative (high p_{T} regime) and non-perturbative (low p_{T} regime) parts of the effective Lagrangian. They then notated the relative change in the number of selected signal and background events, keeping the total number of events the same. For the signal samples, variations of less than 0.3% were observed; for the main backgrounds the variations are approximately 8% for $t\bar{t}$ and about 15% for Z+jets. A conservative value of 12% for the uncertainty on the total background is taken.

8.10 QCD Background Estimation From Data

In order to determine the expected uncertainty in the estimation of the QCD background, a closure test was performed. The muon survival probabilities shown in Fig. 7.10 were applied to three jet events, where a muon (of loose or tight quality) was required to be reconstructed within the cone of one of the jets. The muon survival rate determined from this step was subsequently applied to the three-jet event sample to predict the three-object invariant mass distribution $M_{\mu jj}$ formed by two jets and an isolated muon. The results of the closure test are shown in Figure 8.4, where μjj events are rejected if a second muon is found such that $70 < M_{\mu\mu} < 110\ \mathrm{GeV}/c^2$.

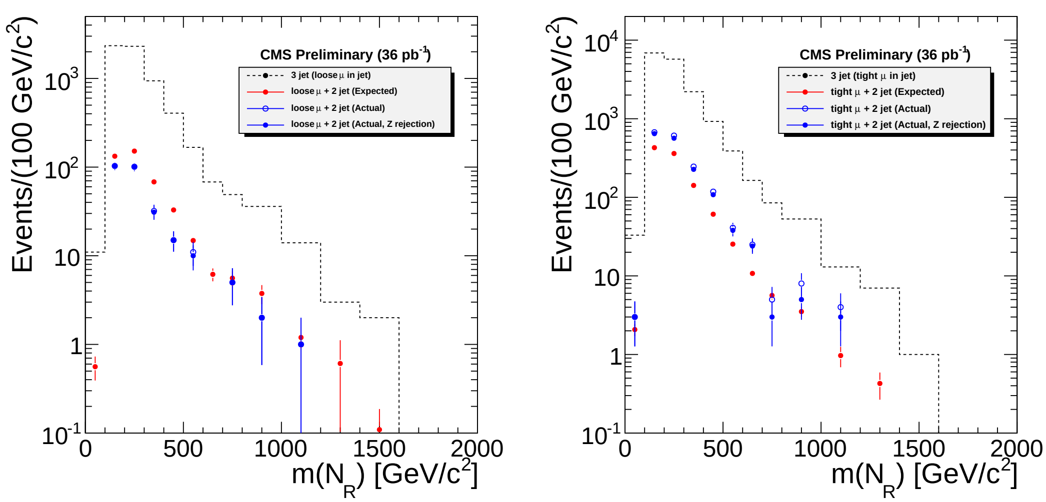

Figure 8.4: Data-based study of three jet and μjj events to determine the QCD uncertainty. The muon survival rate from Figure 7.10 is applied to the muon from the three jet sample (black histogram, where the muon is required to be in one of the jets). The expectations (red points) are compared to a distribution of two jets and an isolated muon, with (solid blue) and without (open blue circles) a Z veto assuming an additional muon is found.

The results of the closure test indicate that 439 (1271) μjj events are predicted to survive with a loose (tight) quality muon using the three jet sample, whereas 316 (1986) μjj events are found with an isolated loose (tight) quality muon. This implies a ratio between actual and expected events of 0.72 for loose quality muons and 1.56 for tight muons. As at least one tight muon in our nominal $\mu\mu jj$ event selection is required, a conservative 100% systematic uncertainty is applied to the muon QCD background estimation.

8.11 Systematics Summary

Table 8.3: Summary of the systematic uncertainties. The magnitudes of each uncertainty are estimated following the procedure described in the text. The total errors for each process (column) in the last row are obtained by summing in quadrature all the uncertainties in that column. The uncertainties on the total number of background events N_{AllBkg} are derived by taking into account the relative contribution of all background events after the full event selection, and the correlation of each systematic effect between all the background processes.

Systematic Uncertainty	Signal eff.	$t\bar{t}$	$Z + jet$	QCD	Other bkgd	All bkgd
Jet Energy Scale	$\pm$ <1-10%	±11%	±4%	–	±11%	±8%
Muon Energy Scale	$\pm$ <1-2%	±5%	±2%	–	±4%	±4%
MC Statistics	±1-6%	±2%	±3%	–	±17%	±2%
Trigger Efficiency	±0.5%	±0.5%	±0.5%	–	±0.5%	±0.5%
Muon Reco/ID/Iso	±2%	±2%	±2%	–	±2%	±2%
MC Normalization	–	±14%	±9%	–	±6%	±8%
ISR/FSR	±3%	±6%	–	–	–	±3%
PDF	±4%	±6%	±9%	–	–	±7%
Fact./Ren. scale	$\pm$ <0.5%	±8%	±15%	–	–	±11%
QCD estimate	–	–	–	±100%	–	±0%
Total	±6-13%	±22%	±21%	±100%	±21%	±18%

Chapter 9

Final Results

> There is something which unites magic and applied science (technology) while separating them from the ”wisdom” of earlier ages. For the wise men of old, the cardinal problem of human life was how to conform the soul to objective reality, and the solution was wisdom, self-discipline, and virtue. For the modern, the cardinal problem is how to conform reality to the wishes of man, and the solution is a technique.
>
> — C.S. Lewis

This chapter describes the final results of the analysis observed from applying the selections and estimation procedures described in the previous three chapters to the data samples described in Chapter 5. Expanded exclusion limits are set, and prospects for further discovery or exclusion in the year 2011 are discussed.

9.1 Observed Events

The number of observed and expected events that survive the various stages of the event selection are presented in Tables 9.1. One event is found in data with $M_{W_R} >$ 520 GeV/c^2 containing opposite-sign muons. This is consistent with a background-only hypothesis (given the large error associated with such low numbers), which predicts a total of 2$\pm$0.3 events that pass all selection criteria. Various additional distributions comparing the observed event spectra to signal and background expectations are presented in Fig. 9.1.

Table 9.1: Statistics after each stage of the event selection. Entries marked with "–" represent less than 0.01 events expected. Values displayed in the "Signal" column assume $M_{W_R} = 1000$ GeV/c^2 and $M_{N_\mu} = 500$ GeV/c^2.

	Data	Signal	Tot.Bg	$t\bar{t}$	Z+jets	QCD	W+jets	VV	tW
M0 (Raw)		10000		1165716	2859343		7189090	6369880	494961
M0		22.4		6036	131165		1131620	2425	381
M1	329	13.8	304±59	27	271	1.10	0.14	3.8	0.68
M2	326	13.7	300±58	26	268	1.06	0.14	3.8	0.67
M3	182	13.7	179±35	14	162	0.32	0.12	2.4	0.41
M4	3	12.1	3.4±0.6	1.96	1.31	0.01	0.022	0.062	0.05
M5	1	12.1	2.0 ± 0.4	1.03	0.85	–	0.022	0.037	0.03
M5 (Raw)	1	5397		198	1230	0	2	137	37

Key:

Designator	Meaning
M0	All available events and statistics
M1	Two muons and two jets with object requirements applied
M2	Vertex Z component of all four objects < 0.03 cm to suppress pileup
M3	One muon with $p_T > 60$ GeV/c
M4	$M_{\mu\mu} > 200$ GeV/c^2
M5	$M_{\mu\mu jj} > 520$ GeV/c^2

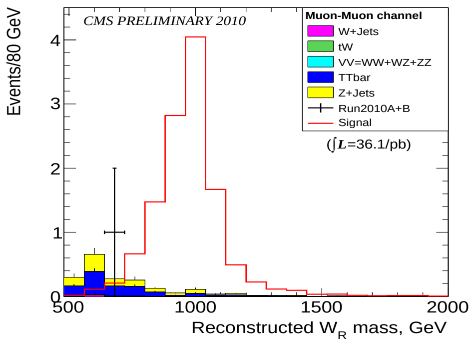

(a) Reconstructed $M_{\mu\mu jj}$ for $\mu\mu jj$ events.

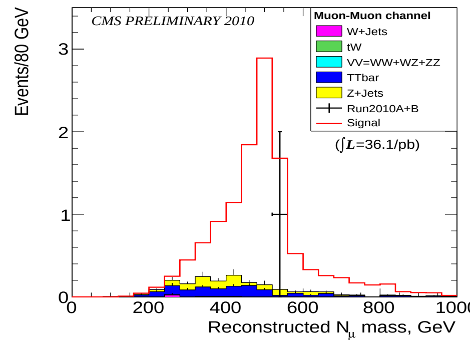

(b) Reconstructed $M_{\mu jj}$ (using the highest p_{T} muon) for $\mu\mu jj$ events.

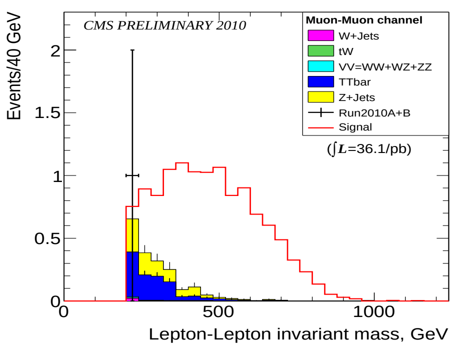

(c) Reconstructed dilepton invariant mass for $\mu\mu jj$ events.

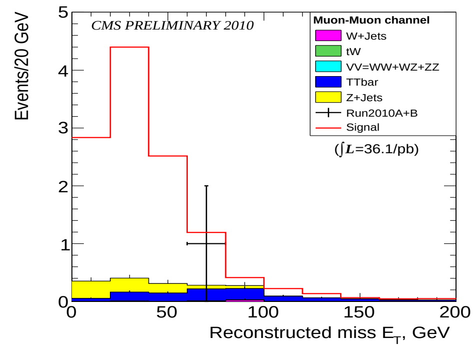

(d) Reconstructed missing transverse energy for $\mu\mu jj$ events.

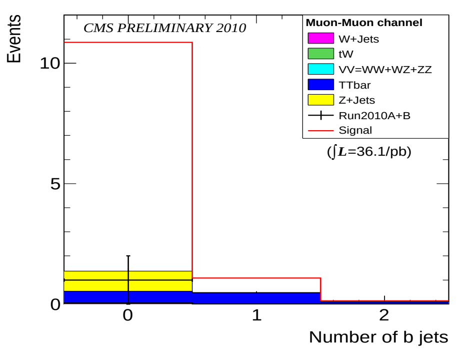

(e) Reconstructed number of b quark jets for $\mu\mu jj$ events.

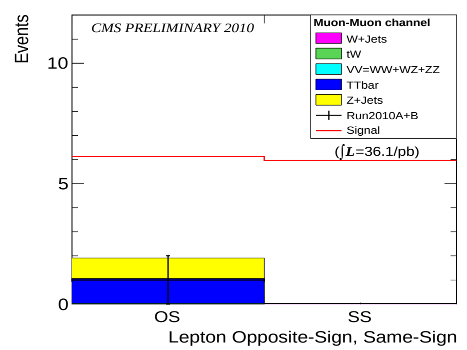

(f) Product of reconstructed lepton charges for $\mu\mu jj$ events.

Figure 9.1: Distributions for events surviving all selections. The signal mass point $M_{W_R} = 1000\ \mathrm{GeV}/c^2$, $M_{N_\mu} = 500\ \mathrm{GeV}/c^2$, is included for comparison.

9.2 Setting Exclusion Limits

The next step in the analysis is to quantify what new information has been learned from all this effort. Typically, for searches of new phenomena, some region of a phase space appropriate to the analysis is carved out and considered excluded according to a commonly accepted level of statistical confidence. This section describes the method used to accomplish this exclusion in some detail.

9.2.1 Testing the signal and background hypotheses

The analysis of these search results has been formulated within the framework of classical statistical hypothesis testing. Within that context, one defines two hypotheses, the null and alternate hypotheses. Ref. [57] succinctly states (p. 82) that

> The null hypothesis is that the signal is absent and the alternate hypothesis is that it exists. An analysis of search results is simply the formal definition of the procedure [that] quantifies the degree to which [these two] hypotheses are favored or excluded by an experimental observation.

Since background is present even after all selection criteria are applied, the two hypotheses are labeled B, for the background-only or null hypothesis, and $S+B$ for signal plus background or alternate hypothesis. Ref. [57] then proceeds to describe the procedure, which has been adopted here, in the form of three steps:

1. **Identify the observables**. In this analysis the final observable has been defined as the number of events passing all selection criteria. The distribution of these events as a function of the "parameter of interest", the four-object mass $M_{\mu\mu jj}$, which would be the mass of the hypothesized W_R boson M_{W_R}, is used in setting final limits.

2. **Define a test statistic** Q that is a function of the defined observables and other parameters of the model. The definition of Q is discussed below. Other parameters of the model, also known as the nuisance parameters, are defined here as the final yields of expected background events from different processes using simulation, their total fractional uncertainties, and the exponential fit slopes from those distributions, as displayed in Figures 7.2 for $t\bar{t}$ and 7.9 for Z+Jets.

3. **Define the rules for exclusion and discovery**, which are the ranges of values of the test statistic for which the signal is considered to be discovered or excluded. To be precise, a *confidence limit* is defined, which is a value of M_{W_R} below which the signal is said to be excluded to a *confidence level* CL of 95%.

Generally the test statistic is designed to increase monotonically, so that small (or large) values signify increasingly signal-like (or background-like) data. This analysis adopts the following sense (although the opposite sense is commonly adopted as well),

$$\begin{array}{ccc} \text{small Q} & & \text{large Q} \\ & \longleftrightarrow & \\ \text{more background-like} & & \text{more signal-like} \end{array}$$

One then speaks of the confidence in a hypothesis $\mathcal{H}$ as being the probability that, given the hypothesis, the test statistic Q is less than or equal to the value observed in the experiment, Q_{obs}, or

$$CL_{\mathcal{H}} = P_{\mathcal{H}}(Q \leq Q_{obs}) = \int_{-\infty}^{Q_{obs}} \frac{dP_{\mathcal{H}}}{dQ} dQ \quad ,$$

where dP_H/dQ is the probability density function, or p.d.f., of the test statistic for hypothesis $\mathcal{H}$. Given the sense of Q that is adopted above, when $\mathcal{H} = S + B$, a high confidence in $\mathcal{H}$ is signified by high values (close to 1) of $CL_{\mathcal{H}} = CL_{s+b}$; but for $\mathcal{H} = B$, high confidence in $\mathcal{H}$ is signified by low values (close to 0) of $CL_{\mathcal{H}} = CL_b$.

The test statistic is formulated in terms of the concept of a likelihood. Likelihoods are closely related to, but also crucially distinct from, probabilities. Within this context, one speaks of the probability P that X number of events would be observed given a certain model M with a set of parameters Θ, notated $P(X|\Theta)$; i.e., the model is predicated, and the amount of data X to be observed, given $M(\Theta)$, is a hypothetical outcome.

However, our interest is exactly the reverse: the data that has been observed is the given, and we are interested in saying something definitive about the theory. That is, we want the *likelihood* that the model $M(\Theta)$ is true for the observed data X, notated $L(\Theta|X)$. $L(\Theta|X)$ is generally proportional to $P(X|\Theta)$, where the constant of proportionality is arbitrary, so that one is actually interested in the ratio of likelihoods where this constant is eliminated. One speaks then of whether one model is more likely than another, given the observed data.

Then, given that the parameter of interest is a function of a continuous variable $M_{\mu\mu jj}$, one replaces the probability P with a p.d.f. that describes the probability to observe X events as a function of the variable. For this analysis there are two p.d.f.'s, $B(M_{WR})$ corresponding to hypothesis $\mathcal{H} = B$, and the signal plus background p.d.f. $SB(M_{WR})$ corresponding to hypothesis $\mathcal{H} = S + B$ (p.d.f.'s B and SB are distinct from p.d.f.'s $P_{\mathcal{H}}$ with $\mathcal{H} = S + B$ or B described previously; the first pair are functions of the observable M_{WR}, whereas the latter pair are functions of the test statistic Q and are derived from the first pair).

Therefore we define the test statistic Q to be the ratio of likelihoods $L(\Theta|X)$, which is equivalent to the ratio of p.d.f.'s:

$$Q = \left(\frac{\prod_i SB(M_i)}{\prod_i B(M_i)} \right) \quad ,$$

where the range of possible masses of the W_R boson has been split into discrete intervals, or "bins" M_i indexed by i, which are then considered to be independent. Finally, one generally takes the natural logarithm of Q to form the "log likelihood ratio", which turns the products into sums while maintaining the sense of Q described above:

$$LLR = \log Q$$

9.2.2 The CL_s Method

Use of CL_{s+b} exclusively has been understood as the classical "frequentist" approach to searches; but the CL_s method modifies this approach by normalizing to the confidence level from the null hypothesis:

$$CL_s = \frac{CL_{s+b}}{CL_b}$$

This normalization is intended to make sense of the results from CL_{s+b} when the amount of observed events even calls the background hypothesis into question. This happens frequently in new physics searches such as this one where the available statistics is small. Although CL_s is not, strictly speaking, a confidence, the signal hypothesis will be considered excluded at the confidence level $CL = 95\%$ when

$$1 - CL_s \leq CL \ ; \quad CL_s \geq 0.05$$

9.2.3 Limit Setting with `RooStats`

The cross section limits for this analysis are set using the `RooStats` [58] package. `RooStats` is a package for sophisticated statistical modeling and hypothesis testing. `RooStats` automates much of the machinery of the CL_s method.

This analysis used `RooStats` statistical modeling algorithms to:

- Instantiate p.d.f.'s of the primary background contributors ($t\bar{t}$ and Z+Jets) as exponential decays using the fit parameters shown in Chap. 7.
- Instantiate a signal p.d.f., one for each (M_{W_R}, M_{N_R}) mass hypothesis, using the shape of the four-object invariant mass distribution $M_{\mu\mu jj}$ that remains after all selection criteria.
- Identify the background yields from Table 9.1 and their uncertainties from Table 8.3 as "nuisance parameters" of the models, to be varied over a number of statistical trials. A log-normal distribution is used for these nuisance parameter uncertainties.
- Invoke a hypothesis test that produces an ensemble of pseudo-experiments based on the $SB(M_{\mu\mu jj})$ and $B(M_{\mu\mu jj})$ distributions. The distribution of LLR values is used to determine the confidence levels for the signal plus background hypothesis (CL_{s+b}) and for the background-only hypothesis (CL_b).
- Calculate CL_s from the hypothesis test results.

For each mass hypothesis, these pseudo-experiments are repeated over a range of scan points; that is, the signal p.d.f. is scaled in steps over a cross section interval that is intended to provide complete coverage over the range of cross sections seen in Fig. 5.2. The scan may be considered a "brute force" computing method to determine the contours of the signal cross section boundary, above which the signal hypothesis can be said to be excludable with a 95% confidence, taking into account all the uncertainties that have been quantified. A number of sample scan points are shown in Fig. 9.2 for one mass hypothesis.

The limits for $CL = 0.95$ are shown in Figures 9.3 and 9.4, and are compared with the expected rate of signal production from the PYTHIA computer simulation model. Where the rate of signal production exceeds the confidence limit derived from the observed data, that range of mass hypotheses is considered to be excluded to 95% confidence or better.

The newly excluded region of mass phase space derived from these observations is shown in Fig. 9.5. This plot is generated by taking the difference of the plot shown in Fig. 5.2 (scaled by the k-factor shown in Table 5.1) minus the same plot of cross sections excluded by the observed data from Figures 9.3 and 9.4, and then generating the contour plot where the difference is equal to zero. The plot shows that, given the 36.1 pb^{-1} of collision data that was collected in 2010, the model is excluded for $M(W_R)$ mass points up to 1200 GeV/c^2 with a wide range of possible $M(N_R)$ mass points, and up to approximately $M(W_R) = 1350\ \mathrm{GeV}/c^2$ for an increasingly narrow range of $M(N_R)$ mass points.

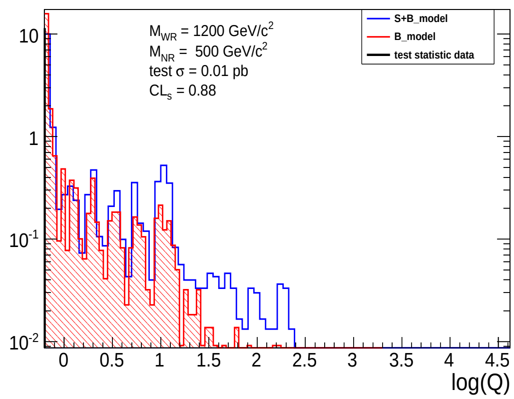

(a) test $\sigma = 0.01$ pb, SB and B are indistinguishable

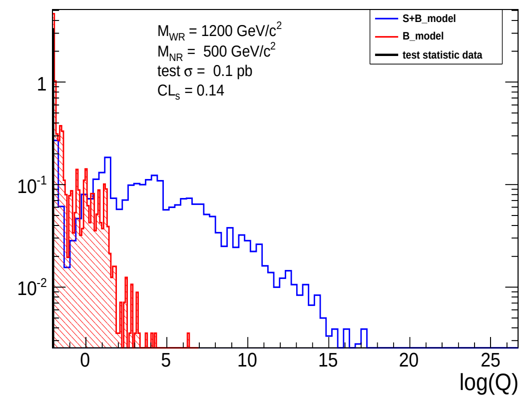

(b) test $\sigma = 0.1$ pb, results would be inconclusive

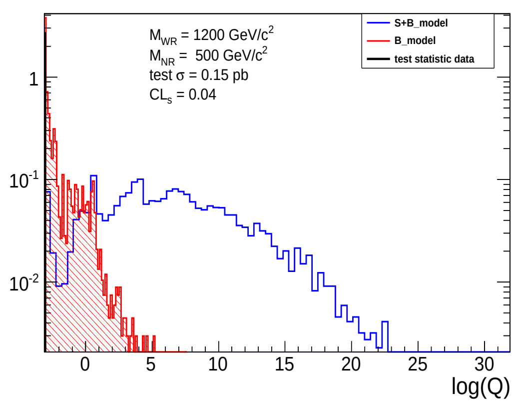

(c) test $\sigma = 0.15$ pb, near the 95% limit boundary

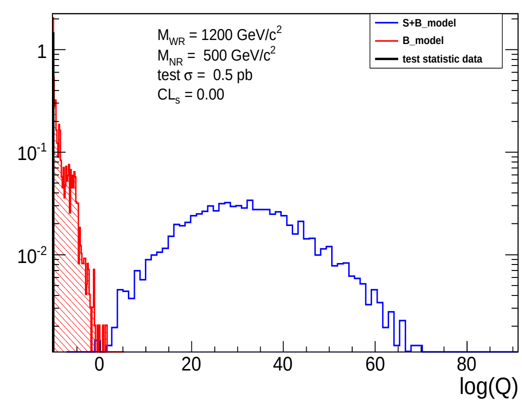

(d) test $\sigma = 0.5$ pb, signal is excluded

Figure 9.2: Signal and background distribution snapshots from a limit scan for mass point (M_{W_R}, M_{N_R})=(1200,500)(GeV/c^2)

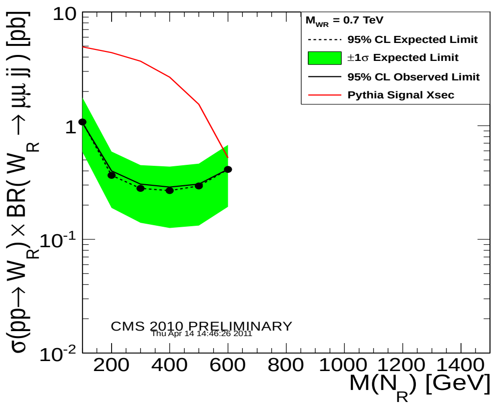

(a) Exclusion as a function of M_{Nu} for $M_{WR} = 0.7\,\mathrm{TeV}/c^2$

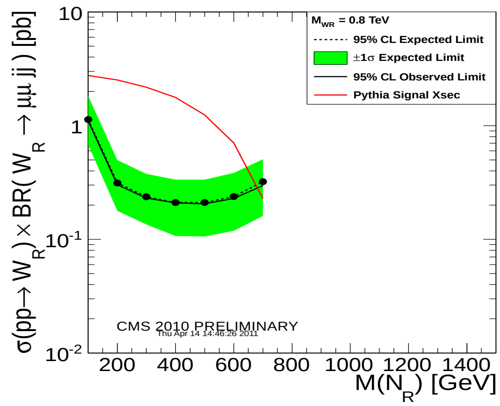

(b) Exclusion as a function of M_{Nu} for $M_{WR} = 0.8\,\mathrm{TeV}/c^2$

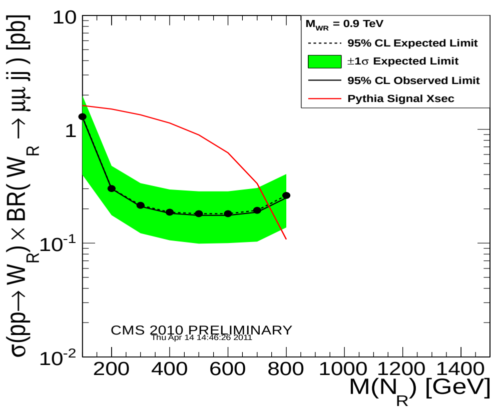

(c) Exclusion as a function of M_{Nu} for $M_{WR} = 0.9\,\mathrm{TeV}/c^2$

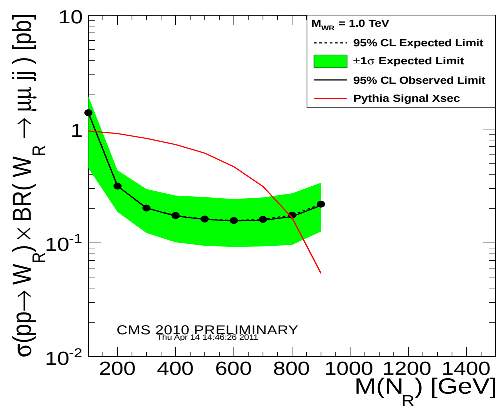

(d) Exclusion as a function of M_{Nu} for $M_{WR} = 1.0\,\mathrm{TeV}/c^2$

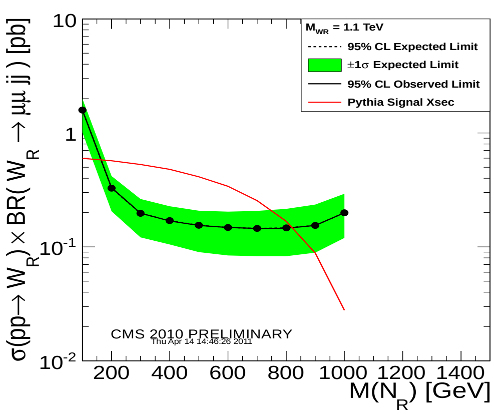

(e) Exclusion as a function of M_{Nu} for $M_{WR} = 1.1\,\mathrm{TeV}/c^2$

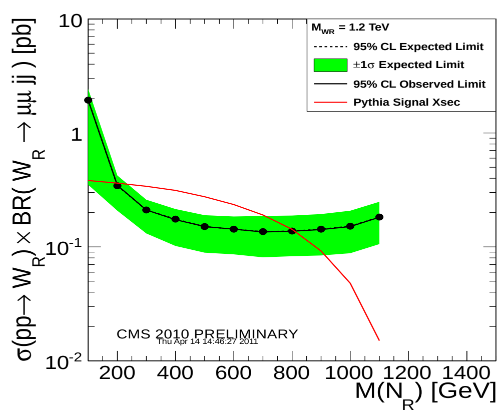

(f) Exclusion as a function of M_{Nu} for $M_{WR} = 1.2\,\mathrm{TeV}/c^2$

Figure 9.3: Exclusion plots for a range of M_{Nu} and M_{WR} hypotheses.

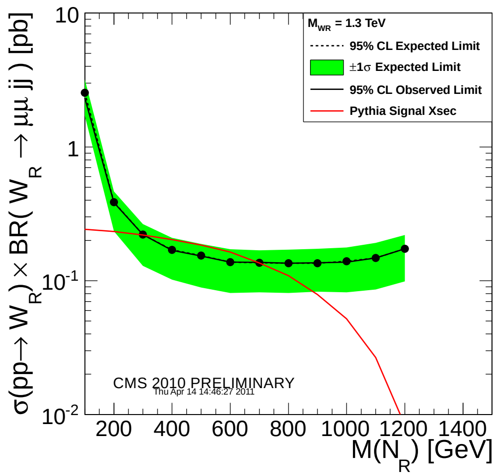

(a) Exclusion as a function of M_{Nu} for $M_{WR} = 1.3\,\mathrm{TeV}/c^2$

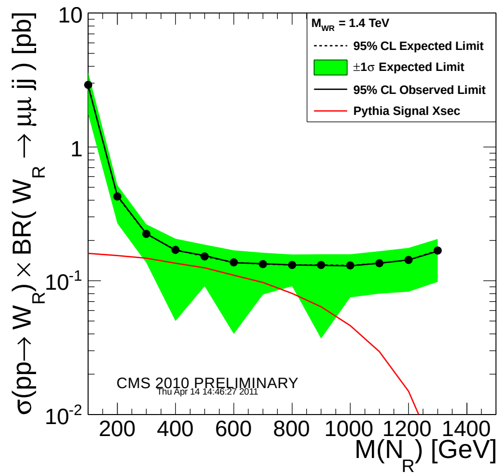

(b) Exclusion as a function of M_{Nu} for $M_{WR} = 1.4\,\mathrm{TeV}/c^2$

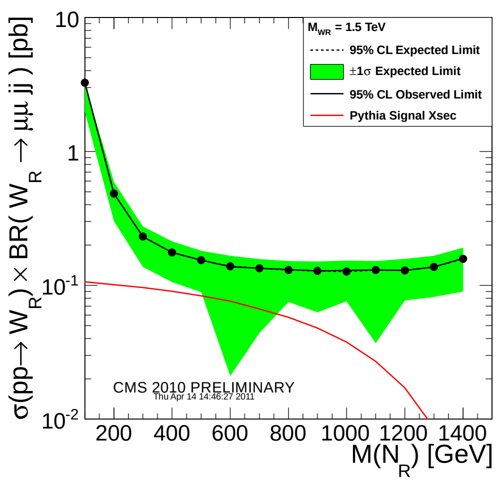

(c) Exclusion as a function of M_{Nu} for $M_{WR} = 1.5\,\mathrm{TeV}/c^2$

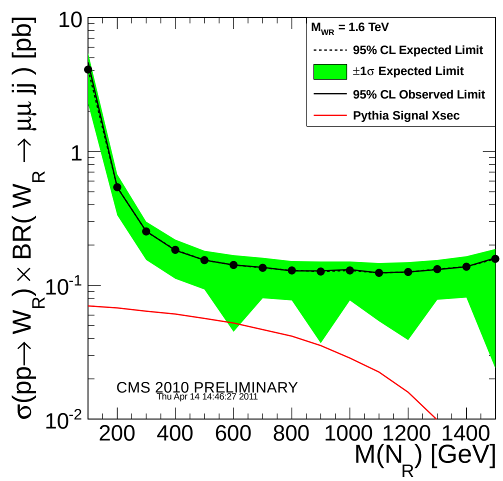

(d) Exclusion as a function of M_{Nu} for $M_{WR} = 1.6\,\mathrm{TeV}$

Figure 9.4: Exclusion plots for a range of M_{Nu} and M_{WR} hypotheses. The highest three mass points exhibit numerical issues with the estimation of the -1σ band; however, this does not affect the interpretation of the results, since the observed and expected limits are very close together.

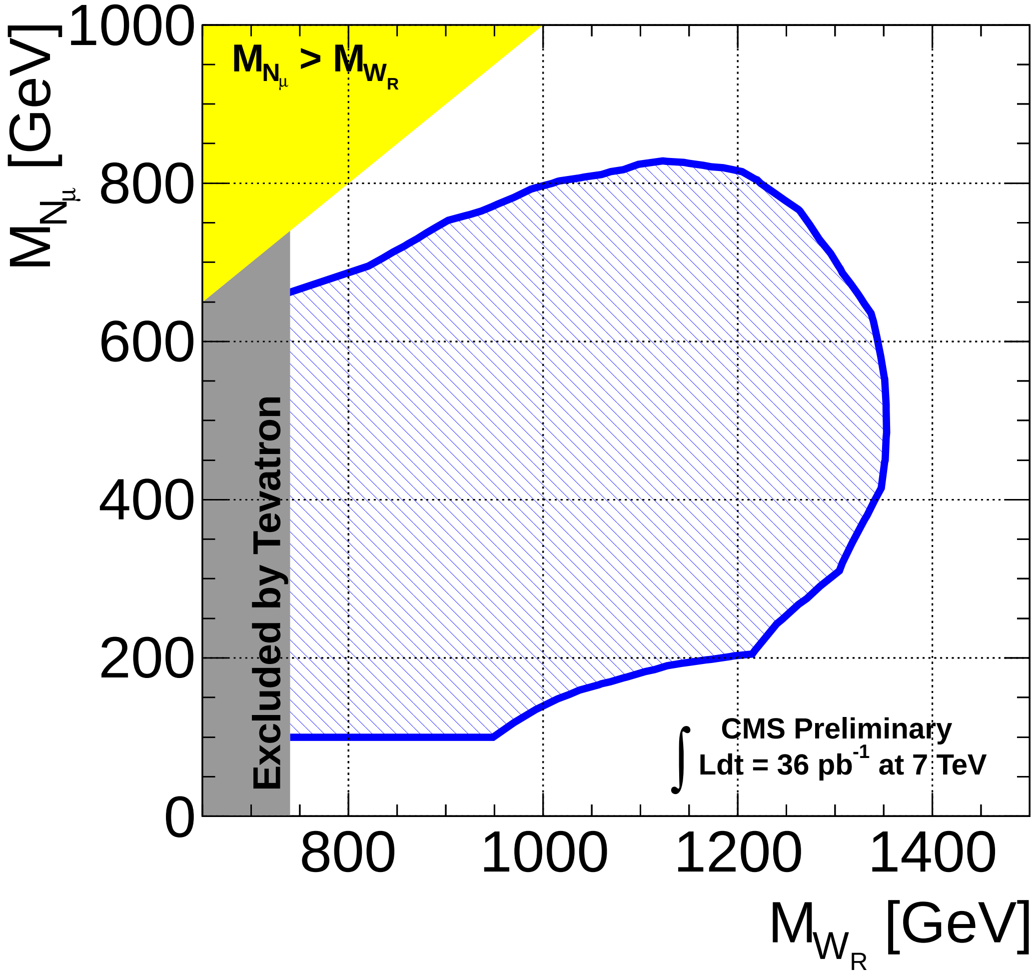

Figure 9.5: 2-D Exclusion plot in the M_{Nu} / M_{WR} plane. The region in dark gray (left) represents the exclusion limit from the Tevatron experiments.

9.3 Prospects for 2011

To study the prospects for expansion of the sensitivity envelope of this analysis in the year 2011, the signal and background Monte Carlo samples that survived all selection criteria were scaled to a total integrated luminosity of 1 fb^{-1}. This amount of data is a stated minimum goal of the LHC operators and experiments for the year 2011 [59], with a view to doubling or trebling it.

Supplemental Monte Carlo samples were also generated to provide additional coverage for the study, as shown in Table 9.2.

M(W_R) (GeV/c^2)	M(N_R) (GeV/c^2)
1800	100 400 700 1000 1300 1600
2000	100 400 700 1000 1300 1600 1900
2200	100 400 700 1000 1300 1600 1900
2400	100 400 700 1000 1300 1600 1900 2200

Table 9.2: New mass points generated for exploration of 1 fb^{-1} expected limits.

With this expanded simulation set, the same limit-setting scan described in the previous section was performed, this time plotting the expected limit (rather than the observed limit). The results are shown in Fig. 9.6, indicating that the sensitivity of this analysis can be extended to over M(W_R)=2 TeV/c^2.

This is a first order estimate, since no adjustment has been made for systematics induced by the increased luminosity, such as “pileup”, which is the effect that uncorrelated interactions within the same bunch crossing have on the interaction of interest. However, it is anticipated that the main impact of pileup on this analysis will come in the systematic change to jet energies from the calorimeters; the muon tracker isolation and vertex requirements will be generally immune to effects of pileup.

In addition, with the increase in statistics, new techniques for separating signal and background signatures, such as the use of a neural net, can be brought to bear, enhancing the sensitivity of this analysis even further.

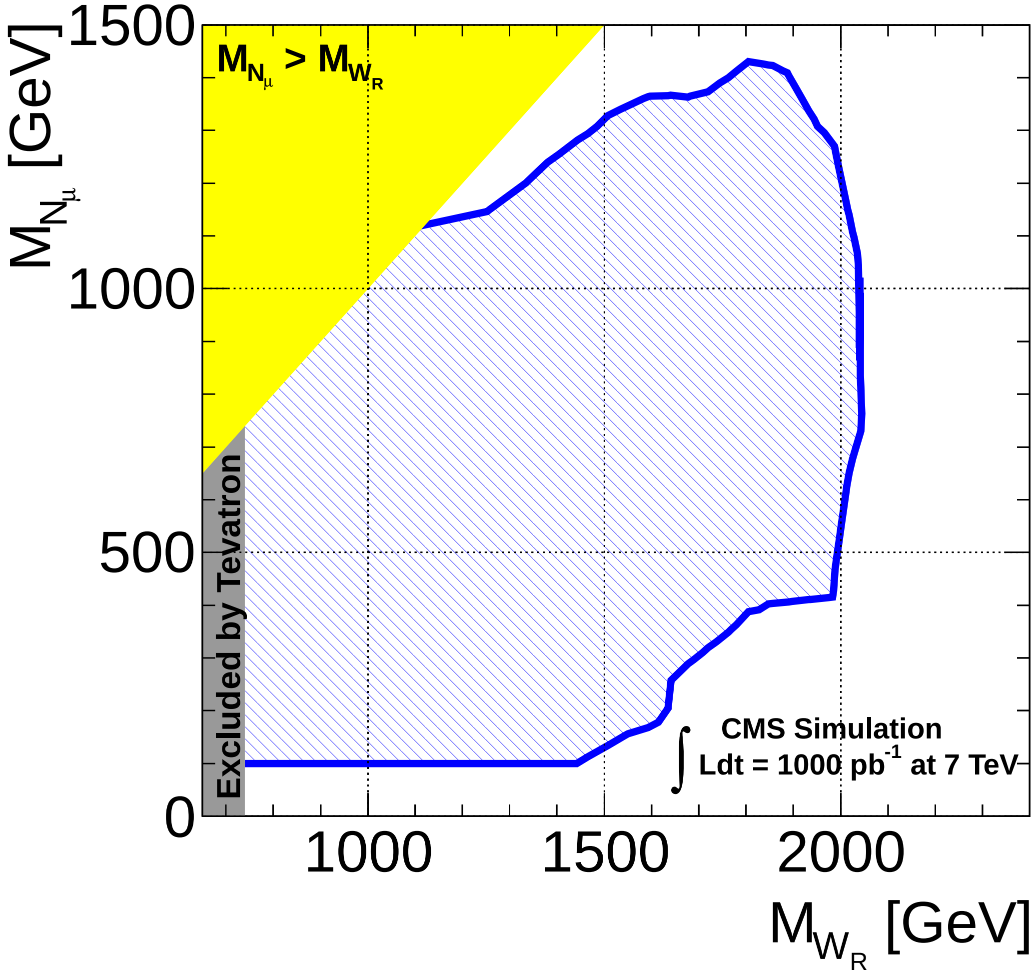

Figure 9.6: Projected 2-D Discovery/Exclusion plot in the M_{Nu} / M_{WR} plane for 1 fb^{-1} total integrated luminosity.

Chapter 10

Conclusion

> The words of the wise are like goads, their collected sayings like firmly embedded nails–given by one Shepherd. Be warned, my son, of anything in addition to them. Of making many books there is no end, and much study wearies the body. Now all has been heard; here is the conclusion of the matter: Fear God and keep his commandments, for this is the whole duty of man. For God will bring every deed into judgment, including every hidden thing, whether it is good or evil.
>
> — Ecclesiastes

In this thesis has been presented a search for right-handed bosons W_R and heavy neutrinos N_ℓ , $\ell = \mu$ of the Left-Right symmetric model. It was found that the collision data sample is in good agreement with the expectations from SM processes. The contribution of the main backgrounds was determined using computer generated Monte Carlo simulations and renormalized to data where possible. The background from QCD multi-jet events, which is most difficult to calculate by Monte Carlo, was estimated from data. The uncertainty for the backgrounds was estimated with the aid of data-driven methods. The main systematic uncertainties have been estimated. The number of observed events, passing a selection optimized for the best sensitivity to W_R and heavy neutrinos N_μ, is in good agreement with the predictions for standard model background processes. We have used a modified frequentist approach called CL_S to set a limit on the masses of W_R and N_μ that includes treatment of the systematic uncertainties as nuisance parameters. These limits exceed prior limits set by the Tevatron proton-antiproton collider.

Prospects for extending the exclusion/discovery boundaries in the year 2011, based on an assumed total accumulated luminosity of 1 fb^{-1} at the same beam energy, were also presented.

References

[1] CMS Collaboration. Search for a heavy neutrino and right-handed W of the left-right symmetric model in pp collisions at sqrt(s) =7 TeV. *CMS PAS*, EXO-11-002, To be published.

[2] A. Lesov. The Weak Force: From Fermi to Feynman. 2009, `physics.hist-ph/0911.0058v1`.

[3] Raymond Davis, Don S. Harmer, and Kenneth C. Hoffman. Search for neutrinos from the sun. *Phys. Rev. Lett.*, 20(21):1205–1209, May 1968.

[4] Q. R. Ahmad et al.. Direct Evidence for Neutrino Flavor Transformation from Neutral-Current Interactions in the Sudbury Neutrino Observatory. *Phys. Rev. Lett.*, 89(1):011301, Jun 2002.

[5] V. Gribov and B. Pontecorvo. Neutrino astronomy and lepton charge. *Physics Letters B*, 28(7):493 – 496, 1969.

[6] J W F Valle. Neutrino physics overview. *Journal of Physics: Conference Series*, 53(1):473, 2006.

[7] M. Guidry. *Gauge Field Theories, An Introduction With Applications.* Wiley-Interscience, 1980, 1999.

[8] S. Glashow. Towards a unified theory - threads in a tapestry. In Stig Lundqvist, editor, *Nobel Lectures, Physics 1971-1980*, Singapore, 1992. World Scientific Publishing Co., `http://nobelprize.org/nobel_prizes/physics/laureates/1979/glashow-lecture.pdf`.

[9] C. Quigg. The electroweak theory. *TASI 2000 Lectures on Electroweak Theory: FERMILAB-CONF-01/001-T.*, 2002, `hep-ph/0204104v1`.

[10] Amsler, C. et al. (Particle Data Group). Review of particle physics. *Phys. Lett. B*, 667, 2008.

[11] J.C.A. Wevers. Physics Formulary, 1995,2009.

[12] Jogesh C. Pati and Abdus Salam. Lepton number as the fourth "color". *Phys. Rev. D*, 10(1):275–289, Jul 1974. The model presented herein has been frequently referred to as a "partial unification theory", which one may perhaps puckishly abbrieviate as "a PUT".

[13] R. N. Mohapatra and J. C. Pati. "Natural" left-right symmetry. *Phys. Rev. D*, 11(9):2558–2561, May 1975.

[14] G. Senjanovic and R. N. Mohapatra. Exact left-right symmetry and spontaneous violation of parity. *Phys. Rev. D*, 12(5):1502–1505, Sep 1975.

[15] Goran Senjanovic. Spontaneous breakdown of parity in a class of gauge theories. *Nuclear Physics B*, 153:334 – 364, 1979.

[16] Rabindra N. Mohapatra and Goran Senjanović. Neutrino mass and spontaneous parity nonconservation. *Phys. Rev. Lett.*, 44(14):912–915, Apr 1980.

[17] R.D. Peccei. Neutrino physics. *AIP Conf.Proc.*, 490:80–124, 1999, `hep-ph/9906509v1`.

[18] E.Kh. Akhmedov. Neutrino physics. *FISIST/1-200/CFIF*, 2000, `hep-ph/0001264v2`.

[19] R. N. Mohapatra and R. E. Marshak. Local $B-L$ Symmetry of Electroweak Interactions, Majorana Neutrinos, and Neutron Oscillations. *Phys. Rev. Lett.*, 44(20):1316–1319, May 1980.

[20] Robert E. Marshak. Yukawa Meson, Sakata Model and Baryon-Lepton Symmetry Revisited. *Progress of Theoretical Physics Supplement*, 85:61–74, 1985.

[21] Ho Tso-hsiu, Ching Cheng-rui, and Tao Zhi-jian. Production of right-handed gauge bosons and heavy majorana neutrinos at the superconducting super collider. *Phys. Rev. D*, 42(7):2265–2273, Oct 1990.

[22] Amitava Datta, Manoranjan Guchait, and D. P. Roy. Prospect of heavy right-handed neutrino search at energies reached at the superconducting super collider and cern large hadron collider. *Phys. Rev. D*, 47(3):961–966, Feb 1993.

[23] Wai-Yee Keung and Goran Senjanović. Majorana neutrinos and the production of the right-handed charged gauge boson. *Phys. Rev. Lett.*, 50(19):1427–1430, May 1983.

[24] Torbjorn Sjostrand, Stephen Mrenna, and Peter Skands. PYTHIA 6.4 Physics and Manual. *JHEP*, 05:026, 2006.

[25] James Botts, Jorge G. Morfin, Joseph F. Owens, Jianwei Qiu, Wu-Ki Tung, and Harry Weerts. CTEQ parton distributions and flavor dependence of sea quarks. *Physics Letters B*, 304(1-2):159 – 166, 1993.

[26] Ryan Gavin, Ye Li, Frank Petriello, and Seth Quackenbush. Fewz 2.0: A code for hadronic z production at next-to-next-to-leading order. 1011.3540.

[27] V. M. et al. Abazov. Search for $w^{'}$ boson resonances decaying to a top quark and a bottom quark. *Phys. Rev. Lett.*, 100(21):211803, May 2008.

[28] G. Beall, Myron Bander, and A. Soni. Constraint on the mass scale of a left-right-symmetric electroweak theory from the $k_L - k_S$ mass difference. *Phys. Rev. Lett.*, 48(13):848–851, Mar 1982.

[29] Paul Langacker and S. Uma Sankar. Bounds on the mass of w_R and the $w_L - w_R$ mixing angle ζ in general $su(2)_L \times su(2)_R \times u(1)$ models. *Phys. Rev. D*, 40(5):1569–1585, Sep 1989.

[30] J. Polak and M. Zralek. Updated constraints on the neutral-current parameters in left-right symmetric model. *Nuclear Physics B*, 363(2-3):385 – 400, 1991.

[31] Thomas G. Rizzo. Model dependence of w_R searches at the fermilab tevatron. *Phys. Rev. D*, 50(1):325–330, Jul 1994.

[32] C.A. Heusch. *Nucl. Phys. B*, 416, 1994.

[33] S.N.Gninenko, M.M.Kirsanov, N.V.Krasnikov, and V.A.Matveev. *Mod. Phys. Lett.*, 17:1407, 2002.

[34] CMS Collaboration. The CMS Experiment at the CERN LHC. *J. Inst.*, 3 S08004, 2008.

[35] L. Evans and P. Bryant (eds.). LHC machine. *J. Inst.*, 3 S08001, 2008.

[36] Baden, A.R. Jets and Kinematics in Hadronic Collisions. *International Journal of Modern Physics A*, 13(11):1817–1845, 1998.

[37] Serguei Chatrchyan et al. Alignment of the CMS Silicon Tracker during Commissioning with Cosmic Rays. *JINST*, 5:T03009, 2010, `physics.ins-det/0910.2505`.

[38] Serguei Chatrchyan et al. Commissioning and Performance of the CMS Silicon Strip Tracker with Cosmic Ray Muons. *JINST*, 5:T03008, 2010, `physics.ins-det/0911.4996`.

[39] CMS Collaboration. Performance and operation of the CMS electromagnetic calorimeter. *Journal of Instrumentation*, 5(03):T03010, 2010.

[40] CMS-HCAL Collaboration. Design, performance, and calibration of CMS hadron-barrel calorimeter wedges. *Eur. Phys. J. C*, 55:159–171, 2008.

[41] CMS-HCAL Collaboration. Design, performance, and calibration of the CMS hadron-outer calorimeter. *Eur. Phys. J. C*, 57:653–663, 2008.

[42] T. Zimmerman and J. Hoff. The design of a charge integrating, modified floating point ADC chip. *IEEE J. Solid State Circuits*, 39:895–905, 2004.

[43] CMS-HCAL Collaboration. The CMS barrel calorimeter response to particle beam from 2 to 350 gev/c. *Eur. Phys. J. C*, 60:359–373, 2009.

[44] M.L.Mangano, M.Moretti, F.Piccinini, R.Pittau, and A. Polosa. Alpgen, a generator for hard multiparton processes in hadronic collisions. *JHEP*, 0307:001, 2003.

[45] S. Jadach, Z. Was, R. Decker, and J. Kuhn. TAUOLA the library for tau lepton decay, and KKMC/KORALB/KORALZ... status report. *Nucl.Phys.Proc.Suppl.*, 98:96–102, 2001.

[46] Standard Model Cross Sections for CMS at 7 TeV. twiki:StandardModelCrossSections, 2010.

[47] J.Alwall et al. Madgraph/madevent v4: The new web generation. *JHEP*, 09:028, 2007.

[48] CMS Collaboration. Measurement of the top-quark pair-production cross section in the dilepton channel at $\sqrt{s} = 7$ TeV. *CMS PAS*, TOP-10-005, 2010.

[49] Cacciari, M., Salam, G., and Soyez, G. The anti k_{T} clustering algorithm. *JHEP*, 04, 2008.

[50] CMS Collaboration. Jet Energy Corrections Determination at 7 TeV. *CMS PAS*, JME-10-010, 2010.

[51] CMS Collaboration. Performance of CMS muon identification in pp collisions at $\sqrt{s} = 7$ TeV. *CMS PAS*, MUO-2010-002, 2010.

[52] CMS Collaboration. Electron reconstruction and identification at $\sqrt{s} = 7$ TeV. *CMS PAS*, EGM-10-004, 2010.

[53] Baffioni, S., et al.. Electron reconstruction in CMS. *The European Physical Journal C - Particles and Fields*, 49:1099–1116, 2007. 10.1140/epjc/s10052-006-0175-5.

[54] CMS Collaboration. Electromagnetic calorimeter commissioning and performance with 7 TeV data. *CMS PAS*, EGM-10-002, 2010.

[55] CMS Collaboration. Measurement of CMS Luminosity. *CMS PAS*, EWK-10-004, 2010.

[56] G. Altarelli, et al.. The Les Houches Accord PDFs (LHAPDF) and LHAGLUE 575, 2005.

[57] A. L. Read. Presentation of search results: the CLs technique. *Journal of Physics G: Nuclear and Particle Physics*, 28, 2002.

[58] Lorenzo Moneta, Kevin Belasco, Kyle Cranmer, Alfio Lazzaro, Danilo Piparo, et al. The RooStats Project. *Proceedings of Science*, PoS(ACAT2010)057, 2010, `physics.data-an/1009.1003`.

[59] C Carli. Proceedings of the Chamonix 2011 workshop on LHC performance. oai:cds.cern.ch:1341525. Technical Report CERN-ATS-2011-005, CERN, Geneva, Mar 2011.

Appendix A

Glossary and Acronyms

Care has been taken in this thesis to minimize the use of jargon and acronyms, but this cannot always be achieved. This appendix defines jargon terms in a glossary, and contains a table of acronyms and their meaning.

A.1 Glossary

- **Abelian/non-Abelian** – A property of groups in group theory whereby the application of the group operation on the elements in the group does (non-Abelian) or does not (Abelian) depend on the order of the elements; also known as the commutative/non-commutative property.

- **baryon** – A particle consisting of three valence quarks plus gluons; the proton is a baryon consisting of two "up" quarks and a "down" quark.

- **coupling constant** – Within particle field theory, the strength of the interaction (or "coupling") between two particle fields is described by a number, generally less than or equal to unity. Each of the fundamental interactions has a characteristic coupling constant.

- **cross section** – A particle physicist's unit of measure of the probability of occurrence of a given subatomic process. It has units of area. In this paper the most commonly used unit is the picobarn: 1 pb = 10^{-36}cm^2.

- **hadron** – A particle consisting of quarks and gluons.
- **hadronization** – The process whereby a "parton" (gluon or quark constituent of a proton) attempting to escape the "color field" associated with the strong interaction, causes the energy associated with the separation to be converted into additional quarks and gluons spontaneously created from the vacuum. The quarks and gluons combine to form new hadrons, since the theory of Quantum Chromodynamics (QCD) stipulates that such quarks or gluons cannot exist in isolation.
- **hit** – A term used to describe the registration in a single detector cell (silicon strip, or pixel, or calorimeter cell) of the passage of a particle or particle shower.
- **jet** – A collimated stream of hadronic and electromagnetic particles arising from the hadronization of a high p_{T} gluon or quark.
- **lepton** – A fundamental particle that does not carry a color charge in the manner of quarks and gluons, and therefore does not participate in the strong interaction.
- **Monte Carlo** – Generally refers to a computer simulation technique that involves the generation of random trials. In the context of particle physics, this term can refer either to computer programs that simulate the production, propagation through the detector, and decay of particles, or to the data samples generated by such programs.
- **parton** – General term for a gluon or quark constituent of a proton.
- **parton distribution function** – A function describing the fraction of a proton's momentum that is carried by the component partons.
- **QCD** – While QCD formally stands for Quantum Chromo-Dynamics, the quantum field theory of color-charged particles, QCD is also often used to refer to the process of the generation of hadronic multijets in hadron collisions, a ubiquitous background at the LHC.
- **tag-and-probe** – An analysis technique used to assess the efficiency of various detector and analysis selection effects.

- **tower** – In the context of CMS, a tower refers to a combination of calorimetric (ECAL+HCAL) cells that are located at the same general (η,ϕ) angular coordinates with respect to the interaction point. The tower therefore measures the total calorimetric response of CMS in that sector of η-ϕ space for a given collision event.

- **transverse** – In the context of detectors like CMS, the term transverse in relation to quantities like energy and momentum refer to that component of the quantity that is directed perpendicular to the beamline. This is true even of normally scalar quantities like energy; the "transverse energy" is found by multiplying $\sin\theta$ times the total energy, where θ is the polar angle of the particle trajectory (or IP-to-calorimeter cell axis) with respect to the beamline.

- **V-A Theory** – The theory developed by Gellman, Feynman, Sudarshan and Marshak in the 1950s that expresses the mathematical form of the Lagrangian term governing weak interactions in terms of the difference between two bilinear covariant forms, vector (V) minus axial (A).

A.2 Acronyms

Table A.1: Acronyms

Acronym	Meaning
ADC	Analog-to-Digital Converter
ASIC	Application-Specific Integrated Circuit
B-L	Baryon number minus Lepton number
CCA	Channel Control ASIC
CL	Confidence Level
COTS	Commercial Off-The-Shelf
CMS	Compact Muon Solenoid
CSC	Cathode Strip Chamber
CSCTF	Cathode Strip Chamber Track Finder
DAQ	Data AcQuisition

Table A.1 – continued from previous page

Acronym	Meaning
DT	Drift Tube
DTTF	Drift Tube Track Finder
ECAL	Electromagnetic CALorimeter
FEE	Front End Electronics
GMT	Global Muon Trigger
GT	Global Trigger
GUT	Grand Unification (or Unified) Theory
h.c.	hermitian conjugate
HB	HCAL Barrel
HCAL	Hadron CALorimeter
HE	HCAL Endcap
HEEP	High-Energy Electron/Photon
HF	HCAL Forward
HLT	High-Level Trigger
HO	HCAL Outer
HPD	Hybrid Photo-Diode
IP	Interaction Point
L1	Level-1
L1A	Level-1 Accept
LHC	Large Hadron Collider
LLR	Log Likelihood Ratio
LO	Leading Order
LRSM	Left-Right Symmetric Model
LUT	Look-Up Table
MET	Missing transverse energy ($\not\!\!E_{\mathrm{T}}$)
MC	Monte Carlo
NLO	Next-to Leading Order
NNLO	Next-to-Next-to Leading Order
PDF	Parton Distribution Function
p.d.f.	probability density function

Table A.1 – continued from previous page

Acronym	Meaning
PMT	Photo-multiplier Tube
QCD	Quantum Chromo-Dynamics
QED	Quantum Electro-Dynamics
QIE	Charge (Q)-Integrating Electronics
RBX	Readout BoX
SC	SuperCluster
SM	Standard Model
TDC	Time-to-Digital Converter
TEC	Tracker EndCap
TIB	Tracker Inner Barrel
TID	Tracker Inner Disk
TOB	Tracker Outer Barrel
V-A	Vector minus Axial

A.3 Analysis variables

Table A.2: Analysis variables and units

Variable	Definition
p_{T}	Transverse Momentum
E_{T}	Transverse Energy
η	the pseudo-rapidity angular coordinate (cf. Sec 3.3)
ϕ	the azimuthal angular coordinate (cf. Sec 3.3)
x, y, z	the first, second and third Cartesian coordinates (cf. Sec 3.3)
M_{W_R}	Mass of the hypothetical right-handed W boson
M_{N_R}	Mass of the hypothetical right-handed heavy neutrino
$M_{\mu\mu}$	Dimuon invariant mass
$M_{\mu\mu jj}$	The measured four-object (two muons and two jets) invariant mass, equivalates to M_{W_R}
GeV	Giga- (10^9) electron volt
MeV	Mega- (10^6) electron volt
TeV	Tera- (10^{12}) electron volt